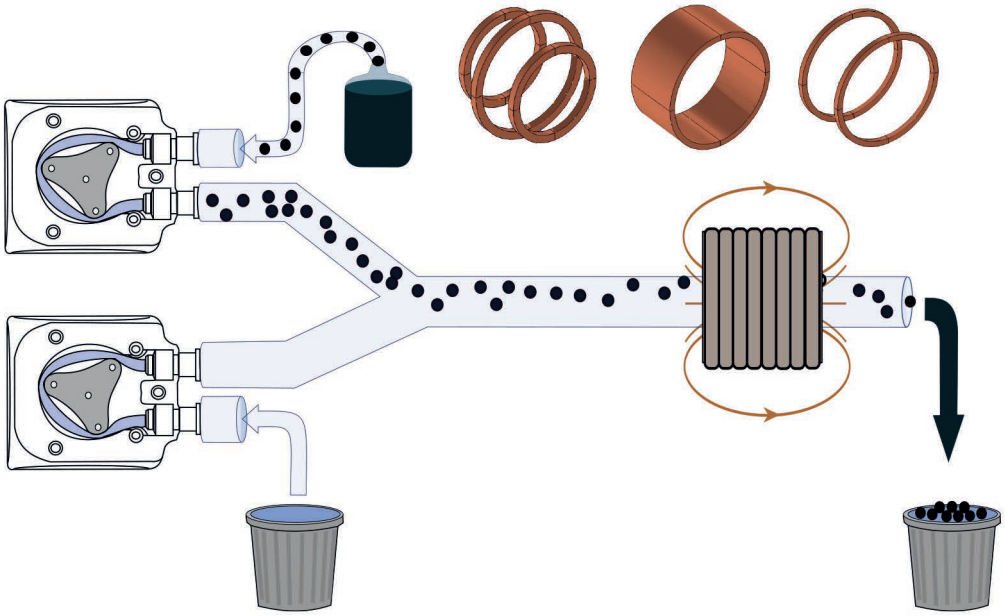

FAU Forschungen, Reihe B, Medizin, Naturwissenschaft, Technik 39

Doaa Ahmed

Detection of Superparamagnetic Iron Oxide Nanoparticles in Fluid Flow for Molecular Communication Applications: Analysis, Simulation, Experimentation and Design Guidelines

FAU University Press

Doaa Ahmed

Detection of Superparamagnetic Iron Oxide Nanoparticles in Fluid Flow for Molecular Communication Applications: Analysis, Simulation, Experimentation and Design Guidelines

FAU Forschungen, Reihe B
Medizin, Naturwissenschaft, Technik
Band 39

Herausgeber der Reihe:
Wissenschaftlicher Beirat der FAU University Press

Doaa Ahmed

Detection of Superparamagnetic Iron Oxide Nanoparticles in Fluid Flow for Molecular Communication Applications: Analysis, Simulation, Experimentation and Design Guidelines

Erlangen
FAU University Press
2022

Bibliografische Information der Deutschen Nationalbibliothek:
Die Deutsche Nationalbibliothek verzeichnet diese Publikation in der Deutschen Nationalbibliografie; detaillierte bibliografische Daten sind im Internet über http://dnb.d-nb.de abrufbar.

Bitte zitieren als
Ahmed, Doaa. 2022. *Detection of Superparamagnetic Iron Oxide Nanoparticles in Fluid Flow for Molecular Communication Applications: Analysis, Simulation, Experimentation and Design Guidelines*. FAU Forschungen, Reihe B, Medizin, Naturwissenschaft, Technik Band 39. Erlangen: FAU University Press. DOI: 10.25593/978-3-96147-518-6.

Der vollständige Inhalt des Buchs ist als PDF über den OPUS-Server der Friedrich-Alexander-Universität Erlangen-Nürnberg abrufbar:
https://opus4.kobv.de/opus4-fau/home

Verlag und Auslieferung:
FAU University Press, Universitätsstraße 4, 91054 Erlangen

Druck: docupoint GmbH

ISBN: 978-3-96147-517-9 (Druckausgabe)
eISBN: 978-3-96147-518-6 (Online-Ausgabe)
ISSN: 2198-8102
DOI: 10.25593/978-3-96147-518-6

Detection of Superparamagnetic Iron Oxide Nanoparticles in Fluid Flow for Molecular Communication Applications: Analysis, Simulation, Experimentation and Design Guidelines

Detektion von superparamagnetischen Eisenoxid-Nanopartikeln im Flüssigkeitsfluss für Anwendungen in der molekularen Kommunikation: Analyse, Simulation, Experimente und Designrichtlinien

Der Technischen Fakultät
der Friedrich-Alexander-Universität
Erlangen-Nürnberg

zur
Erlangung des Doktorgrades Dr.-Ing.

vorgelegt von

Doaa Ahmed, M.Sc.

aus Ismailia, Ägypten

Als Dissertation genehmigt
von der Technischen Fakultät
der Friedrich-Alexander-Universität Erlangen-Nürnberg

Tag der mündlichen Prüfung:	03.02.2022
Gutachter:	Prof. Dr.-Ing. Georg Fischer
	Assoz. Univ.-Prof. DI. Dr. Werner Haselmayr

Preface

This dissertation is based on scientific work accomplished under the supervision of Prof. Dr.-Ing. Georg Fischer at the Institute for Electronics Engineering at the Friedrich-Alexander-University Erlangen-Nuremberg. The significant parts of this thesis are written in sole monographic style. However, a portion of this dissertation is already published in existing publications, as stated below.

- Section 5.1.3 has some parts from [4], which is joint work with our colleagues from the Chair for Digital Transmission and Section for Experimental Oncology and Nanomedicine. The author of this thesis has mainly written the manuscript.
- Section 1.3 states some information from [3, 5], which have been mainly written by the author of this thesis as a proof of concept to the idea given in section 1.2.
- The testbed used in this dissertation was first introduced in [138].
- Also, the author has participated in other publications [20, 125, 136], which belong to the same topic of the dissertation. However, none of their results have been included in this manuscript.
- All other parts of the thesis are so far unpublished work.

Acknowledgment

First and foremost, I praise and thank Allah, the Almighty God, for his showers of blessings throughout my research work to complete this work successfully.

Also, I would like to express my sincere appreciation and gratitude to Prof. Dr.-Ing. Georg Fischer, the academic supervisor of this work, for his continuous help, support, guidance, motivation, enthusiasm, and immense knowledge. It has been an honor to work with him. Throughout this dissertation and master thesis, he has supported me with his patience and expertise and provided me a working place to work in an adequate environment.

My deep and sincere thanks also go to my group leader Dr. rer. nat. Dr. phil. Jens Kirchner for his kind effort, theoretical knowledge, leadership, patience, valuable ideas, and intensive guidance for more than three years.

I would also like to thank Prof. Dr.-Ing. Dr.-Ing. habil. Robert Weigel for allowing me to join his institute and affording all required components and types of equipment.

My sincere gratitude goes to Prof. Dr.-Ing. Robert Schober for his mental support. In addition, an Emerging Fields Initiative (EFI) project launched by Friedrich-Alexander-Universität (FAU) funded part of this work, which I heartily appreciate.

Furthermore, I want to thank Dr.-Ing. Harald Unterweger for conducting the experiments and preparing the superparamagnetic nanoparticles required for this work.

I wish to express my gratitude to the students whose theses have inspired me in this Ph.D. research: Niklas Schlechtweg and Charlotte Hintze.

I am so thankful to all the professors and colleagues who taught and supported me at the FAU Erlangen-Nuremberg, Institute for Electronics Engineering. I cannot express my respect and appreciation towards them for the knowledge, experience, suitable manner, and family-like atmosphere they gave me during my time at the university.

Last but not least, I would like to thank my whole family: father, siblings, nieces and nephews. Also, I heartily dedicate this thesis to the person who

has always been inspiring me, my mother, who took the lead to heaven but her love still surrounds me. May God bless her soul.

Abstract

Continuous monitoring of health status has become a demand to ensure early detection, diagnosis, and disease treatment. Molecular Communication (MC) system utilizes molecules or synthesized particles as information carriers, which can be considered an excellent alternative to the conventional communication systems in aqueous media such as the human body.

In this dissertation, based on the MC system, a macroscale aqueous-based testbed is used to imitate the propagation of biocompatible Superparamagnetic Iron Oxide Nanoparticles (SPIONs) through a human vessel for drug delivery applications, where the SPIONs are covered by drugs and released into the bloodstream to reach any targeted cells such as cancerous tumors. In the employed testbed, particle suspension stored in a syringe is pumped at different flow rates into a channel filled with water via one arm of a Y-connector. A stationary background flow enters the channel via its second arm and carries the particles to the receiver, i.e., susceptometer. All fundamentals required to understand the testbed's physics, including fluidics and magnetism, are discussed.

In a preliminary study, the testbed is simplified to a 2D rotationally symmetric model described mathematically, and its flow regime is analytically derived. A full numerical study of the simplified model is carried out. In order to avoid the computational complexity of the multiphysics simulations, a simple analytical solution is also provided to efficiently estimate the system response directly from the particle density and the magnetic field strength of the detector within its detection region. This analytical solution is compared against simulation.

In another study, a 3D simulation-based model of the testbed is given, from which the particle density during propagation is obtained and substituted into the analytical solution together with the magnetic field of the detector to estimate the system response, which is verified by the conducted experiments. Other detectors, including Helmholtz, Maxwell, and planar coils, are also considered. All employed coils are analytically and numerically studied. Varied positions, trajectories and distribution of particles are assumed inside their detection regions to obtain and analyze the corresponding system responses.

Some results are concluded as follows. The detected signal of the coils is directly proportional to the volume susceptibility and thus to the density of the particles in their detection regions. Changing the particle distribution inside the transmitter before being injected into the channel leads to various distributions inside the detector, significantly affecting the system response.

The best scenario is to inject the particles in the region between the tube center and its inner boundary. Also, the injection is recommended to end before or shortly after the particles enter the detector. The receiver should be longer than or of comparable length to the transmitter. Otherwise, some information will be lost. The sensitivity near the inner boundary of the cylindrical coils is generally higher than that about the center axis. Hence, it is recommended to be wrapped directly on the propagation tube. The signal is detected before the particles enter the short coils because the field is not limited to their inner cores. Directly after the Y-connector, the particles cover only one side of the propagation tube. In addition, increasing the background flowrate pushes the particles away from the tube center and reduces their density, weakening the detected signal accordingly. With large pipes, the time delay and detected pulse width increase. Also, turbulence should be taken into consideration. In the planar coils, the signal decays very quickly when moving vertically above their surfaces. The fields of the circular and square planar coils are rotationally symmetrical and limited to the regions above their surfaces. Distributing multiple numbers of planar coils around the tube can help strengthen the detected signal.

Kurzfassung

Eine kontinuierliche Gesundheitsüberwachung ist zu einer Voraussetzung geworden, um die Früherkennung, Diagnose und Behandlung von Krankheiten zu gewährleisten. Das MC System nutzt Moleküle oder synthetisierte Partikel als Informationsträger, die als hervorragende Alternative zu herkömmlichen Kommunikationssystemen in wässrigen Medien wie dem menschlichen Körper angesehen werden können.

In dieser Dissertation, die auf dem MC-System basiert, wird ein makroskaliges wässriges Testbed verwendet, um die Ausbreitung von biokompatiblen superparamagnetischen Eisenoxid-Nanopartikeln (SPIONs) durch ein menschliches Gefäß für Drug Delivery-Anwendungen zu imitieren, wobei die SPIONs abgedeckt werden durch Medikamente und in den Blutkreislauf freigesetzt werden, um gezielte Zellen wie Krebstumore zu erreichen. Im eingesetzten Testbed wird in einer Spritze gelagerte Partikelsuspension mit unterschiedlichen Flussraten über einen Arm eines Y-Verbinders in einen mit Wasser gefüllten Kanal gepumpt. Eine stationäre Hintergrundströmung tritt über seinen zweiten Arm in den Kanal ein und trägt die Partikel zum Empfänger, d. h. zum Suszeptometer. Alle Grundlagen, die zum Verständnis der Physik des Testbeds erforderlich sind, einschließlich Fluidik und Magnetismus, werden besprochen.

In einer Vorstudie wird das Testbed zu einem 2D- rotationssymmetrischen Modell vereinfacht, mathematisch beschrieben und dessen Strömungsregime analytisch abgeleitet. Eine vollständige numerische Studie des vereinfachten Modells wird durchgeführt. Um die Rechenkomplexität der Multiphysik-Simulationen zu vermeiden, wird auch eine einfache analytische Lösung bereitgestellt, um die Systemantwort direkt aus der Partikeldichte und der magnetischen Feldstärke des Detektors innerhalb seines Detektionsbereichs abzuschätzen. Diese analytische Lösung wird mit Simulationen verglichen.

In einer anderen Studie wird ein 3D-simulationsbasiertes Modell des Testbeds angegeben, aus dem die Partikeldichte während der Ausbreitung gewonnen und in der analytischen Lösung zusammen mit dem Magnetfeld des Detektors zur Abschätzung der Systemantwort verwendet wird, die durch die durchgeführten Experimente verifiziert wird. Andere Detektoren, einschließlich Helmholtz-, Maxwell- und Planarspulen, werden ebenfalls in Betracht gezogen. Alle verwendeten Spulen werden analytisch und numerisch untersucht. Es werden unterschiedliche Positionen, Flugbahnen und Verteilungen von Par-

tikeln innerhalb ihrer Detektionsbereiche angenommen, um die entsprechenden Systemantworten zu erhalten und zu analysieren.

Einige Ergebnisse werden wie folgt abgeleitet. Das detektierte Signal der Spulen ist direkt proportional zur Volumensuszeptibilität und damit zur Dichte der Partikel in ihren Detektionsbereichen. Eine Änderung der Partikelverteilung im Sender vor der Injektion in den Kanal führt zu unterschiedlichen Verteilungen im Detektor, die die Systemantwort erheblich beeinflussen. Das beste Szenario besteht darin, die Partikel in den Bereich zwischen der Mitte der Röhre und ihrer inneren Begrenzung einzuspritzen. Außerdem wird empfohlen, die Injektion vor oder kurz nach dem Eintritt der Partikel in den Detektor zu beenden. Der Empfänger sollte länger oder vergleichbar lang sein wie der Sender. Andernfalls gehen einige Informationen verloren. Die Empfindlichkeit nahe der Innengrenze der zylindrischen Spulen ist im Allgemeinen höher als die um die Mittelachse. Daher wird empfohlen, direkt auf das Ausbreitungsrohr gewickelt zu werden. Das Signal wird erfasst, bevor die Partikel in die kurzen Spulen eintreten, da das Feld nicht auf ihre inneren Kerne beschränkt ist. Direkt nach dem Y-Verbinder bedecken die Partikel nur eine Seite des Ausbreitungsrohres. Darüber hinaus werden die Partikel durch eine Erhöhung der Hintergrundströmungsrate von der Röhrchenmitte weggedrückt und ihre Dichte verringert, wodurch das detektierte Signal entsprechend geschwächt wird. Bei großen Rohren erhöhen sich die Zeitverzögerung und die erkannte Pulsbreite. Auch Turbulenzen sind zu berücksichtigen. Bei den Planarspulen klingt das Signal sehr schnell ab, wenn sie sich vertikal über deren Oberflächen bewegen. Die Felder der kreisförmigen und quadratischen Planarspulen sind rotationssymmetrisch und auf die Bereiche oberhalb ihrer Oberflächen beschränkt. Das Verteilen mehrerer Planarspulen um das Rohr herum kann das detektierte Signal verstärken.

Contents

List of Symbols and Abbreviations

List of Abbreviations

Abbreviation	Description
AC	Alternating Current
AI	Autoinducers
ATP	Adenosine Triphosphate
BAN	Body Area Network
BER	Bit Error Rate
CNT	Carbon Nanotubes
CSK	Concentration Shift Keying
DC	Direct Current
dMCS	distributed Molecular Communication Simulator
DNA	Deoxyribonucleic Acid
DPM	Delay to Peak Maximum
ECG	Electrocardiogram
EFI	Emerging Fields Initiative
EM	Electromagnetic
ER	Endoplasmic Reticulum
FAU	Friedrich-Alexander-Universität
FEM	Finite Element Method
Fl	Fluorescein
FRET	Förster Resonance Energy Transfer
GA	Golgi Apparatus
HBC	Human Body Communication
IDA	Increased Detection Algorithm
IM	Index Modulation
IoBNT	Internet of Bio-Nanothings
ISI	Inter-Symbol Interference

Abbreviation	Description
LTE	Lehrstuhl für Technische Elektronik
MC	Molecular Communication
MCvD	Molecular Communication via Diffusion
MIMO	Multi-Input Multi-Output
MoSK	Molecule Shift Keying
MSE	Mean Square Error
MUCIN	MolecUlar CommunicatIoN
OOK	On-Off Keying
PCB	Printed Circuit Board
PMFDHM	Peak Maximum of the detected signal to its Full Duration at Half Maximum
PPM	Pulse Position Modulation
PS	Fluorescent Polystyrene
QS	Quorum Sensing
RF	Radio Frequency
RhB	Rhodamine B
RX	Receiver
S-ATV	Sampling-based Adaptive Threshold Variation
SISO	Single-Input Single-Output
SPIONs	Superparamagnetic Iron Oxide Nanoparticles
SPIONs	superparamagnetischen Eisenoxid-Nanopartikeln
TX	Transmitter

List of Symbols

Symbol	Description
A_{Ch}	Cross-sectional area of the propagation tube (channel)
$2a_{\mathrm{R}}$	Length of the rectangular planar coil
A_{Sol}	Cross-sectional area of the solenoid
$\mathbf{B}_0$	Magnetic flux density vector when no magnetic materials exist
$\mathbf{B}$	Magnetic flux density vector
$2b_{\mathrm{R}}$	Width of the rectangular planar coil
c_{L}	Adjustment factor used to obtain the inductance of a short solenoid
c_0	Optimization factor used to estimate the particle density matrix $\nu(r, \varphi)$
L_{Ch}	Channel length
$\chi_{\mathrm{m}}^{\mathrm{Sim}}(i, j)$	Volume susceptibility of an ij-indexed compartment in the simulated channel
χ_{m}	Volume magnetic susceptibility
$\chi_{\mathrm{m}}^{\mathrm{Meas}}$	Initial volume susceptibility in the measurement
$C_{\mathrm{m}}(\mathbf{x}, t)$	Iron concentration of the SPIONs
c_s	Closed contour taken around the wire-turns of the solenoid
I	Electric current
$d\mathbf{A}$	Vector area whose direction is perpendicular to the cross-sectional area of the detector
ΔN_l	Wire-turns in slice number l within a subdivided solenoid
ΔZ_l	Width of slice number l within the subdivided solenoid
ρ_{f}	Fluid density
d_{h}	Variable that takes two values $\{-z_{\mathrm{h}}, z_{\mathrm{h}}\}$
D_h	Hydraulic diameter of a tube

Symbol	Description
dI	Electric current due to the infinitesimal length dz_S
$\mathcal{D}$	Diffusivity of particles or molecules
$d\mathbf{l}_s$	Infinitesimal element vector
d_{m}	Variable that takes two values $\{-z_{\mathrm{m}}, z_{\mathrm{m}}\}$
d_{P}	Diameter of a single particle of SPIONs
dz_S	Infinitesimal length of the solenoid
$E(k)$	Elliptic integral of the second kind
e_{P}	Mean square error between the actual and approximated particle density matrices
$\mathbf{F}_{\mathrm{ext}}$	External force vector applied to the fluid
Φ_{B_0}	Flux density of the field lines that pass through the air-core of the solenoid
$\mathbf{g}$	Acceleration acting on the continuum
$H(t)$	Unit step function
H_{c}	Coercive magnetic field
$\alpha - \mathrm{Fe_2O_3}$	Hematite
$\mathbf{H}$	Magnetic field strength vector
I_{m}	Electric current flows in the side loops of Maxwell coil
k_0	Constant of proportionality between the volume density and magnetic susceptibility
K_{a}	Anisotropy constant
K_{B}	Boltzmann constant
ν_{f}	Fluid kinematic viscosity
$K(k)$	Elliptic integral of the first kind
Kn	Knudsen number
k_{s}	Scaling parameter
k_{w}	Scaling factor that ensures a minimum MSE between the system responses of the fully numeric and fully analytic methods

Symbol	Description
L_0	Coil self-inductance (without particles)
λ	Mean free path length of the fluid molecules
L_{Ch}	Length of the propagation channel
L_{Char}	Characteristic length of a tube
$L_{h,\mathrm{Laminar}}$	Hydrodynamic entry length of Laminar flow
L_{ref}	Reference inductance
L_{RX}	Receiver length
L_{Sol}	Solenoid length
L_{Susc}	Detection length of the susceptometer
$L(t)$	Time-dependent inductance due to the propagation of particles
L_{TX}	Transmitter length
$\gamma - \mathrm{Fe_2O_3}$	Maghemite
$\mathrm{Fe_3O_4}$	Magnetite
$\mathbf{M}$	Magnetization vector
n_{a}	Number of dipole moments (atoms) per unit volume
m_{P}	Mass of a single particle of SPIONs
M_{r}	Remanent magnetization
M_{s}	Saturation magnetization
μ	Permeability of any material
μ_0	Permeability of free space
μ_r	Relative permeability
N	Total number of wire-turns of a coil
ρ_0	Initial particle density (inside the transmitter)
ρ_{Ch}	Particle density during propagation
$N_{\mathrm{Par.}}(t)$	Detected number of particles within the receiver
$\overline{\mu}_{\mathrm{atomic}}$	Net atomic dipole moment
N_l	Number of wire-turns in a thin solenoid
N_R	Number of wire-turns of a rectangular coil

Symbol	Description
N_t	Number of wire-layers in a thick solenoid
$n_z(l)$	Linear density of the wire-turns in slice number l within the subdivided solenoid
$\overline{\mu}_{\mathrm{m}}$	Orbital magnetic moment
$\rho_{\mathrm{Ch}}^{\mathrm{Sim}}(i,j)$	Particle volume density of an ij-indexed compartment in the simulated channel
Pe	Péclet number
φ	Angular coordinate
φ_A	Angle between $\mathbf{v}_A$ and x-axis
φ_S	Angle between $\mathbf{v}_S$ and x-axis
$\Pi(n,k)$	Elliptic integral of the third kind
ρ_0^{Meas}	Initial volume density of particle in the measurement
$\nu(r,\varphi)$	Estimated particle density matrix
$\mathrm{P}_{\varphi}(\varphi)$	Exact angular particle density vector
$A(\varphi)$	Estimated angular particle density vector
$\tilde{\mathrm{P}}_{\varphi}(\varphi)$	Approximated angular particle density vector
$\mathrm{P}_r(r)$	Exact radial particle density vector
$\mathbf{P}$	Pressure vector of the fluid
$R(r)$	Estimated radial particle density vector
$\tilde{\mathrm{P}}_r(r)$	Approximated radial particle density vector
ρ_0^{Sim}	Initial volume density of particle in the simulated transmitter
p_{w}	Wetted perimeter of a tube
Q_{BG}	Stationary background flow rate
$Q_{\mathrm{Ch}}(t)$	Time-dependent channel flow rate
$Q_{\mathrm{Inj},0}$	Injection flow rate of particles
$Q_{\mathrm{Inj}}(t)$	Time-dependent injection flow rate
r	Radial coordinate
r_0	Superparamagetism (unstable) critical radius

Symbol	Description
R_2	Solenoid outer radius
r_A	Radial component of the vector $\mathbf{v}_A$
r_c	Single domain critical radius
R_Ch	Radius of the propagation channel
Re	Reynolds number
$R_\mathrm{Helmholtz}$	Radius and length of Helmholtz coil
$\mathrm{P}_0(r,\varphi)$	Exact particle density matrix
$\rho_\mathrm{l}(z,t)$	Particle linear density
$\rho_\mathrm{v}(\mathbf{x},t)$	Particle volume density
$r_\mathrm{i}(z,t)$	Inner radius of the parabolic velocity profile
R_Loop	Radius of a current loop
R_Maxwell	Radius of the main (large) loop of Maxwell coil
R_m	Radius of the side (small) loops of Maxwell coil
$r_\mathrm{o}(z,t)$	Outer radius of the parabolic velocity profile
(r,φ,z)	Cylindrical coordinates
R_RX	Receiver radius
r_S	Radial component of vector $\mathbf{v}_S$
R_Sol	Solenoid inner radius
r_sp	Superparamagetism (stable) critical radius
R_N	Radius of the circular planar coil
R_i	Radius of loop number i within the circular planar coil
R_Susc	Radius of the susceptometer
R_TX	Transmitter radius
$s_0(t)$	System response for $L_\mathrm{ref} = L_0$
ΔR	Solenoid thickness
$\overline{\mu}_\mathrm{B}$	Spin magnetic moment
$s(t)$	System response
T	Temperature
t	Time variable

Symbol	Description
T_{B}	Blocking temperature
T_{BG}	Time required by the particles to reach the receiver after the injection ends
T_{C}	Curie temperature
T_{D}	Time delay between transmitter and receiver
θ_{m}	Angle between the easy axis and the particle's magnetization
T_{Inj}	Duration of particle injection
T_{max}	Time required to reach the peak maximum
T_{N}	Néel temperature
T_{Th}	Time required by the particles to reach the receiver during the injection
u_{avg}	Average propagation velocity
u_{max}	Maximum velocity at the tube-center
$u(r)$	Fully developed parabolic velocity of laminar flow
$\mathbf{v}$	Relative position vector
$\mathbf{v}_A$	Position vector of the field point A
$\mathbf{U}$	Velocity vector of the fluid
V_{Inj}	Injection volume of the SPIONs suspension
μ_{f}	Fluid viscosity
V_{p}	Volume of the particle
$\mathbf{v}_S$	Position vector of the source point S
$W_{\mathrm{B_{fm}}}$	Anisotropic energy barrier of ferromagnetic particles
$W_{\mathrm{B_{spm}}}$	Anisotropic energy barrier of superparamagnetic particles
W_{Th}	Thermal energy
$w(z)$	Sensitivity curve of the detecting solenoid
X	Number of the radial sections in the segmented channel

Symbol	Description
Y	Number of the angular sections in the segmented channel
Z	Total number of slices in the subdivided solenoid
z	Axial coordinate
z_0	Initial position of the particle parabolic profile before propagation
z_A	Axial component of the vector $\mathbf{v}_A$
z_{h}	Half the length (or radius) of Helmholtz coil
z_{m}	Half the length of Maxwell coil
z_S	Axial component of the vector $\mathbf{v}_S$

List of Figures

List of Tables

1 Introduction

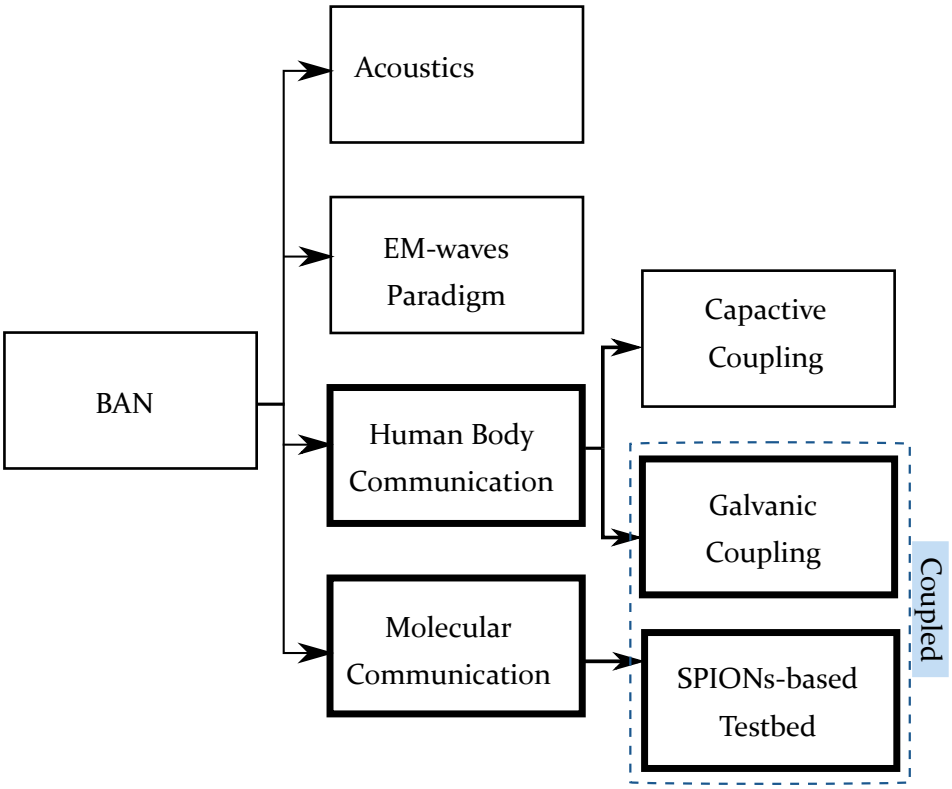

Figure 1: Different communication paradigms used in the BAN network.

1.1 Body Area Networks

Real-time monitoring and promotion of human health require full coverage and control of the vital processes in the human body. Body Area Network (BAN) [108] is a communication network that covers the human body, where biosignals such as heart rate or glucose level are exchanged between sensors placed in/on or at the proximity of the body. The communication in this network can be subdivided into either intra-body communication between small-scale devices placed in/on the body, which might also be able to communicate with the biological cells, or off-body communication between the on-body devices and macroscale devices placed nearby and connected to the internet. To communicate with biological cells, nanotechnology is integrated with synthetic biology to create biocompatible nanoscale communication

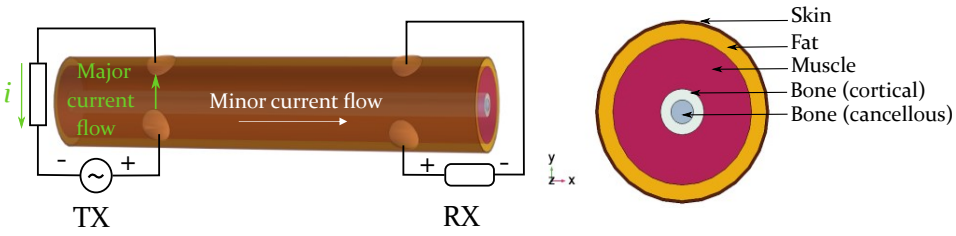

Figure 2: HBC galvanic coupling through a simulation-based model of the human arm.

devices. For instance, nanorobots are supposed to perform simple, valuable tasks such as communication, information sharing, data storing, and/or computing.

Different communication paradigms, seen in Fig. 1, can be used to establish a BAN network, namely acoustic wave transmission, Electromagnetic (EM) waves paradigm, Human Body Communication (HBC), and Molecular Communication (MC).

Acoustic waves at inaudible frequencies (ultrasound) experience low attenuation in water compared to EM waves. Therefore, they are currently used for in-body communication [65, 86]. However, the human tissues absorb the propagated wave, which accordingly heats them. For temperatures above 38.5 °C, adverse biological effects might occur [47].

In the EM waves paradigm, antennas are typically used in the Radio Frequency (RF) band for data transmission. However, the antenna size is inversely proportional to the carrier frequency. Hence, to be able to communicate at the nanoscale, newly developed nanomaterials are needed to design nanoscale antennas that transmit data at extremely high frequencies. For instance, Carbon Nanotubes (CNT)/graphene-based antennas [17, 59] work in the terahertz band with a resonant frequency up to two orders of magnitude lower than the noncarbon-based antennas. Nevertheless, such antennas are not practical for in-body applications due to their bio-incompatibility. Also, EM waves highly attenuate in aqueous media such as the human body, i.e., path loss exponent up to 8 and higher [89]. Besides, high power consumption is required for data transmission, which is not applicable within the body and might harm the human tissues. Therefore, the EM paradigm would be more appropriate for off-body applications that require a high data rate and consume a large amount of power.

Antennas are replaced by electrodes in the HBC system, which exploits the dielectric properties of the human body to send information through the tissues at low frequencies, up to tens of megahertz [150]. This technique promises less interference and low power consumption. There are mainly two types of HBC [128], namely capacitive and galvanic coupling. Each of which incorporates four electrodes, two of which are placed at the transmitting and receiving sides. Through the former method, only one electrode at both sides of the communication link is placed on the body, while the other two electrodes are float in the air. Therefore, part of the signal is transmitted through the conductive body tissues, while a capacitive return path through the surroundings represents the other part. This capacitive path may reduce the system robustness such that any change in the surrounding environment affects the received signal. In capacitive coupling, no direct contact with the skin is needed. In contrast, in the galvanic coupling approach (Fig. 2), all electrodes should be in direct contact with the body. An Alternating Current (AC) that follows the human safety regulations is injected through the transmitting electrodes into the human tissues. The injected current causes a primary current flow between the two transmitting electrodes and a small secondary current that propagates further into the conductive tissues in the receiver's direction, causing an alternating potential difference between its electrodes, from which the required information is extracted. Galvanic coupling does not depend on the surrounding environment and has less interference because the signal is confined to the body.

MC system is inspired by nature, where biological cells communicate through molecular signaling to achieve a particular task such as control of hormonal activities or cell division [123]. MC incorporates molecules or synthesized particles as information carriers rather than electric, optical, or EM waves used in traditional communication systems. Hence, the MC system overcomes their drawbacks for the in-body applications. In MC, a Transmitter (TX) releases molecules into an aqueous or gaseous environment, which propagate until being detected and decoded by a Receiver (RX). Nanomachine is the most basic communication unit in the MC system, which is used to develop and build more complex systems such as nanorobots. Each nanomachine is supposed to have a set of instructions that describe its task. Several nanomachines will communicate inside the human body, forming a bio-nanonetwork [11].

1.2 Thesis Motivation

The interaction between the bio-nanonetworks, MC-based network, and the already existing traditional communication networks is called the Internet of

Bio-Nanothings (IoBNT) [9, 32]. IoBNT is going to provide real-time monitoring for healthcare applications. Data about the health status are collected through an MC-based network (intra-body) and sent to an external device or medical center (off-body) for being analyzed. However, the realization of such networks faces many challenges, including the development of nanomachines with nanoscale integrated batteries and transceivers, understanding and engineering the new MC communication paradigm, mitigate interference due to the tremendous biological processes in the body, ensure secure data transmission, and building an interface between the in-body and off-body devices (bio-cyber interface) to export the detected signals externally.

One solution to the bio-cyber interface problem is to couple both MC and HBC systems to externally obtain the detected signal from the body. For instance, as seen in Fig. 3, for drug delivery applications, a repository of biocompatible Superparamagnetic Iron Oxide Nanoparticles (SPIONs) that convey drugs can be implanted inside the body or attached to a human vessel. If triggered, it releases an appropriate volume of particle suspension, hence the drug, into the bloodstream. Due to the magnetic properties of the nanoparticles, they can be detected using a small-scale solenoid wrapped around the vessel. The detected electrical signal, e.g., potential difference, can be further resent via the galvanic coupling HBC (through the transmitting electrodes) to an external device placed on the body, e.g., smartwatch embedded with the receiving electrodes. In the case of superficial veins, a planar coil can be used directly for particle detection. The particles can be externally controlled using electromagnets, which will help protect the healthy cells from the side effects of the drugs. Other sensors can also be distributed on the body to collect the vital signs regularly. The collected data are sent to a medical center via RF propagation techniques. For in-body communication, power can be harvested directly from the body or wirelessly transmitted using interrogator (passive responder) schemes.

1.3 Thesis Aims

This manuscript focuses only on the SPIONs-based MC system in fluids. A platform (testbed) that imitates the particle propagation through the bloodstream is employed, in which the SPIONs are detected using a susceptometer, i.e., solenoid. The modeling of the fluidic channel and optimizing the detecting coils are covered. Different FEM models are built to separately study each part of the system, i.e., transmitter, channel, and receiver.

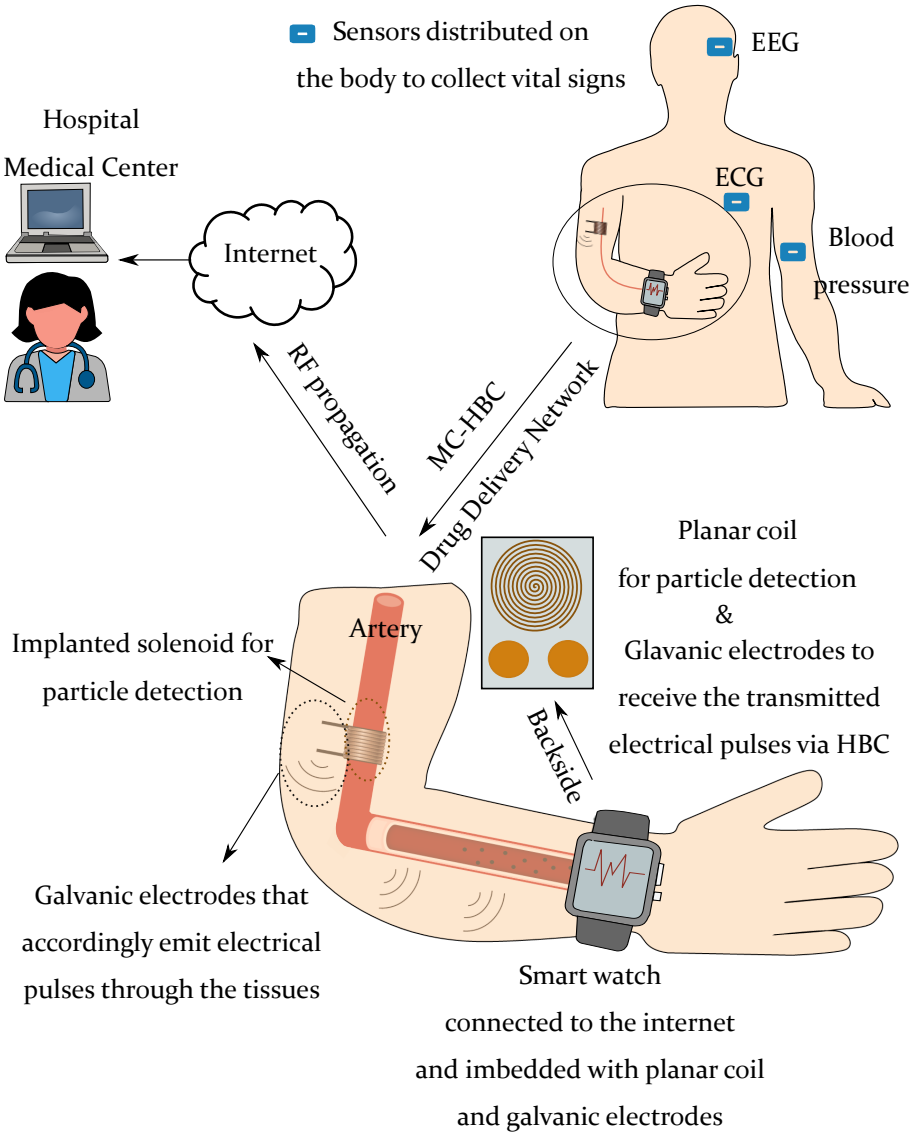

Figure 3: Proposed solution for in-body/off-body interface problem by coupling both the MC and HBC communication systems. RF propagation is used to externally export the detected signal to a hospital or medical center.

As a proof of concept, a brief study on the galvanic coupling HBC system is provided in [3, 5]. An FEM model of the human arm is built in COMSOL Multiphysics to study the transmission mechanism of the electrical signals through the human tissues. The arm is approximated by a cylinder of 5 different layers (Fig. 2): skin, fat, muscle, cortical bone, and cancellous bone. The dielectric properties of each tissue are derived from the summation of 4 Cole-Cole expressions that describe the complex relative permittivity of the different tissues at different frequencies. In [3], the study is aimed to investigate how changing the type and thickness of tissues, through which the signal is transmitted, affects the received signal. Moreover, some bending is introduced to the model to mimic the elbow. This model is extended in [5] to include inter-body communication between two arms in touch, i.e., to exchange information between different bodies. Several key parameters are studied, including the applied frequency, contact area, and transmission length.

1.4 Thesis Structure

This manuscript is organized as follows.

- Chapter 1 introduces the communication paradigms used in the BAN networks. Also, it includes the motivation and aim of the dissertation.
- Chapter 2 describes the cell signaling between the biological cells. In addition, it lists some of the biomedical applications of MC. Finally, it surveys most of the theoretical and experimental studies conducted in the literature, including the SPIONs-based testbed.
- In Chapter 3, the fundamentals related to the testbed are discussed, including the fluid mechanics, magnetic properties of SPIONs, and theoretical derivation of the magnetic fields of all employed detectors.
- In Chapter 4, the testbed is simplified to a 2D-rotationally symmetric model described mathematically, and its essential equations, such as the propagation profile of the SPIONs and estimated system response, are analytically derived.
- Two types of coils are used for particle detection: cylindrical coils wrapped around the vessel or planar coils placed on its outer surface. Chapter 5 presents simulated models for the coils and analyzes their magnetic fields within the detection region to study their detection mechanism. Also, the system responses due to the movement of parti-

cles through the detection region of each coil are obtained for different applied scenarios.

- In addition to the measurements, three main computational schemes can be utilized to estimate the system response, namely fully numerical, fully analytical, and hybrid. The schemes are described and discussed in detail in Chapter 6. Afterwards, the simulation is experimentally validated.
- Chapter 7 sets the design guidelines and optimization strategy for the transmitter, channel, and receiver.
- Finally, Chapter 8 concludes this work and proposes some ideas for future work.

2 Molecular Communication

2.1 Introduction

An organism contains many parts that make up that whole. The human body is mainly composed of cells, which are independently functioning units that use MC to communicate with each other through the release of molecules or chemical compounds. To understand the communication mechanism of biological cells, i.e., bio-nanomachines, the functionalities of their organelles are investigated.

2.1.1 Biological Cells

An animal eukaryotic cell, shown in Fig. 4, mainly contains [123]:

- Cytosol: intracellular fluid in which the cell organelles are suspended. The cytosol contains water and ions, in addition to high amounts of charged molecules and proteins.
- Cytoplasm: it is the cell's interior, including the cytosol and all organelles.
- Nucleus: it contains chromosomes that carry most of the genes in the form of Deoxyribonucleic Acid (DNA).
- Endoplasmic Reticulum (ER): it is subdivided into rough and smooth ER. Rough ER includes ribosomes that produce proteins based on

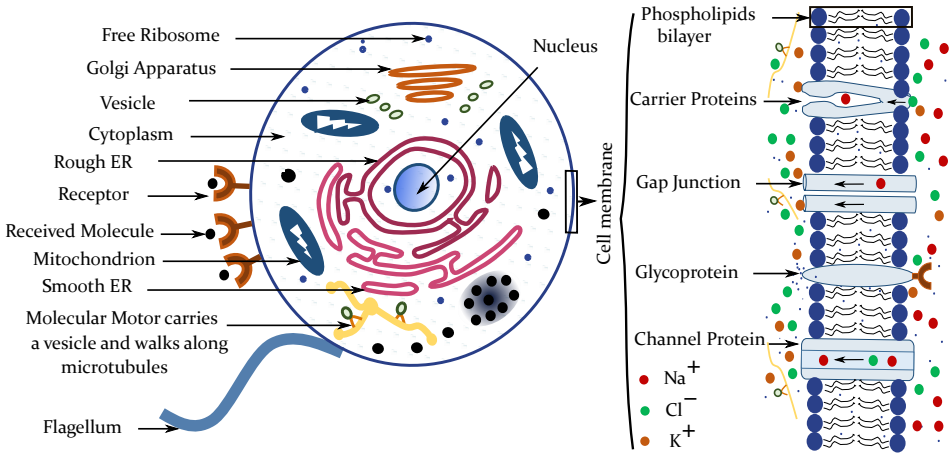

Figure 4: Structures of an animal cell (left) with a detailed view of its membrane (right).

the information from the DNA. Smooth ER is involved in different metabolism processes, e.g., detoxification of drugs and poisons.

- Golgi Apparatus (GA): it is extensively found in cells specialized for secretion to receive, modify, encode and send the products of the ER, e.g., proteins, to another destination.
- Mitochondria: they are mainly responsible for the generation of Adenosine Triphosphate (ATP) from sugars and fats with the help of oxygen, i.e., cell respiration. ATP supports the cell with the energy required to drive its processes.
- Plasma membrane: a selectively permeable membrane that surrounds the cell to control which substances enter or leave its domain. It is composed of phospholipid molecules, which are subdivided into hydrophilic charged heads and hydrophobic uncharged tails. Diverse proteins are embedded into the membrane or attached to its surface, such as channel proteins that provide hydrophilic gated channels to allow only particular solutes to pass through it. Also, carrier proteins change their shapes using ATP energy to pump substances from one side to another side of the membrane. Some membrane proteins are used to establish a communication channel between different cells using various kinds of junctions, e.g., gap junction. In addition, certain types of membrane proteins have receptors that recognize only specific shapes of signaling molecules, i.e., hormones. The distribution and concentration of anions and cations differ on both sides of the membrane, resulting in membrane potential, i.e., from -50 to -200 mV.
- Cytoskeleton: it is a network of fibers that maintains the shape of the cell. It extends throughout the cytoplasm to organize its activities, location, and structure. It contains hollow rods (microtubules) made up of tubulin proteins, on which some protein motors can walk across the cell. Molecules secreted from the GA are encapsulated in transport vesicles and carried by molecular motors, i.e., dynein, that move along the microtubules until reaching the plasma membrane, with whom the vesicles fuse to release their secretory proteins out of the cell. Specialized arrangements of microtubules give either flagella or cilia, which extend from some cells and act as locomotors appendages.

2.1.2 Cell Signaling

Biological cells utilize MC to perform a particular task or function within the human tissues. The cell signaling is mainly classified into five types (Fig. 5)

based on the transmission distance between the sender and receiver [10, 12, 25]:

1. Intracrine (tens to hundreds of nm): the communication occurs within the same cell. For instance, molecular motors use chemical reactions to generate energy and allow directional transportation of data packets, i.e., vesicles, along the microtubules.
2. Autocrine (tens to hundreds of nm): both sender and receiver belong to the same cell, which secretes signaling molecules that bind to its receptors, e.g., the autocrine secretion of the cancerous cells.
3. Juxtacrine (nm – μm): intercellular communication, where the sending and receiving cells are in contact. One example of such MC systems is the transmission of calcium signaling molecules (Ca^{2+}) through the gap junctions between adjacent cells.
4. Paracrine (μm – mm): the transmitter and receiver are close to each other but not directly connected. For example, via a process called conjugation, the DNA information, i.e., plasmids, are loaded onto bacterial motors that travel via another process called chemotaxis in the receiver's direction following its released molecules, i.e., chemoattractants. Another example of paracrine signaling is neurochemical transmission, where neurotransmitters, i.e., small molecules, are released at junctions (synapses) between two nerve cells to send an impulse.
5. Endocrine (mm – m): macroscale communication mechanism, which is the focus of this dissertation, in which the transmitter and receiver are relatively distant. For instance, dozen of endocrine glands and tissues transmit different hormone molecules through the bloodstream or extracellular fluids among the whole body to control muscle growth, heart rate, and menstrual cycles. Another example is the transmission of pheromones through the air to allow plants and many mammals to communicate with members of the same species.

2.2 Biomedical Applications

MC systems are expected to enable new revolutionary applications in different fields, namely environmental, industrial, military, and entertainment [111, 120, 144]. However, due to its biocompatibility and superiority over other communication systems in aqueous mediums, e.g., the human body, the importance of MC strongly appears in biomedical applications [22, 40, 44, 101, 109, 110], some of which are stated below.

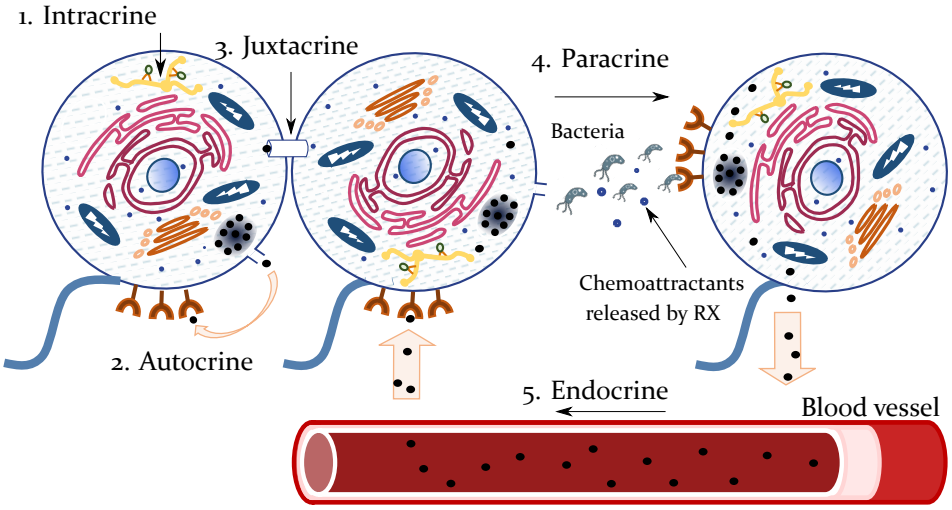

Figure 5: Different methods for cell signaling.

Replace organs and repair damaged tissues Synthetic bio-devices such as micro and nanoscale robots are supposed to be manufactured and distributed inside the body to repair organs or lost tissues (tissue engineering). A central unit will detect any failure or injury in the tissues and accordingly send instructions to the nanorobots to start the healing process. The deployed nanorobots may also be able to sense and interact with the organs to fix any failure in their communication.

Immune system support and health monitoring The immune system is considered a bio-nanonetwork with several bio-nanomachines to identify and control foreign objects. The existence of specific molecules within the bloodstream can be biomarkers for a particular disease. Therefore, developed nanomachines that use molecular communication can be implanted in the body to regularly collect and transmit information about the status of the bio-molecules to external devices for being analyzed.

Drug delivery systems As introduced in section 1.2, the MC system can also be used to deliver drugs carried by SPIONs (or any other synthesized molecules) to diseased tissues in the body. An electrical signal stimulates a drug repository that releases some of its contents into the bloodstream. A confirmation signal is received when the drug is delivered. The amount and release rate of drug can be also wirelessly controlled and monitored via MC.

Localization of infected cells Bacteria can localize sources of particular types of molecules through the conjugation and chemotaxis processes (paracrine

signaling). If the molecules were biomarkers released by cancerous cells, they will be easily detected and localized by using bacteria or synthesized nanosensors.

Modify the gene sequences of humans MC system will pave the way for manipulating and modifying nanostructures such as the human gene sequences to add or suppress some of its functionalities, providing notable therapeutic advantages. For instance, bio-chips will be used to read the old gene sequences, modify them and produce new genetically modified genes with sophisticated functionalities, i.e., process (Lab)-on-a-chip.

2.3 Literature Review

Before realizing the applications of MC, it is essential to understand this new communication paradigm. The MC system is composed of three main components shown in Fig. 6: a transmitter to release information molecules into the environment, a receiver to decode the transmitted molecules, and a channel where the information molecules propagate. However, each physical component of the system is further subdivided into smaller modules or blocks; each of which is responsible for a particular task. This section summarizes some of the theoretical studies available in the literature for MC. Also, the simulation tools developed for studying MC as well as the experimental platforms are given, including on-chip and tabletop MC systems.

2.3.1 Theoretical Studies

The different blocks of the MC system, shown in Fig. 6, have been extensively studied in the literature. This subsection briefly describes the basic functionality of each block and surveys the relevant literature.

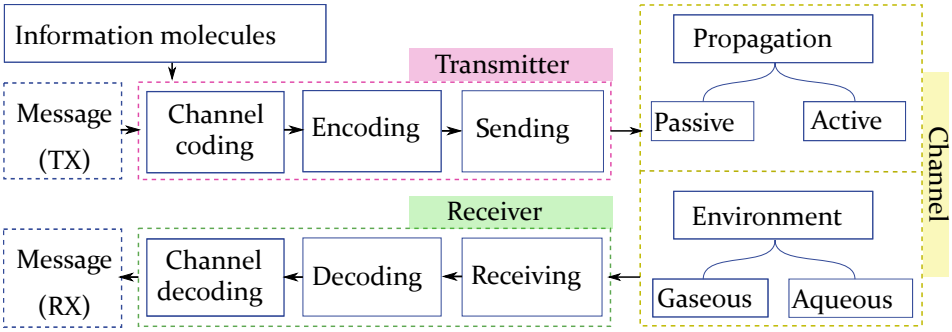

Figure 6: Block diagram of a typical MC system.

In the MC system, a message that carries information such as sensed parameters, specific events, sets of instructions, and/or data storing commands are transmitted through the channel. Each message should represent a predefined structure at both transmitter and receiver. The message is carried from the sender to the receiver by information molecules, which can be either organic compounds, such as hormones, proteins and lipids, or synthetically engineered materials, such as chemical compounds and nanoparticles made of sophisticated materials, e.g., gold or magnetite. For biocompatibility, the particles can be encapsulated in lipid vesicles to separate them from the surrounding environment [39].

Unlike the EM waves, the signaling molecules are physical elements that can be stored in a repository and placed at the transmitter. In open-loop systems, the amount of signaling molecules will be limited; hence they should be consumed efficiently and eliminated quickly from the system with no or negligible side effects.

Some of the transmitted molecules that belong to previous time durations may remain in the channel and affect the upcoming symbol durations, causing Inter-Symbol Interference (ISI). To ensure robust communications and enhance the reliability of the transmitted data, additional information is added before the data is sent, i.e., channel coding. This information is used at the receiver to recover the transmitted bit sequence and correct any errors introduced during transmission. Different error correction codes are considered in the literature [30, 92, 130]. Other studies propose using enzymes [112, 145] or photolysis reactions [28] to degrade the information molecules so that they do not interfere with future transmissions.

The transmitted message is encoded (modulated) on the properties of the information molecules, namely the type, quantity, and release time. The corresponding modulation schemes for these properties are respectively called Molecule Shift Keying (MoSK) [79], Concentration Shift Keying (CSK) [79], and Pulse Position Modulation (PPM) [6]. However, to achieve higher information rates and mitigate the ISI, it is possible to encode the message on any combination of these physical quantities [71, 107]. Advanced modulation schemes are also developed for MC, in which the message is encoded on the spatial index of the transmitters, i.e., Index Modulation (IM) [55, 63], the permutation of multiple types of molecules [134], and the releasing order of different molecules [13], e.g., bit "0" is encoded by a molecule of type "A" followed by type "B", while reversing the order of the released molecules encodes bit "1". A combination of IM and PPM modulation schemes is given in [56].

However, the system complexity increases rapidly for high-order modulation schemes, which might be challenging at the nanoscale.

In response to an external stimulus such as temperature, light, or electric signal, the transmitter releases the information molecules, according to the chosen modulation scheme, into an aqueous or gaseous environment by either unbinding them or opening a molecular gate that allows them to propagate. During the propagation, the molecules might be affected by the velocity, viscosity, temperature, pH level, and/or pressure of the flow introduced to the environment. The signaling molecules should be synthesized to be immune to any changes, noise, or other matters in the system. The propagation through the channel can be either passive or active.

Passive propagation includes Molecular Communication via Diffusion (MCvD), where the information molecules diffuse randomly in all directions via Brownian motion from regions of high concentrations to regions of low concentrations [66, 133, 140]. In macroscale MC that involves a large number of information molecules, diffusion can be described by Fick's second law. While in microscale MC, where the number of released molecules is small, diffusion can be accurately simulated using Monte Carlo simulation [39]. In MCvD, no external power supplies are required because the signaling molecules use the thermal energy in the surrounding environment to diffuse through the channel. Hence, they may take a long time to reach the destination, resulting in a low bit rate transmission.

In contrast to MCvD, active propagation requires energy suppliers to overcome the thermal noise in the environment. It is subdivided into advection-based (also called flow-based diffusion, or diffusion with drift), bacteria-based propagation [18, 53], and transport using molecular motors [61, 105]. In the advection-based propagation, a flow is introduced to the environment, which speeds up the propagation of molecules and ensures a transmission for long distances with a relatively high bit rate. Also, because the propagation is directed, fewer molecules are needed compared to the diffusion-based mechanism.

Different mechanisms are used to capture the information molecules from the channel, including, but not limited to, the permeable absorbing receiver that considers the number or concentration of the received molecules [146], the reversible adsorbing receiver that binds to a specific type of information molecules [124], and reversible adsorbing and desorbing receiver that adsorbs specific molecules near its surface and desorbs previously adsorbed ones [29]. According to the chosen modulation scheme, the captured molecules or

particles are decoded into an output signal, e.g., electric, electrochemical, fluorescent light, or chemical reactions that may produce new molecules to perform a particular task or to be further transmitted to another receiver.

Because of the tedious work of the experimental studies that may also be expensive and time-consuming, different simulators are developed to model large and complex MC systems. NeuroSim is a neuronal signaling simulator used for nanoscale intrabody sensor networks [132]. Bacteria-based simulators include NanoNs3 [68] and BNSim [141]. Diffusion-based propagation simulators include distributed Molecular Communication Simulator (dMCS) [7], N3sim [88] and MolecUlar CommunicatIoN (MUCIN) [147]. However, to simulate the diffusion with drift inside the blood vessels, BINs2 simulators are used [42, 43] as well as COMSOL Multiphysics simulation tool, which has been chosen to run all the required simulations in this dissertation.

2.3.2 Experimental Studies

As mentioned before, MC has been extensively theoretically studied over the past several years. However, most of this work has not been translated into practical and experimental systems. This subsection summarizes most of the experimental platforms available in the literature in either gaseous or aqueous channels.

2.3.2.1 On-Chip MC Systems

The inherent advantages of miniaturization as well as the promising applications of on-chip MC systems have motivated researchers to conduct studies in this field. Generally, on-chip MC can be classified into two main categories [37]: microfluidic devices and active transport schemes using molecular motors [35].

A subcategory of the microfluidic on-chip MC systems includes those that depend on the bacterial Quorum Sensing (QS) process, i.e., the production, sensation, and detection of Autoinducers (AI) signaling molecules. In [8], synthetically engineered *E. coli* bacteria confined in two separable compartments are connected through a microfluidic channel. Upon stimulation, transmitting bacteria release AI molecules through the channel to be detected by the receiving bacteria that fluoresce once the molecules arrive with a specific concentration. Other QS-based microfluidic MC systems are considered in [15, 16, 77, 114].

Another subcategory of the microfluidic MC is the droplet microfluidics, in which discrete volumes of fluids that carry the information are dispersed

into a continuous stream of another immiscible fluid [60]. One of the first practical studies of droplet-based communication is conducted in [58], where an external pressure pump is used to inject colored drops of water into a microfluidic channel of continuous oil flow. An optical microscope with an integrated high-speed camera is used as a detector. This model is further updated in [19, 45, 57]. Other detection schemes are also considered in the literature, such as capacitance sensors [34, 64]. Nevertheless, the droplets are replaced in [33] by Fluorescent Polystyrene (PS) micro-beads, which are released into the channel via programmable syringe pumps and detected by an inverted fluorescence microscope.

2.3.2.2 Gaseous-based Tabletop Platforms

MC system considers mainly two transmission ranges, i.e., channel length, namely microscale (nm-mm) and macroscale (mm-km) communication. To the best of the author's knowledge, only macroscale gas-based platforms are available in the literature.

One of the first works on engineering the macroscale experiments, which mimics the insect infochemical communication system, is introduced in [41] by N. Farsad et al. As shown in Fig. 7a, a message is entered using a microcontroller that controls the release of alcohol molecules from an electronic spray into a channel of maximum length 4 m according to the On-Off Keying (OOK) modulation scheme, i.e., presence or absence of signaling molecules to decode bit "1" or "0", respectively. A fan is placed behind the spray to introduce a flow that speeds up the propagation of molecules (flow-based diffusion). Three different sensors are used to detect the transmitted signal. The maximum data rate achieved is 0.3 bps. The testbed is extended in [76, 84, 85] to include Multi-Input Multi-Output (MIMO) system for bit rate improvement. However, due to the ISI and inter-link interference, the improvement is not significant, i.e., $\approx$ 0.5 bps without drift and $\approx$ 0.7 bps with drift. A new detection mechanism, namely Increased Detection Algorithm (IDA), is introduced in [149] to mitigate the impact of ISI for a channel of maximum length 80 cm without drift. Another detection algorithm called Sampling-based Adaptive Threshold Variation (S-ATV) is given in [117], which shows better Bit Error Rate (BER) performance of shorter bit intervals compared to the IDA algorithm applied in [149]. In another study [121], the performance of MC in complex confined structural environments (metallic containers) is compared with EM waves (Zigbee). The results show that MC offers a good alternative to the EM system in such environments with a maximum bit rate of 0.1 bps. Another comparison between EM and MC systems is conducted in [54], considering a

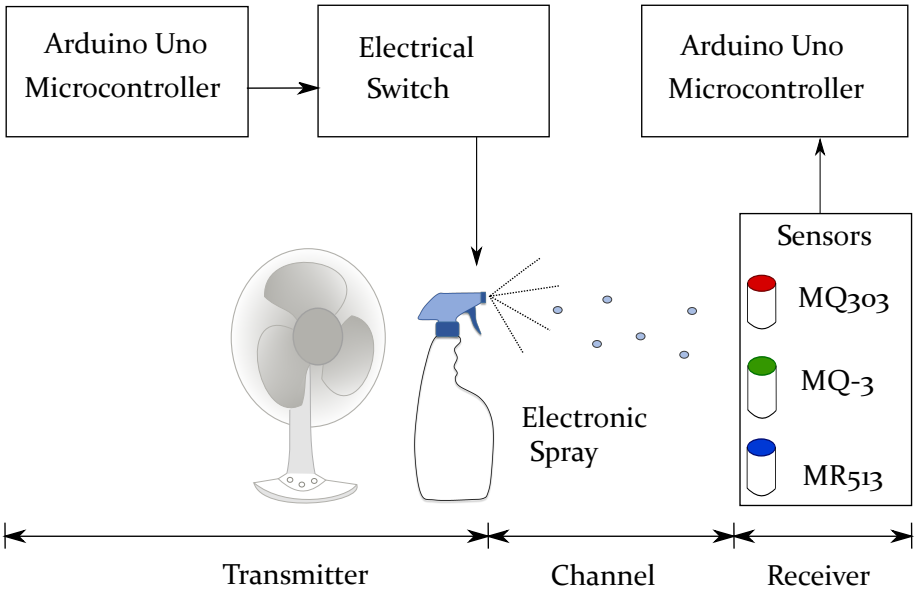

(a) Open air channel

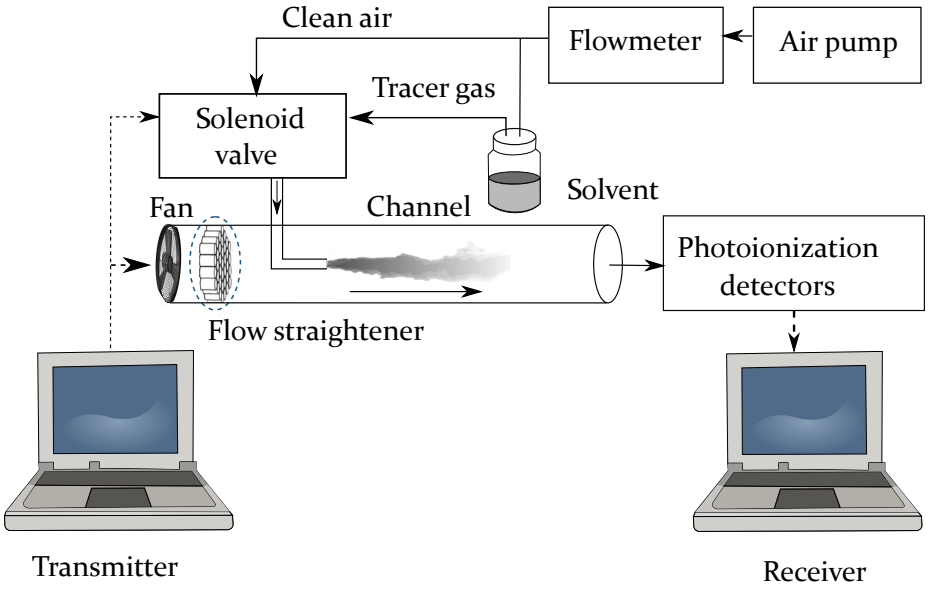

(b) Tubular channel

Figure 7: Schematic diagram of macroscale gaseous-based testbeds with different channels.

pipe channel, a knife-edge channel, and a mesh channel. It concludes that, for a lossy copper pipe, the attenuation per unit length is relatively low in the case of MC compared to EM. Referring also to Farsad's testbed, the effect of vertical propagation for a relatively short channel of length 10 cm is studied in [90, 91]. Moreover, in [119], a movable transmitter mounted on an RF-remotely controlled chassis is proposed to prove that bits disorder (transposition) occurs in mobile MC systems due to the slow propagation rate relative to the speed of the movable transceivers.

A refined version of Farsad's testbed is introduced and developed in [72, 115, 129] (see Fig. 7b), where solvent vapors (isopropyl alcohol) are released into a tubular channel of length 3.5 m and detected by multiple numbers of susceptible photoionization detectors. The injection of the vapor flow is controlled by a solenoid valve and regulated by a variable-area flowmeter, while the bulk airflow is controlled by a fan fixed at the transmitting end of the tube. The environment is assumed to be turbulent. However, to create a laminar flow, hundreds of straws (flow straighteners) are placed in front of the fan. The maximum bit rate achieved is 20 bps at a transmission length of 1.4 m using the OOK modulation scheme and Karhunen-Loeve method for decoding. This model is improved in [116] by using a different detection scheme, doubling the bit rate, i.e., 40 bps.

Another gaseous-based MC testbed derived from Farsad's setup is given in [48], where olfactory signals are transmitted from an odor emitter through a tubular channel and received by a mass spectrometer with a quadrupole mass analyzer. A range of volatile organic compounds are considered at different temperatures, flow rates, and tube sizes for a transmission distance up to 3 m. Two different modulation schemes are employed, namely OOK and CSK. The fundamental parameters of the system, such as the carrier flow rate and bit duration, are studied in [96]. This system is further analyzed both experimentally and theoretically in [97, 98], while the open-air transmission and noise analysis are given in [95].

2.3.2.3 Aqueous-based Tabletop Platforms

Aqueous-based MC promises to replace the radio-based systems in regions where EM waves are not visible or experience high losses, such as underwater, in-body, or inside sewer pipelines. Driven by this, micro and macroscale aqueous-based testbeds are proposed and investigated in the literature as described below.

Microscale Platforms One of the most promising testbeds that provides bit rate up to 150 kbps is proposed in [80]. Based on Förster Resonance Energy Transfer (FRET) mechanism, a nano-channel is established in an ethanol solvent. Highly concentrated Fluorescein (Fl) and Rhodamine B (RhB) dye molecules are employed as TXs and RXs, respectively. When the transmitting molecules are exposed to an optical signal, they accordingly transmit the information in the form of excitons, which are received by the RhB molecules, whose fluorescence signals are decoded by a distant photodetector. Other microscale aqueous-based platforms that, however, depend on the bacterial QS process are given in [51, 52, 87].

Macroscale Platforms To imitate the bloodstream in vessels, a multi-chemical testbed (Fig. 8a) is proposed in [38], where peristaltic pumps are used to inject different liquids, i.e., bases and acids, into a tube filled with a stationary water flow. The information is encoded in the pH level of the received signal. This testbed is extended in [62, 82, 83] to include the MIMO system. For mimicking the water flow in sewer pipelines, as proposed in [73], hydrochloric acid molecules are released into a large-scale semi-cylindrical channel of length and radius 2 m and 10 cm, respectively. In [139], saline molecules are used as information carriers detected by an electrical conductivity reader. Other macroscale aqueous-based testbeds are given in [1, 2, 14], where fluorescent particles are used as information carriers detected by optical sensors.

None of the above mentioned testbeds is valid for targeted drug delivery applications. Motivated by this, a SPIONs-based testbed is introduced in [138], which is dissertation's focus. A schematic diagram of the testbed is shown in Fig. 8b, in which three tubes are connected via a Y-connector, namely particle, background, and propagation tubes. One peristaltic pump is used to maintain a stationary flow of water in the channel, mimicking the bloodstream in a vessel. A second pump is responsible for the injection of SPIONs suspension into the flow. The propagation tube goes through a susceptometer that generates an electrical signal when the particles travel through its core. After the detection of particles, they are removed from the environment and collected in a waste bin. Other detection schemes for this testbed rather than the susceptometer are proposed in [20, 21]. In the next chapter, the theoretical fundamentals of this testbed, such as fluid mechanics and magnetism, are given.

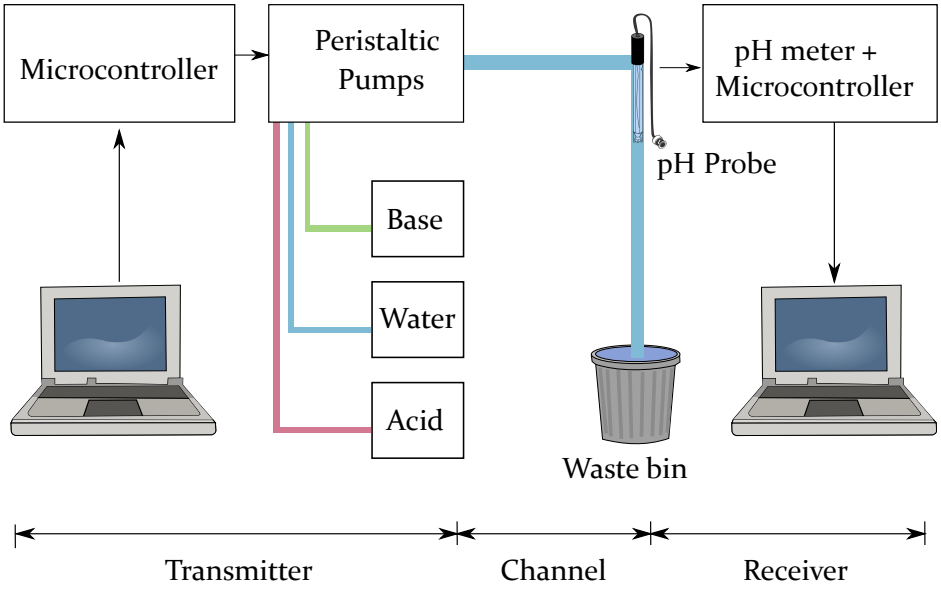

(a) Chemical-based testbed

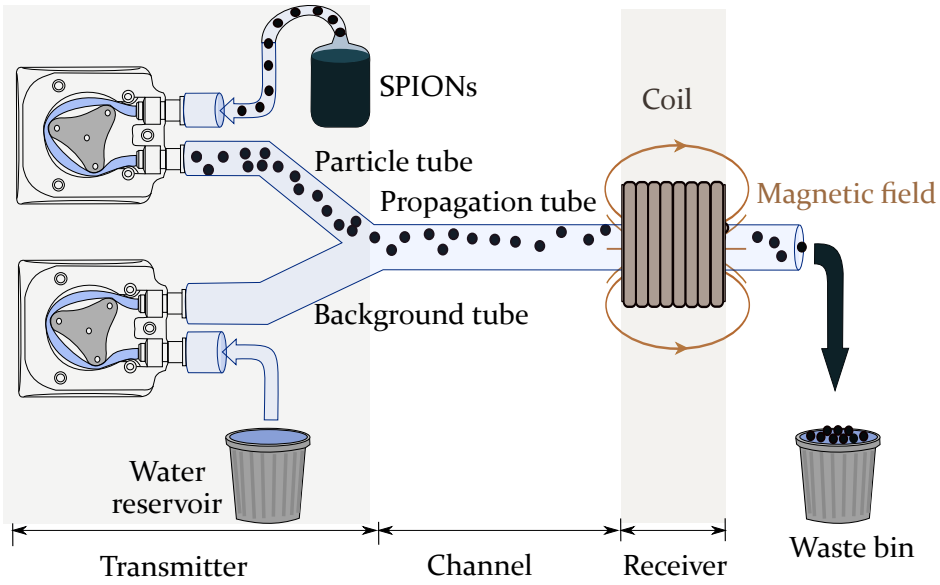

(b) SPIONs-based testbed

Figure 8: Schematic diagram of macroscale aqueous-based testbeds.

3 Fundamentals

3.1 Fluid Mechanics

This section outlines the parameters used to describe the fluid properties. Also, it describes the different flow regimes in pipes, i.e., circular tubes. Besides, it introduces important dimensionless numbers used in fluid mechanics.

3.1.1 Fluid Properties

3.1.1.1 Density

Fluids can be either gases or liquids. A fluid is described as an *incompressible fluid* if changes in its density during propagation are negligible [23]. In contrast to gases, the density of liquids is not highly dependent on pressure [31]. Therefore, all liquids are considered *incompressible fluids*, except at very high pressures.

3.1.1.2 Viscosity

Viscosity describes the friction between the fluid's different layers as well as the friction with its surroundings. It also measures the fluid resistance to deforming (flow) due to applied shear stress. If the relation between the applied shear stress and rate of shearing strain (velocity gradient) is linear, the fluid is called *Newtonian fluid*, e.g., water, air, and oil. Viscosity μ_f of a fluid is related to its density ρ_f through

$$\nu_f = \frac{\mu_f}{\rho_f} \tag{1}$$

where ν_f is called the fluid kinematic viscosity. For water [142], $\nu_f = 1.01 \times 10^{-6}$ m²/s at 1 atm and 20 °C.

3.1.2 Flow Regimes

There are typically three types of fluid flow regimes: laminar, transitional, and turbulent (see Fig. 9).

Laminar flow (also called viscous flow) is usually observed at low velocities and is characterized by smooth parallel streamlines with highly ordered motion and small molecular diffusion [27]. Also, a solution to its velocity profile can be analytically derived.

On the other hand, turbulent flow is usually observed at relatively high velocities. Besides, it depends on the pipe roughness, width, and fluid viscosity. It is characterized by mixed streamlines, velocity fluctuations in directions other than the main flow direction, and highly disordered motion.

When the flow fluctuates between laminar and turbulent, it is then called transitional.

3.1.3 Navier-Stokes Equation

Navier-Stokes equation is a second-order nonlinear partial differential equation that governs the motion of *Newtonian-incompressible* fluids (water) in pipes, and it is given by [142]

$$\underbrace{\rho_{\mathrm{f}}\left(\frac{\partial \mathbf{U}}{\partial t}+(\mathbf{U}\cdot\nabla\mathbf{U})\right)}_{\text{Inertial force}}=\underbrace{-\nabla\mathbf{P}}_{\text{Pressure force}}+\underbrace{\rho_{\mathrm{f}}\,\mathbf{g}}_{\text{Gravity force}}+\underbrace{\mu_{\mathrm{f}}\nabla^2\mathbf{U}}_{\text{Viscous force}}+\underbrace{\mathbf{F}_{\mathrm{ext}}}_{\text{External force}} \tag{2}$$

In cylindrical coordinates (r,φ,z), it is defined by

$$\rho_{\mathrm{f}}\left(\frac{\partial \mathbf{U}}{\partial t}+\left(u_r\frac{\partial \mathbf{U}}{\partial r}+\frac{u_\varphi}{r}\frac{\partial \mathbf{U}}{\partial \varphi}+u_z\frac{\partial \mathbf{U}}{\partial z}\right)\right)=-\left(\frac{\partial \mathbf{P}}{\partial r}+\frac{1}{r}\frac{\partial \mathbf{P}}{\partial \varphi}+\frac{\partial \mathbf{P}}{\partial z}\right)+\rho_{\mathrm{f}}\,\mathbf{g}$$
$$+\mu_{\mathrm{f}}\left(\frac{1}{r}\frac{\partial}{\partial r}\left(r\frac{\partial \mathbf{U}}{\partial r}\right)+\frac{1}{r^2}\frac{\partial^2\mathbf{U}}{\partial \varphi^2}+\frac{\partial^2\mathbf{U}}{\partial z^2}\right)+\mathbf{F}_{\mathrm{ext}} \tag{3}$$

with

$$\mathbf{U}=\mathbf{e}_r u_r+\mathbf{e}_\varphi u_\varphi+\mathbf{e}_z u_z \qquad \text{and} \qquad \mathbf{P}=\mathbf{e}_r p_r+\mathbf{e}_\varphi p_\varphi+\mathbf{e}_z p_z \tag{4}$$

where $\mathbf{U}$ and $\mathbf{P}$ are the velocity and pressure of the fluid, respectively; while $\mathbf{g}$ is the body accelerations acting on the continuum such as gravity, and $\mathbf{F}_{\mathrm{ext}}$ is any other external force that influences the fluid. In order to find the velocity profile of the flow in the propagation tube, the Navier-Stokes equation is solved together with the *incompressible* continuity equation defined by [142]

$$\nabla\cdot\mathbf{U}=\frac{1}{r}\frac{\partial}{\partial r}(ru_r)+\frac{1}{r}\frac{\partial}{\partial \varphi}(u_\varphi)+\frac{\partial}{\partial z}(u_z)=0 \tag{5}$$

3.1.4 Characteristic Numbers in Fluid Mechanics

3.1.4.1 Knudsen Number

Navier-Stokes equation is valid only if the fluid is continuum, which can be determined using the Knudsen number Kn [122]

$$\mathrm{Kn} = \frac{\text{Mean free path length}}{\text{Characteristic length}} = \frac{\lambda}{L_{\mathrm{Char}}} \tag{6}$$

The mean free path length λ of the fluid molecules is the distance taken by one molecule before encountering a collision event with a second molecule, approximated for water by $\lambda \approx 0.31\,\mathrm{nm}$. The characteristic length L_{Char} of the tube equals its hydraulic diameter D_h [148]

$$L_{\mathrm{Char}} = D_h = \frac{4A_{\mathrm{Ch}}}{p_{\mathrm{w}}} \overset{\text{Circular tubes}}{=} 2R_{\mathrm{Ch}} \tag{7}$$

where A_{Ch} is the cross-sectional area of the propagation tube (channel), whose radius and wetted perimeter are R_{Ch} and p_{w}, respectively.

Knudsen number is of particular interest to assess the boundary conditions required to solve Eq. (2). For instance, for $\mathrm{Kn} < 0.001$, the relative movement between the tube wall and the fluid layer in its contact is zero, i.e., no-slip boundary condition. For $0.001 < \mathrm{Kn} < 0.1$, slip boundary condition is assumed. Otherwise, the Navier-Stokes equation is not valid.

3.1.4.2 Reynolds Number

Reynolds number Re is the primary parameter used to predict the transition between the different flow regimes, which is defined by [142]

$$\mathrm{Re} = \frac{\text{Inertial force}}{\text{Viscous force}} = \frac{u_{\mathrm{avg}} \cdot L_{\mathrm{Char}}}{\nu_{\mathrm{f}}} \overset{(7)}{=} \frac{u_{\mathrm{avg}} \cdot 2R_{\mathrm{Ch}}}{\nu_{\mathrm{f}}} \tag{8}$$

where u_{avg} is the average velocity of the propagating flow.

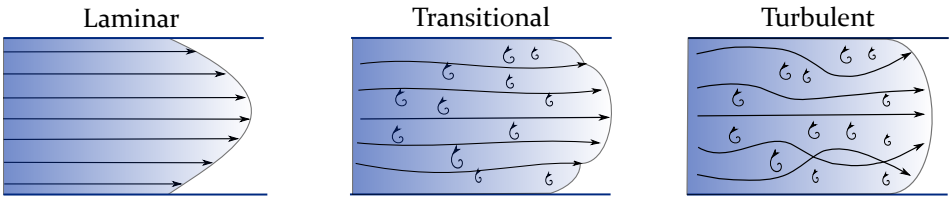

Figure 9: Fluid velocity profile for different flow regimes in pipes.

Under most practical conditions in circular tubes, laminar flow is obtained if $\mathrm{Re} < 2300$; fully turbulent flow is obtained if $\mathrm{Re} > 10000$; while in between, the flow is considered transitional. However, in some cases, the flow becomes fully turbulent for $\mathrm{Re} > 4000$ [148].

3.1.4.3 Péclet Number

The motion of particles in a fluid is governed by both advection and diffusion. Advection versus diffusion dominance can be determined by the Péclet number Pe [122]

$$\mathrm{Pe} = \frac{\text{Advection transport}}{\text{Diffusion transport}} = \frac{\mathrm{Re} \cdot \nu_\mathrm{f}}{\mathcal{D}} \overset{(8)}{=} \frac{u_\mathrm{avg} \cdot 2R_\mathrm{Ch}}{\mathcal{D}} \tag{9}$$

where $\mathcal{D}$ is the diffusivity of the magnetic nanoparticles, which for the considered SPIONs has the value of less than 10^{-11} m²/s.

For a channel of length L_Ch, advection dominates if [118]

$$\mathrm{Pe} \gg \frac{L_\mathrm{Ch}}{2R_\mathrm{Ch}} \tag{10}$$

hence the particles travel with the flow faster than they spread out.

3.1.5 Laminar Flow in Tubes

As will be derived in Chapter 4, the propagation flow in the employed testbed is laminar. However, the laminar velocity profile goes through various phases until it is fully developed. In the following two subsections, a derivation is given to find the fully developed velocity profile. Moreover, the distance required by the flow to fully develop is specified.

3.1.5.1 Fully Developed Velocity Profile

The fully developed laminar velocity profile inside the propagation tube is derived from the Navier-Stokes equation. First, two boundary conditions are applied, namely a no-slip boundary condition and a rotationally symmetric model, i.e., $\frac{\partial}{\partial \varphi} = 0$. Second, five assumptions are made: sufficiently long tube such that the flow is fully developed; the flow is steady, i.e., $\frac{\partial}{\partial t} = 0$; in laminar flow, the velocity field lines are axially parallel, therefore $u_r = 0$; constant pressure gradient is assumed in the z-direction, i.e., $\frac{dP}{dz} = \text{constant}$; the gravitational force is neglected, and no external forces are applied.

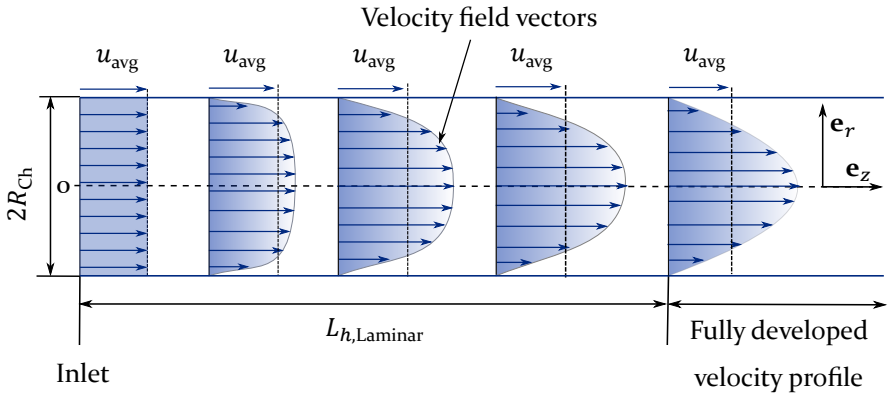

Figure 10: Schematic diagram of the different flow phases of laminar velocity profile inside the tube until it is fully developed. Longer arrows denote higher flow rates.

Applying the assumptions and boundary conditions into Eq. (3), Eq. (4), and Eq. (5) yields [148]

$$\frac{\mu_f}{r}\frac{d}{dr}\left(r \cdot \frac{d}{dr}u(r)\right) = \frac{dP}{dz} \tag{11}$$

After integrating Eq. (11) twice and applying the boundary conditions, the fully developed velocity $u(r)$ of laminar flow is obtained from

$$u(r) = \frac{r^2}{4\mu_f} \cdot \frac{dP}{dz} - \frac{R_{Ch}^2}{4\mu_f} \cdot \frac{dP}{dz} \tag{12}$$

$$= -\frac{R_{Ch}^2}{4\mu_f} \cdot \frac{dP}{dz} \cdot \left(1 - \left(\frac{r}{R_{Ch}}\right)^2\right) \tag{13}$$

$$= u_{max} \cdot \left(1 - \left(\frac{r}{R_{Ch}}\right)^2\right) \tag{14}$$

where u_{max} is the maximum velocity at the tube center, which is defined by

$$u_{max} = -\frac{R_{Ch}^2}{4\mu_f} \cdot \frac{dP}{dz} = 2 \cdot u_{avg} \tag{15}$$

From this derivation, we see that the fully developed laminar velocity profile in circular tubes is parabolic. In addition, pressure decreases in the direction of the flow, i.e., $\frac{dP}{dz}$ is negative.

3.1.5.2 Hydrodynamic Entry Length

Consider the fluid entering the propagation tube at a uniform velocity u_{avg}, as seen in Fig. 10. Due to the boundary conditions and friction between the adjacent fluid layers, the flow passes through different phases until it is fully developed. The distance taken by the flow to develop its velocity profile is called hydrodynamic entry length $L_{h,\text{Laminar}}$, and it is defined by [148]

$$L_{h,\text{Laminar}} \approx 0.05\text{Re} \cdot 2R_{\text{Ch}} \tag{16}$$

3.2 Magnetization

This section explains the origin of magnetism in matter as well as the classifications of the magnetic materials and their properties, i.e., specifically superparamagnetism. Also, it gives approximate analytical solutions and analysis of the magnetic fields for different coils, i.e., cylindrical and planar.

3.2.1 Magnetism in Matter

In atoms, as shown in Fig. 11, the motion of electrons contributes to two different types of magnetic moments: spin magnetic moment $\overline{\mu}_{\text{B}}$ associated with the spin of the electron around its axis, which can be in an "up" or "down" direction [102] and orbital magnetic moment $\overline{\mu}_{\text{m}}$ due to the orbital motion about the nucleus [26]. The net atomic dipole moment $\overline{\mu}_{\text{atomic}}$ is calculated by the vector sum of the orbital and spin magnetic moments. Due to the vector quantity of the magnetic moments, they may cancel each other such as in nonmagnetic materials. Magnetization $\mathbf{M}$ in [A/m] of a collection of identical atoms is a vector quantity used to describe the net dipole moment per unit volume [99]

$$\mathbf{M} = n_{\text{a}}\overline{\mu}_{\text{atomic}} \tag{17}$$

where n_{a} is the number of dipole moments (atoms) per unit volume. In addition, $\mathbf{M}$ is an intrinsic material property that describes the magnetic response of a material when exposed to an external magnetic field strength $\mathbf{H}$ in [A/m]

$$\mathbf{M} = \chi_{\text{m}}\,\mathbf{H} \tag{18}$$

where χ_{m} is the magnetic susceptibility of the material through which the field lines go. The magnetic field in the presence of a magnetic material is described by [93]

$$\mathbf{B} = \mu_0\,(\mathbf{H} + \mathbf{M}) \tag{19}$$

where **B** in [T] (Tesla) is the magnetic flux density of the magnetic material from both **H** and **M**, while $\mu_0 = 4\pi \times 10^{-7}$ H/m is the permeability of free space. From Eq. (19) and Eq. (18), the magnetic flux density is further defined by

$$\mathbf{B} = \mu_0 \left(1 + \chi_\mathrm{m}\right) \mathbf{H} = \mu_0 \mu_r \mathbf{H} = \mu \mathbf{H} \tag{20}$$

where μ is the permeability of the material and μ_r is its relative permeability. If no magnetic materials exist, i.e., $\chi_\mathrm{m} = 0$, the magnetic field density becomes

$$\mathbf{B}_0 \overset{(20)}{=} \mu_0 \mathbf{H} \tag{21}$$

3.2.2 Classifications of Magnetic Materials

The classification of magnetic materials is determined through the way the local atomic moments couple to each other and to an externally applied magnetic field (see Fig. 12). Magnetic materials can be classified into three main categories: diamagnetic, paramagnetic, and ferromagnetic materials. The latter has two additional subclasses: antiferromagnetic and ferrimagnetic from which superparamagnetic materials are obtained.

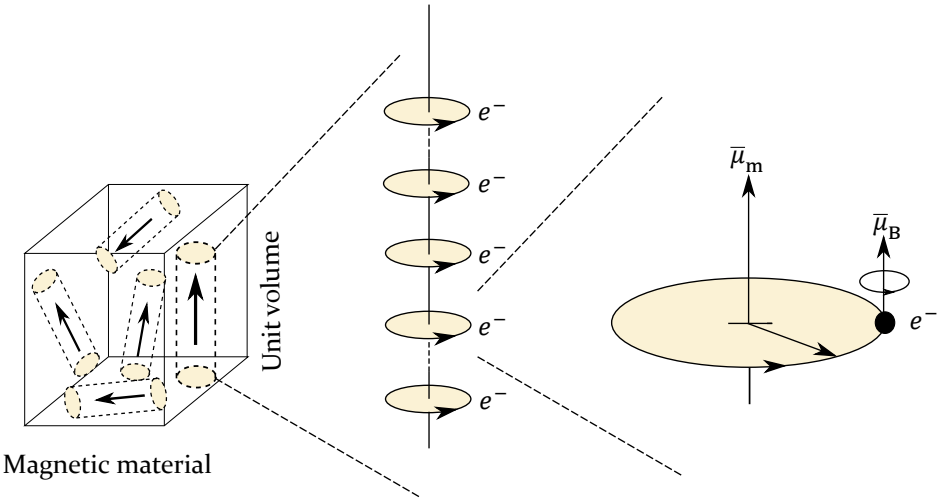

Figure 11: Spinning and orbiting magnetic moments that exist in a unit volume of a magnetic material, own presentation inspired by [113].

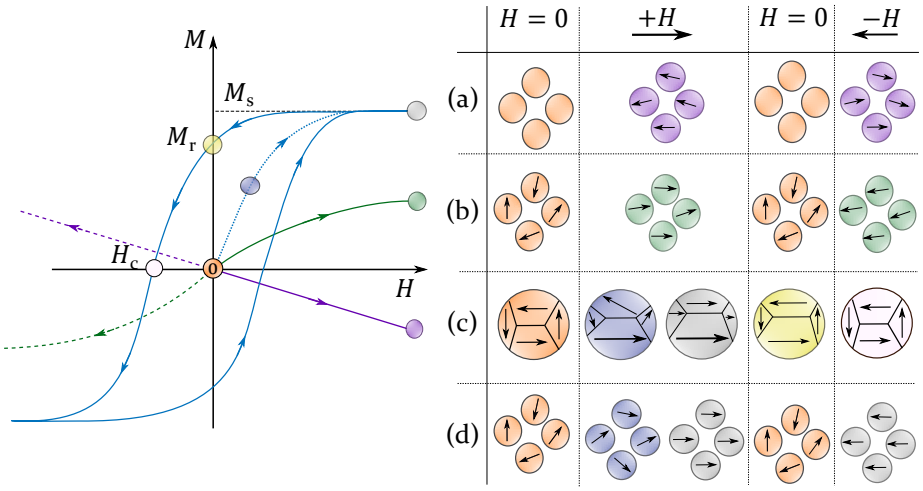

Figure 12: *M*-*H* curve that shows the different magnetization states for different materials: (a) diamagnetic, (b) paramagnetic, (c) ferromagnetic, and (d) superparamagnetic materials.

3.2.2.1 Diamagnetic Materials

Diamagnetic materials have no permanent magnetic moments in the absence of the field, as seen in Fig. 12a. However, when exposed to an external magnetic field, they show very weak magnetization in the opposite direction to the field, i.e., attracted towards the regions where the field is weak or repelled by strong fields. Examples of diamagnetic materials are water, silver, copper, and silicon [26]. Their magnetic susceptibility is in the range of $\chi_{\mathrm{m}} \approx -10^{-5}$ [69].

3.2.2.2 Paramagnetic Materials

Paramagnetic materials have randomly oriented dipoles, partially aligning with the applied magnetic field [67], as seen in Fig. 12b. However, when the field is removed, the random arrangement of the magnetic moments is retained without any remanence. Their magnetic susceptibility ranges from $\chi_m = 10^{-5}$ to 10^{-3} [69].

3.2.2.3 Ferromagnetic Materials

Ferromagnetic materials have domains over which all moments are essentially parallel, and in between some walls separate the domains. The direction of the magnetization in each domain is different. As seen in Fig. 12c, when a ferromagnetic sample is exposed to a magnetic field, the field introduces motion to the walls to expand the domains of the largest component of *M*

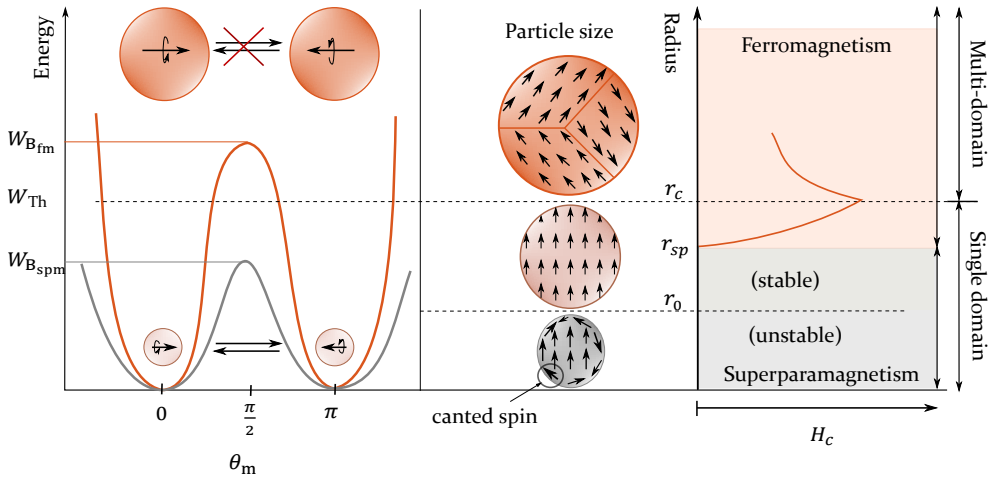

Figure 13: Variation of energy and coercive magnetic field for different particle sizes, own presentation inspired by [67, 103, 113].

along H [26, 113]. The saturation state is reached if the motion of domain walls is completed and all magnetization vectors are rotated to be in the same direction of the applied field, i.e., easy axis. The maximum induced magnetic moment during the exposure to the field is called the saturation magnetization M_s, which is highly dependent on temperature. When the magnitude of the applied field is reduced, most of the rotated magnetization vectors return to their original directions. However, the wall motion is an irreversible and lossy process that shows hysteresis. Therefore, a residual magnetization M_r remains in the sample even when the applied field is removed. To restore the initial state of the sample, an inverse coercive magnetic field H_c should be applied. Typical ferromagnetic materials at room temperature are iron, nickel, and cobalt, whose magnetic susceptibility is in the range of $\chi_m \approx 50 - 10000$ [69].

Compositions of iron oxides are called ferrimagnetic materials (ferrite), including magnetite (Fe_3O_4) and maghemite ($\gamma - Fe_2O_3$), whose magnetic moments are anti-parallel and have different values [78, 135]. However, when the magnetic moments are anti-parallel but equal in magnitude, the materials are called antiferromagnetic, e.g., hematite ($\alpha - Fe_2O_3$), which have poor magnetic properties and hence play a minor role in biomedical applications [36]. The magnetic properties of ferri- and ferromagnetic materials are retained until an ordering temperature called the Curie temperature T_C, above which their magnetic behavior becomes paramagnetic [137]. The corresponding value for the antiferromagnetic materials is called Néel temperature T_N.

3.2.2.4 Superparamagnetic Materials

Magnetite and maghemite can be used to synthesize magnetic nanoparticles of significant magnetic properties based on their sizes [75].

As seen in Fig 13, in large size multi-domain ferromagnetic particles, the anisotropic energy barrier ($W_{\mathrm{B_{fm}}} = K_{\mathrm{a}} V_{\mathrm{p}} \sin^2\theta_{\mathrm{m}}$) is higher than the thermal energy ($W_{\mathrm{Th}} = K_{\mathrm{B}} T$), where K_{a} is the anisotropy constant, V_{p} is the volume of the particle, θ_{m} is the angle between the easy axis and the particle's magnetization, K_{B} is Boltzmann constant and T is temperature. Therefore, residual magnetization remains in the particles even when the applied field is removed, corresponding to hysteresis.

However, if the particle size is reduced to be below a critical value r_{c}, it will possess only a single domain with a noticeable decrease in H_c until it becomes zero at a radius r_{sp}, where the particle behaves as a paramagnet with much higher saturation magnetization because it is originated from the ferromagnetic materials. This property is called superparamagnetism, e.g., SPIONs. The decrease in H_c is due to the absence of the domain walls, i.e., the reversal of the magnetic moments is realized only by the spin rotation [143]. For magnetite, r_{c} is about 128 nm [104].

In contrast to the large particles made of ferromagnetics, the thermal fluctuations in superparamagnetic nanoparticles, at temperatures above the so-called blocking temperature T_{B}, overcome the anisotropy energy barrier ($W_{\mathrm{B_{spm}}}$) and easily reverse the direction of the spin magnetic moments [70, 103]. There are two types of dipole relaxation: Brownian relaxation that takes place only in liquids, where the entire particle rotates, and Néel relaxation, in which only the magnetic moment vector aligns [137]. SPIONs are close in the magnetization properties to their large ferromagnetic counterparts but with no coercivity [143]. In addition, their magnetic moments show a stronger response to the applied field and hence higher magnetic susceptibility compared to the paramagnetic materials [75].

When the size of the single-domain particle is further reduced to be below another critical value r_0, the saturation magnetization is also reduced due to the so-called spin canting effect, i.e., the surface spins are tilted about their axis by certain angles instead of being parallel to each other [106, 126], resulting in unstable SPIONs.

3.2.3 Magnetic Fields Derivation

3.2.3.1 Biot-Savart Law

An electric current flow I through a straight wire results in a magnetic flux density $\mathbf{B}$ around it. This magnetic field is described using Biot-Savart law [127]

$$\mathbf{B} = \frac{\mu_0}{4\pi} \oint \frac{I d\mathbf{l}_S \times \mathbf{v}}{|\mathbf{v}|^3} \tag{22}$$

where $d\mathbf{l}_s$ is a vector line segment of the wire and $\mathbf{v}$ is a position vector representing the distance between an observation (field) point and the wire segment (source).

3.2.3.2 Current Loop

Assume the wire is wrapped to form a circular loop of radius R_{Loop}, placed horizontally on the xy-plane, as shown in Fig. 14. The position vector $\mathbf{v}_A$ of the field point A is defined by

$$\mathbf{v}_A = \mathbf{e}_{r_A} r_A + \mathbf{e}_z z_A \tag{23}$$

while the current segment $I\mathrm{d}\mathbf{l}_S$ of the loop is located at a source point S, whose position vector $\mathbf{v}_S$ is defined by

$$\mathbf{v}_S = \mathbf{e}_{r_S} r_S + \mathbf{e}_z z_S \tag{24}$$

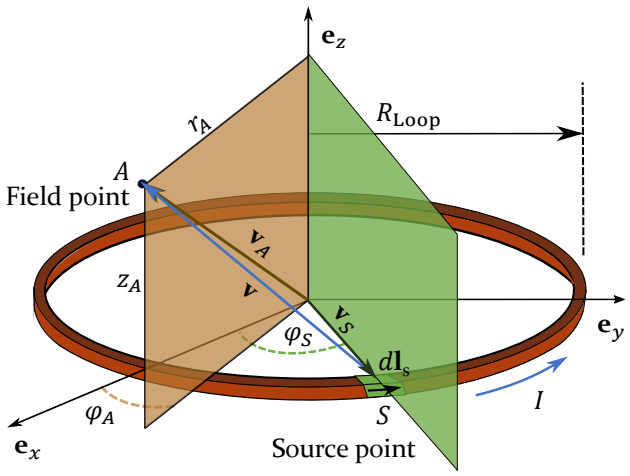

Figure 14: Schematic view of a current-carrying wire loop used to derive its magnetic field at an observation point A.

For a loop of a negligible thickness, r_S can be replaced by R_{Loop}. From Eq. (23) and Eq. (24), the relative position vector $\mathbf{v}$ is found from

$$\mathbf{v} = \mathbf{v}_A - \mathbf{v}_S = \mathbf{e}_{r_A} r_A + \mathbf{e}_z (z_A - z_S) - \mathbf{e}_{r_S} R_{\text{Loop}} \tag{25}$$

whose magnitude is given by

$$|\mathbf{v}| = \sqrt{r_A^2 + R_{\text{Loop}}^2 + (z_A - z_S)^2 - 2 r_A R_{\text{Loop}} \cos(\varphi_A - \varphi_S)} \tag{26}$$

The loop-segment vector $d\mathbf{l}_S$ is defined by

$$d\mathbf{l}_S = \mathbf{e}_{\varphi_S} R_{\text{Loop}}\, d\varphi_S \tag{27}$$

Because of the rotational symmetry of the loop, its magnetic field has equal values at any observation angle φ_A, which for simplicity is chosen to be zero. Hence, φ_S can be replaced by φ that changes from 0 to 2π. Substituting Eq. (25), Eq. (26) and Eq. (27) into the Biot-Savart law defined by Eq (22), the magnetic field $\mathbf{B}(\mathbf{v}_A)$ due to the current loop is calculated by

$$\mathbf{B}(\mathbf{v}_A) = \frac{\mu_0}{4\pi} \int_0^{2\pi} I R_{\text{Loop}} \frac{\left[\mathbf{e}_{r_S} (z_A - z_S) + \mathbf{e}_z \left(R_{\text{Loop}} - r_A \cos\varphi\right)\right] d\varphi}{\left[r_A^2 + R_{\text{Loop}}^2 + (z_A - z_S)^2 - 2 r_A R_{\text{Loop}} \cos\varphi\right]^{\frac{3}{2}}} \tag{28}$$

whose radial $B_r(\mathbf{v}_A)$ and axial $B_z(\mathbf{v}_A)$ components are derived respectively from

$$B_r(\mathbf{v}_A) = \mathbf{e}_{r_A} \cdot \mathbf{B}(\mathbf{v}_A) \tag{29}$$

$$= \frac{\mu_0}{4\pi} \int_0^{2\pi} I R_{\text{Loop}} \frac{[(z_A - z_S)\cos\varphi]\, d\varphi}{\left[r_A^2 + R_{\text{Loop}}^2 + (z_A - z_S)^2 - 2 r_A R_{\text{Loop}} \cos\varphi\right]^{\frac{3}{2}}} \tag{30}$$

$$B_z(\mathbf{v}_A) = \mathbf{e}_z \cdot \mathbf{B}(\mathbf{v}_A) \tag{31}$$

$$= \frac{\mu_0}{4\pi} \int_0^{2\pi} I R_{\text{Loop}} \frac{\left[R_{\text{Loop}} - r_A \cos\varphi\right] d\varphi}{\left[r_A^2 + R_{\text{Loop}}^2 + (z_A - z_S)^2 - 2 r_A R_{\text{Loop}} \cos\varphi\right]^{\frac{3}{2}}} \tag{32}$$

Consider the loop is placed at $z_s = 0$ such that the coordinates z_A and r_A are replaced directly by z and r, respectively. Hence, the integrals in Eq. (30) and Eq. (32) yield [131]

$$B_r(r,z) = \frac{\mu_0 I}{2\pi r} \frac{z}{\sqrt{\left(R_{\text{Loop}} + r\right)^2 + z^2}} \left[-K(k) + \frac{R_{\text{Loop}}^2 + r^2 + z^2}{\left(R_{\text{Loop}} - r\right)^2 + z^2} E(k) \right] \quad (33)$$

$$B_z(r,z) = \frac{\mu_0 I}{2\pi} \frac{1}{\sqrt{\left(R_{\text{Loop}} + r\right)^2 + z^2}} \left[+K(k) + \frac{R_{\text{Loop}}^2 - r^2 - z^2}{\left(R_{\text{Loop}} - r\right)^2 + z^2} E(k) \right] \quad (34)$$

where $K(k)$ and $E(k)$ are the elliptic integrals of the first and second kinds, respectively, which are defined by

$$K(k) = \int_0^{\pi/2} \frac{1}{\sqrt{1 - k^2 \sin^2 \alpha}} d\alpha \quad (35)$$

$$E(k) = \int_0^{\pi/2} \sqrt{1 - k^2 \sin^2 \alpha}\, d\alpha \quad (36)$$

while k is given by

$$k^2 = \frac{4 r R_{\text{Loop}}}{\left(R_{\text{Loop}} + r\right)^2 + z^2} \quad (37)$$

The total magnetic field (norm) is defined by

$$B(r,z) = \sqrt{B_r^2(r,z) + B_z^2(r,z)} \quad (38)$$

Note that, volume integral should have been applied to Eq. (28). However, for simplicity, the loop is assumed to be of a negligible thickness, and only a line integral along its circumference is considered. Hence, this derivation and all other related derivations are *approximate* solutions used to estimate the magnetic fields of the corresponding sources.

3.2.3.3 Helmholtz Coil

Helmholtz coil is used to obtain a uniform magnetic field from two separated current loops or, more precisely, two thin coils [50] (see Fig. 15). A typical arrangement of a Helmholtz coil pair is shown in Fig. 15a. The coils are placed

parallel to each other with a separate distance equal to their identical radius $R_{\text{Helmholtz}}$. The superposition of the fields due to each separate coil gives the total magnetic field of Helmholtz coil, whose radial $B_r\,(r,z)$ and axial $B_z\,(r,z)$ components are respectively given by

$$B_r\,(r,z) = \frac{\mu_0 I}{2\pi r}\sum_{d_\text{h}} \frac{z-d_\text{h}}{\sqrt{\left(R_\text{Helmholtz}+r\right)^2+\left(z-d_\text{h}\right)^2}} \cdot\left[-K(k_{d_\text{h}}) + \frac{R_\text{Helmholtz}^2+r^2+\left(z-d_\text{h}\right)^2}{\left(R_\text{Helmholtz}-r\right)^2+\left(z-d_\text{h}\right)^2}E(k_{d_\text{h}})\right] \tag{39}$$

$$B_z\,(r,z) = \frac{\mu_0 I}{2\pi}\sum_{d_\text{h}} \frac{1}{\sqrt{\left(R_\text{Helmholtz}+r\right)^2+\left(z-d_\text{h}\right)^2}} \cdot\left[+K(k_{d_\text{h}}) + \frac{R_\text{Helmholtz}^2-r^2-\left(z-d_\text{h}\right)^2}{\left(R_\text{Helmholtz}-r\right)^2+\left(z-d_\text{h}\right)^2}E(k_{d_\text{h}})\right] \tag{40}$$

where

$$d_\text{h} \in \{-z_\text{h}, z_\text{h}\}, \qquad z_\text{h} = \frac{R_\text{Helmholtz}}{2} \tag{41}$$

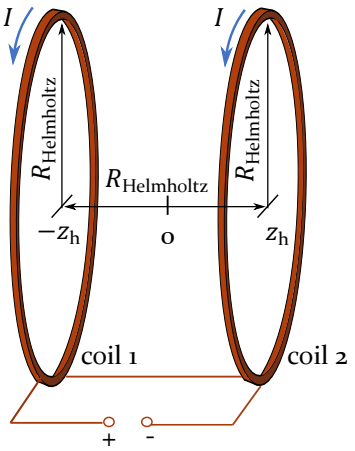

(a) Typical arrangement

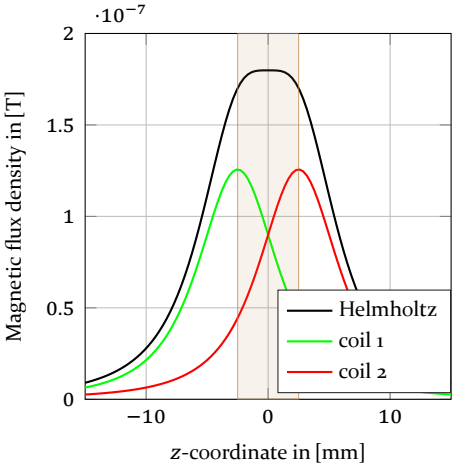

(b) Total magnetic field at $r = 0$ mm. Shaded area shows where the coil exists.

Figure 15: Helmholtz coil and its magnetic field for $R_{\text{Helmholtz}} = 5$ mm and $I = 1$ mA.

and

$$k_{d_\mathrm{h}}^2 = \frac{4rR_\mathrm{Helmholtz}}{\left(R_\mathrm{Helmholtz}+r\right)^2+\left(z+d_\mathrm{h}\right)^2} \tag{42}$$

The total magnetic field of the Helmholtz coil at $r = 0$ mm is shown in Fig. 15b. Its length $R_\mathrm{Helmholtz} = 5$ mm is chosen to be identical to the length of the employed susceptometer. The green and red curves show the magnetic fields produced by the two individual coils of Helmholtz. The black curve represents the total field, which is uniform along the center axis between the individual coils. However, the uniformity is lost and the field decays near the borders of the shaded area.

3.2.3.4 Maxwell Coil

Maxwell tried to improve the uniformity of the field obtained from Helmholtz coil by adding a third coil [94] (see Fig. 16). A typical arrangement of Maxwell coil is shown in Fig. 16a, which involves a large central coil of radius R_Maxwell carrying current I and two relatively small side coils each of radius $R_\mathrm{m} = \sqrt{\frac{4}{7}}R_\mathrm{Maxwell}$ carrying current $I_\mathrm{m} = \frac{49}{64}I$ placed on either side of the main coil at an axial distance $z_\mathrm{m} = \sqrt{\frac{3}{7}}R_\mathrm{Maxwell}$. The superposition of the fields due to the three coils gives the magnetic field of the Maxwell coil as follows

$$\begin{aligned} B_r\left(r,z\right) = {} & \frac{\mu_0 I_\mathrm{m}}{2\pi r}\sum_{d_\mathrm{m}} \\ & \frac{z-d_\mathrm{m}}{\sqrt{\left(R_\mathrm{m}+r\right)^2+\left(z-d_\mathrm{m}\right)^2}}\cdot\left[-K(k_{d_\mathrm{m}})+\frac{R_\mathrm{m}^2+r^2+\left(z-d_\mathrm{m}\right)^2}{\left(R_\mathrm{m}-r\right)^2+\left(z-d_\mathrm{m}\right)^2}E(k_{d_\mathrm{m}})\right] \\ & +\frac{\mu_0 I}{2\pi}\frac{z}{\sqrt{\left(R_\mathrm{Maxwell}+r\right)^2+z^2}}\cdot\left[-K(k)+\frac{R_\mathrm{Maxwell}^2+r^2+z^2}{\left(R_\mathrm{Maxwell}-r\right)^2+z^2}E(k)\right] \end{aligned} \tag{43}$$

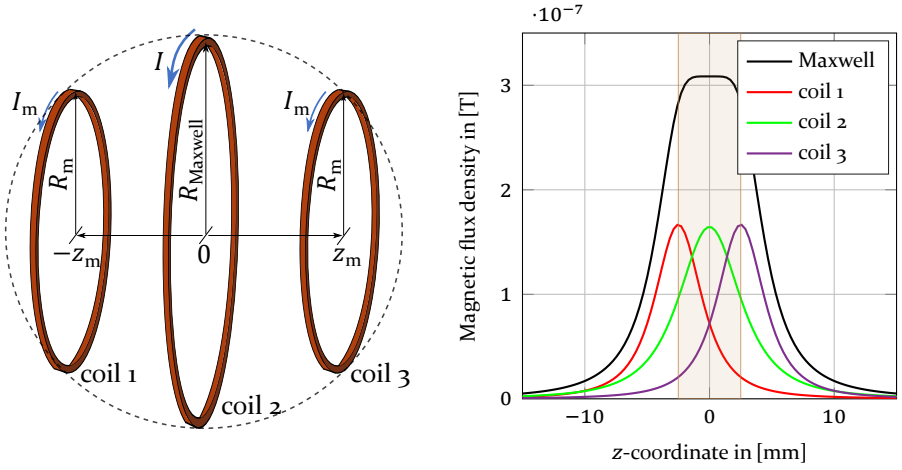

(a) Typical arrangement

(b) Total magnetic field at $r = 0$ mm. Shaded area shows where the coil exists.

Figure 16: Maxwell coil and its magnetic field for $R_{\text{Maxwell}} = \frac{5}{2}\sqrt{\frac{7}{3}}$ mm and $I = 1$ mA.

$$B_z(r,z) = \frac{\mu_0 I_m}{2\pi} \sum_{d_m} \frac{1}{\sqrt{(R_m + r)^2 + (z - d_m)^2}} \cdot \left[+K(k_{d_m}) + \frac{R_m^2 - r^2 - (z - d_m)^2}{(R_m - r)^2 + (z - d_m)^2} E(k_{d_m}) \right] + \frac{\mu_0 I}{2\pi} \frac{1}{\sqrt{(R_{\text{Maxwell}} + r)^2 + z^2}} \cdot \left[+K(k) + \frac{R_{\text{Maxwell}}^2 - r^2 - z^2}{(R_{\text{Maxwell}} - r)^2 + z^2} E(k) \right] \quad (44)$$

where

$$d_m \in \{-z_m, z_m\} \qquad \text{and} \qquad k_{d_m}^2 = \frac{4 r R_m}{(R_m + r)^2 + (z + d_m)^2} \quad (45)$$

The total magnetic field at $r = 0$ mm is shown in Fig. 16b. In order to make a fair comparison with the Helmholtz coil, the length is kept fixed, i.e., equal to 5 mm. For that reason, the main radius of Maxwell coil is chosen to be $R_{\text{Maxwell}} = \frac{5}{2}\sqrt{\frac{7}{3}}$ mm. The red, green, and purple curves show the magnetic fields produced by the individual coils, whereas the black curve is the total field from the three coils. As can be seen, along the center axis of the Maxwell coil, the field is nearly uniform and decays outside its ends. However, comparing

the fields from both Maxwell and Helmholtz coils shows that the decay in Maxwell is faster, which demonstrates the improvement introduced to it.

More detailed field analysis for both coils will be given later based on the numerical simulation.

3.2.3.5 Solenoids

A solenoid is a wire wrapped in the form of a helix of radius R_{Sol} and length L_{Sol} (see Fig. 17). Consider the wire is of a negligible thickness such that it forms a *thin* solenoid of N_l wire-turns. The number of turns in an infinitesimal length dz_S of the solenoid is $\left(\frac{N_l}{L_{\text{Sol}}}\right) dz_S$, which produces current

$$dI = I \cdot \left(\frac{N_l}{L_{\text{Sol}}}\right) dz_{\text{S}} \tag{46}$$

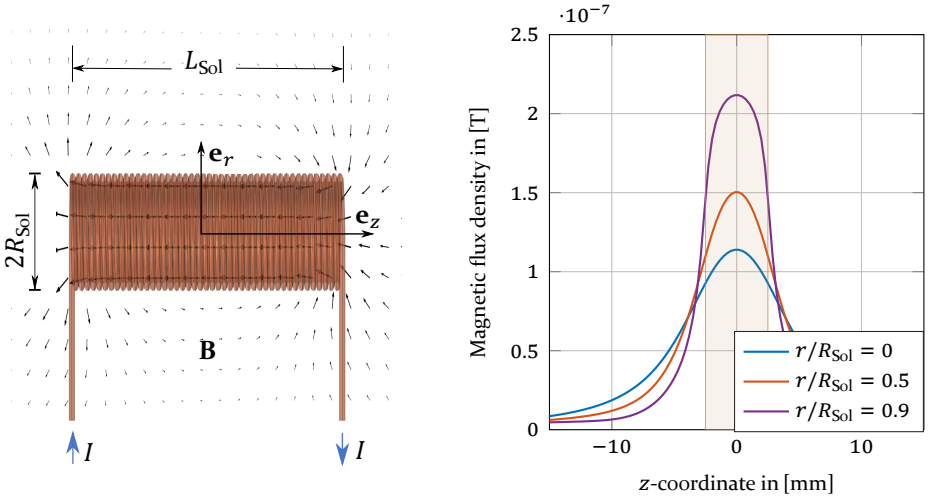

(a) A wire wounded tightly to form a solenoid. Black arrows represent its magnetic field.

(b) Magnetic field at different radial positions. Shaded area shows where the coil exists.

Figure 17: A thin solenoid and its magnetic field for $L_{\text{Sol}} = R_{\text{Sol}} = 5$ mm and $I = 1$ mA.

The magnetic field of this solenoid can be obtained when Eq. (28) is expanded to integrate over the solenoid length. After substituting Eq. (46) into Eq. (28), the total magnetic field is defined by

$$B\left(\mathbf{v}_A\right)=\frac{\mu_0}{4\pi}\frac{IN_lR_{\mathrm{Sol}}}{L_{\mathrm{Sol}}}\int_{-L_{\mathrm{Sol}}/2}^{L_{\mathrm{Sol}}/2}dz_S\int_0^{2\pi}\frac{\left[\mathbf{e}_{r_S}\left(z_A-z_S\right)+\mathbf{e}_z\left(R_{\mathrm{Sol}}-r_A\cos\varphi\right)\right]d\varphi}{\left[r_A^2+R_{\mathrm{Sol}}^2+\left(z_A-z_S\right)^2-2r_AR_{\mathrm{Sol}}\cos\varphi\right]^{\frac{3}{2}}} \tag{47}$$

Accordingly, both components of the magnetic field are obtained from Eq. (30) and Eq. (32), respectively, when the axial and radial coordinates (z_A, r_A) are replaced by (z, r)

$$B_r\left(r,z\right)=\frac{\mu_0}{4\pi}\frac{IN_lR_{\mathrm{Sol}}}{L_{\mathrm{Sol}}}\int_{-L_{\mathrm{Sol}}/2}^{L_{\mathrm{Sol}}/2}dz_S\int_0^{2\pi}\frac{\left[\left(z-z_S\right)\cos\varphi\right]d\varphi}{\left[r^2+R_{\mathrm{Sol}}^2+\left(z-z_S\right)^2-2r\,R_{\mathrm{Sol}}\cos\varphi\right]^{\frac{3}{2}}} \tag{48}$$

$$B_z\left(r,z\right)=\frac{\mu_0}{4\pi}\frac{IN_lR_{\mathrm{Sol}}}{L_{\mathrm{Sol}}}\int_{-L_{\mathrm{Sol}}/2}^{L_{\mathrm{Sol}}/2}dz_S\int_0^{2\pi}\frac{\left[R_{\mathrm{Sol}}-r\cos\varphi\right]d\varphi}{\left[r^2+R_{\mathrm{Sol}}^2+\left(z-z_S\right)^2-2r\,R_{\mathrm{Sol}}\cos\varphi\right]^{\frac{3}{2}}} \tag{49}$$

Elliptical integrals are used again to find the magnetic field of the thin solenoid as follows [81]

$$B_r\left(r,z\right)=-\frac{\mu_0}{\pi}\frac{IN_l}{L_{\mathrm{Sol}}}\sqrt{\frac{R_{\mathrm{Sol}}}{r}}$$
$$\cdot\left[\frac{1}{k_-}\left(\left(1-\frac{k_-^2}{2}\right)K(k_-)-E(k_-)\right)-\frac{1}{k_+}\left(\left(1-\frac{k_+^2}{2}\right)K(k_+)-E(k_+)\right)\right] \tag{50}$$

$$B_z(r,z)=\frac{\mu_0}{4\pi}\frac{IN_l}{L_{\mathrm{Sol}}\sqrt{rR_{\mathrm{Sol}}}}\cdot\left[\left(z+\frac{L_{\mathrm{Sol}}}{2}\right)k_+\left(\left(\frac{2R_{\mathrm{Sol}}}{R_{\mathrm{Sol}}+r}-1\right)\Pi(t,k_+)+K(k_+)\right)\right.$$
$$\left.-\left(z-\frac{L_{\mathrm{Sol}}}{2}\right)k_-\left(\left(\frac{2R_{\mathrm{Sol}}}{R_{\mathrm{Sol}}+r}-1\right)\Pi(t,k_-)+K(k_-)\right)\right] \tag{51}$$

where the elliptic integral $\Pi(n,k)$ of the third kind is defined by

$$\Pi(n,k)=\int_0^{\pi/2}\frac{1}{\left(1-n\sin^2\alpha\right)\sqrt{1-k^2\sin^2\alpha}}d\alpha \tag{52}$$

with the parameters

$$n = \frac{4rR_{\mathrm{Sol}}}{(R_{\mathrm{Sol}}+r)^2} \qquad \text{and} \qquad k_{\pm}^2 = \frac{4rR_{\mathrm{Sol}}}{(R_{\mathrm{Sol}}+r)^2 + \left(z \pm \frac{L_{\mathrm{Sol}}}{2}\right)^2} \tag{53}$$

A geometrical representation of an arbitrary solenoid with its magnetic field lines is depicted in Fig.17a. However, the total magnetic field of a thin solenoid, whose length equals to its radius, i.e., $L_{\mathrm{Sol}} = R_{\mathrm{Sol}} = 5$ mm, at different radial positions is shown in Fig. 17b. At the center ($z = 0$), the field is maximum and decays when deviating axially away from it. The decay is faster near the inner boundary of the solenoid than along its center axis, where the amplitude is also relatively low.

Now assume the solenoid has a thickness of ΔR due to N_t layers of windings, which is the real representation of the solenoid. To include this thickness into the derivation so that the exact analytical solution of the field is obtained, the segment vector defined by Eq. (27) should be modified

$$d\mathbf{l}_S = \mathbf{e}_{\varphi_S} r_S \, d\varphi_S \tag{54}$$

In addition, the infinitesimal length dz_S in Eq. (46) should be replaced by an infinitesimal area $dA_S = dz_S \, dr_S$ from the *thick* solenoid, which produces current

$$dI = I \cdot \left(\frac{N_l}{L_{\mathrm{Sol}}} \frac{N_t}{\Delta R}\right) dz_S \, dr_S \tag{55}$$

Therefore, a triple integral over dr_S, $d\varphi$ and dz_S is needed to obtain the total magnetic field

$$\begin{aligned} \mathbf{B}(\mathbf{v}_A) &= \frac{\mu_0}{4\pi} \frac{I}{L_{\mathrm{Sol}}} \frac{N}{\Delta R} \\ &\cdot \int_{-L_{\mathrm{Sol}}/2}^{L_{\mathrm{Sol}}/2} dz_S \int_{R_{\mathrm{Sol}}}^{R_2} r_S \, dr_S \int_0^{2\pi} \frac{\mathbf{e}_{r_S}(z_A - z_S) + \mathbf{e}_z [r_S - r_A \cos\varphi]}{\left[r_A^2 + r_S^2 + (z_A - z_S)^2 - 2 r_A r_S \cos\varphi\right]^{\frac{3}{2}}} d\varphi \end{aligned} \tag{56}$$

where

$$R_2 = R_{\mathrm{Sol}} + \Delta R \qquad \text{and} \qquad N = N_l \, N_t \tag{57}$$

This integral is challenging to be analytically solved. Therefore, for thick solenoids, numerical solutions (simulations) are usually employed, which are given in Chapter 5. Nevertheless, approximated field components of any thick

solenoid can be obtained with acceptable accuracy from graphs and equations introduced in [24].

The magnetic field along the center axis of the thick solenoid is obtained from

$$\mathbf{B}(r_A = 0, z) = \frac{\mu_0}{4\pi} \frac{IN}{L_{\mathrm{Sol}} \Delta R} \int_{-L_{\mathrm{Sol}}/2}^{L_{\mathrm{Sol}}/2} dz_S \int_{R_{\mathrm{Sol}}}^{R_2} dr_S \, r_S \int_0^{2\pi} \frac{\mathbf{e}_{r_S}(z - z_S) + \mathbf{e}_z \, r_S}{[{r_S}^2 + (z - z_S)^2]^{\frac{3}{2}}} d\varphi \tag{58}$$

$$= \frac{\mu_0}{2} \frac{IN}{L_{\mathrm{Sol}} \Delta R} \int_{-L_{\mathrm{Sol}}/2}^{L_{\mathrm{Sol}}/2} dz_S \int_{R_{\mathrm{Sol}}}^{R_2} r_S \frac{\mathbf{e}_{r_S}(z - z_S) + \mathbf{e}_z \, r_S}{[{r_S}^2 + (z - z_S)^2]^{\frac{3}{2}}} dr_S \tag{59}$$

from which the axial component is given by [74]

$$B_z(r_A = 0, z) = \frac{\mu_0}{2} \frac{IN}{L_{\mathrm{Sol}} \Delta R} \int_{-L_{\mathrm{Sol}}/2}^{L_{\mathrm{Sol}}/2} dz_S \int_{R_{\mathrm{Sol}}}^{R_2} dr_S \frac{{r_S}^2}{[{r_S}^2 + (z - z_S)^2]^{\frac{3}{2}}} \tag{60}$$

$$= \frac{IN\mu_0}{2L_{\mathrm{Sol}}} \cdot \left\{ \frac{\frac{L_{\mathrm{Sol}}}{2} - z}{R_2 - R_{\mathrm{Sol}}} \cdot \ln\left(\frac{R_2 + \sqrt{R_2^2 + \left(\frac{L_{\mathrm{Sol}}}{2} - z\right)^2}}{R_{\mathrm{Sol}} + \sqrt{R_{\mathrm{Sol}}^2 + \left(\frac{L_{\mathrm{Sol}}}{2} - z\right)^2}} \right) \right. \tag{61}$$

$$\left. + \frac{\frac{L_{\mathrm{Sol}}}{2} + z}{R_2 - R_{\mathrm{Sol}}} \cdot \ln\left(\frac{R_2 + \sqrt{R_2^2 + \left(\frac{L_{\mathrm{Sol}}}{2} + z\right)^2}}{R_{\mathrm{Sol}} + \sqrt{R_{\mathrm{Sol}}^2 + \left(\frac{L_{\mathrm{Sol}}}{2} + z\right)^2}} \right) \right\} \tag{62}$$

$$= \frac{IN\mu_0}{2L_{\mathrm{Sol}}} \cdot w_{\mathrm{B}}(z) \tag{63}$$

where $w_{\mathrm{B}}(z)$ is defined by

$$w_{\mathrm{B}}(z) = \frac{\frac{L_{\mathrm{Sol}}}{2} - z}{R_2 - R_{\mathrm{Sol}}} \cdot \ln\left(\frac{R_2 + \sqrt{R_2^2 + \left(\frac{L_{\mathrm{Sol}}}{2} - z\right)^2}}{R_{\mathrm{Sol}} + \sqrt{R_{\mathrm{Sol}}^2 + \left(\frac{L_{\mathrm{Sol}}}{2} - z\right)^2}} \right)$$

$$+ \frac{\frac{L_{\mathrm{Sol}}}{2} + z}{R_2 - R_{\mathrm{Sol}}} \cdot \ln\left(\frac{R_2 + \sqrt{R_2^2 + \left(\frac{L_{\mathrm{Sol}}}{2} + z\right)^2}}{R_{\mathrm{Sol}} + \sqrt{R_{\mathrm{Sol}}^2 + \left(\frac{L_{\mathrm{Sol}}}{2} + z\right)^2}} \right) \tag{64}$$

This equation will be used later to analytically estimate the system response due to the particle propagation through the susceptometer.

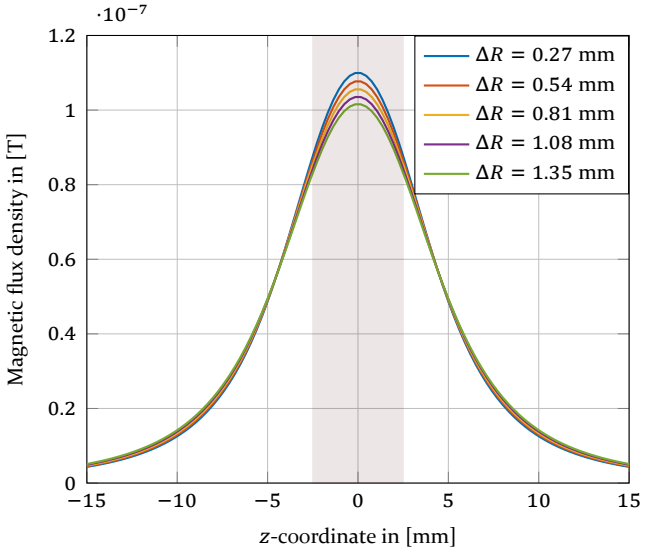

Figure 18: Axial component of the magnetic field of a thick solenoid along its center-axis at different thicknesses. Shaded area shows where the coil exists.

To demonstrate how the thickness of the solenoid affects its magnetic field, the magnetic field along the center axis of the thick solenoid at different thicknesses, $\Delta R \in \{0.27, 0.54, ..., 1.35\}$ mm, is depicted in Fig. 18.

Increasing the thickness of the solenoid reduces its magnetic field and slightly slows down the decay outside its ends. This behavior negatively affects the system response, as will be seen later.

3.2.3.6 Planar Coils

All previously mentioned coils are cylindrical coils wrapped around the tube. However, consider a scenario where the detector is embedded in a smart device and placed directly on the skin. Planar coils (Fig. 19), including circular and rectangular spirals, are well suited in such a case.

Circular planar coil is a flat spiral coil of N wire-turns and main radius R_N (see Fig. 19a). Its magnetic field can be approximated by the superposition of the magnetic fields due to N circular loops placed horizontally on the xy-plane and symmetrically about the z-axis. Each loop is of radius R_i, where the index $i \in \{1, 2, ..., N\}$ refers to the loop number. From Eq. (33) and Eq. (34), the

radial and axial field components of a circular spiral coil are approximated respectively by

$$B_r(r,z) = \frac{\mu_0 I}{2\pi r}\sum_{i=1}^{N}\frac{z}{\sqrt{(R_i+r)^2+z^2}}\left[-K(k)+\frac{{R_i}^2+r^2+z^2}{(R_i-r)^2+z^2}E(k)\right] \quad (65)$$

$$B_z(r,z) = \frac{\mu_0 I}{2\pi}\sum_{i=1}^{N}\frac{1}{\sqrt{(R_i+r)^2+z^2}}\left[+K(k)+\frac{{R_i}^2-r^2-z^2}{(R_i-r)^2+z^2}E(k)\right] \quad (66)$$

The similar concept can be applied to a *rectangular* planar coil of N wire-turns, length $2a_\mathrm{R}$ and width $2b_\mathrm{R}$, shown in Fig. 19b. Its magnetic field is the superposition of the magnetic fields due to N rectangular current loops. The x-, y- and z-components of the magnetic field due to a single rectangular current loop are derived in [100] and given respectively by

$$B_x(x,y,z) = \frac{\mu_0 I}{4\pi}\sum_{l_\mathrm{R}=1}^{4}(-1)^{l_\mathrm{R}}\,X_{l_\mathrm{R}}z \quad (67)$$

$$B_y(x,y,z) = \frac{\mu_0 I}{4\pi}\sum_{l_\mathrm{R}=1}^{4}(-1)\,Y_{l_\mathrm{R}}z \quad (68)$$

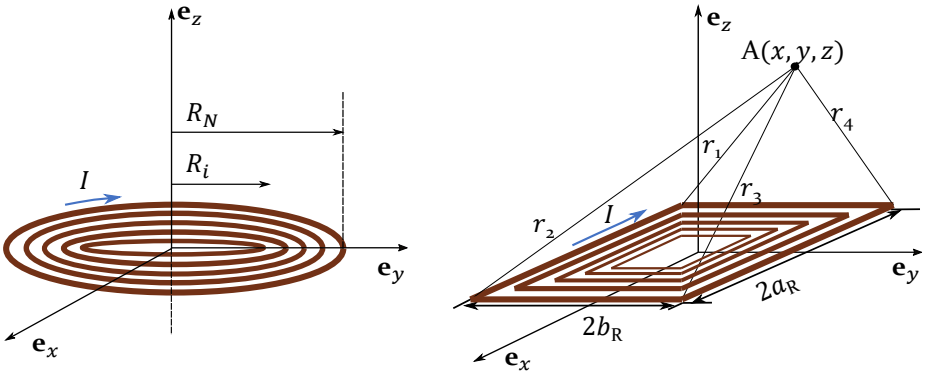

(a) Circular (b) Rectangular

Figure 19: Superposition of N current loops that compose two different spiral planar coils.

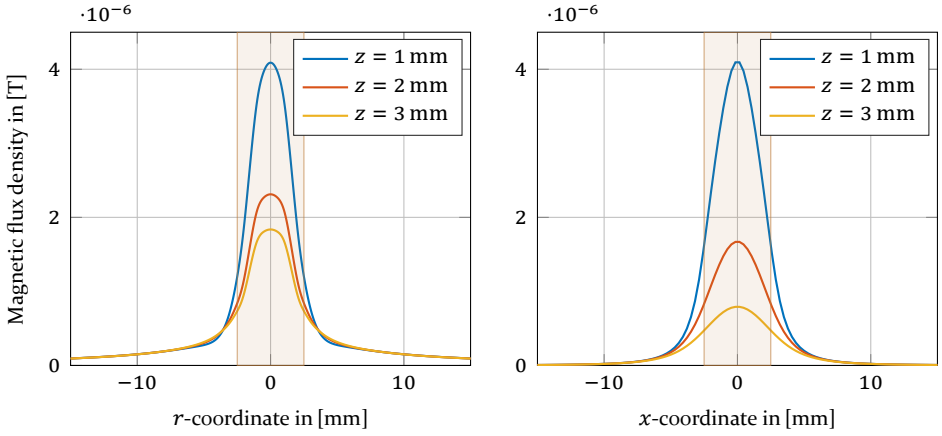

(a) Circular (b) Square

Figure 20: Magnetic field at different axial positions above two different spiral planar coils for $2R_N = 2a_R = 2b_R = 5\,\text{mm}$ and $N = 15$ wire-turns. Shaded area shows where the coils exist.

$$B_z(x,y,z) = \frac{\mu_0 I}{4\pi} \sum_{l_R=1}^{4} \left[X_{l_R} C_{l_R} + Y_{l_R} D_{l_R} \right] \tag{69}$$

where

$$X_{l_R} = \frac{(-1)}{r_{l_R}\left[r_{l_R} + D_{l_R}\right]} \tag{70}$$

$$Y_{l_R} = \frac{(-1)^{l_R}}{r_{l_R}\left[r_{l_R} + (-1)^{l_R+1} C_{l_R}\right]} \tag{71}$$

$$C_1 = -C_4 = a_R + x, \qquad D_1 = D_2 = y + b_R$$
$$C_2 = -C_3 = a_R - x, \qquad D_3 = D_4 = y - b_R$$

with r_1, r_2, r_3, and r_4 are distances from the field point A(x,y,z) to the individual vertices of a single rectangle

$$r_1 = \sqrt{(a_R + x)^2 + (y + b_R)^2 + z^2}, \quad r_2 = \sqrt{(a_R - x)^2 + (y + b_R)^2 + z^2}$$
$$r_3 = \sqrt{(a_R - x)^2 + (y - b_R)^2 + z^2} \quad r_4 = \sqrt{(a_R + x)^2 + (y - b_R)^2 + z^2}$$

Consider that the length and width of the rectangular coil are equal, such that a square planar coil is obtained. The propagation tube is laid down

directly above the center of the spiral coils. Hence, the diameter and length of the circular and square coils can be considered their detection lengths, respectively. Fig. 20 shows the magnetic field along different horizontal lines above the two spiral coils for a fixed detection length of 5 mm and $N = 15$ wire-turns.

In both coils, the field is symmetric about the z- axis. Most of the field is confined to the region where the coils exist. However, the decay of the fields is very prominent when moving vertically away from their surfaces, i.e., double distance reduces the field almost by half. This property limits the coverage region of the detector. However, it reduces the interference due to any magnetic materials that might exist nearby.

4 Analysis of Fluid Dynamics and Particle Detection

4.1 Simplified SPIONs-based Testbed

In this section, to reduce the computational complexity of the 3D simulation, the SPIONs-based testbed shown in Fig. 8b is simplified to a 2D-rotationally symmetric model. An analytical solution to this naive model is given to estimate the propagation profile of the SPIONs inside the channel. Besides, the essential time durations during the particle transmission are derived.

4.1.1 Mathematical Description

In the simplified model, the Y-connector is removed, while the injected particle suspension is assumed to fully mix with the background flow within the transmitter, as shown in Fig. 21a. The transmitter releases an injected volume V_{Inj} of SPIONs suspension at an injection flow rate of $Q_{\mathrm{Inj},0}$ into the propagation channel that has a stationary flow rate Q_{BG} of water. The time-dependent injection flow rate $Q_{\mathrm{Inj}}(t)$ is described by

$$Q_{\mathrm{Inj}}(t) = Q_{\mathrm{Inj},0} \cdot H(t) \tag{72}$$

where $H(t)$ is a unit step function defined by

$$H(t) = \begin{cases} 1, & \text{if } t \leq T_{\mathrm{Inj}} \\ 0, & \text{otherwise} \end{cases} \tag{73}$$

T_{Inj} is the time duration of the particle injection into the channel. It is calculated from

$$T_{\mathrm{Inj}} = \frac{V_{\mathrm{Inj}}}{Q_{\mathrm{Inj},0}} \tag{74}$$

The channel flow rate $Q_{\mathrm{Ch}}(t)$ is the summation of both background and injection flow rates

$$Q_{\mathrm{Ch}}(t) = Q_{\mathrm{Inj}}(t) + Q_{\mathrm{BG}} \tag{75}$$

The average propagation velocity of the water flow is related to the channel flow rate through

$$u_{\mathrm{avg}} = \frac{Q_{\mathrm{Ch}}}{\pi R_{\mathrm{Ch}}^2} \tag{76}$$

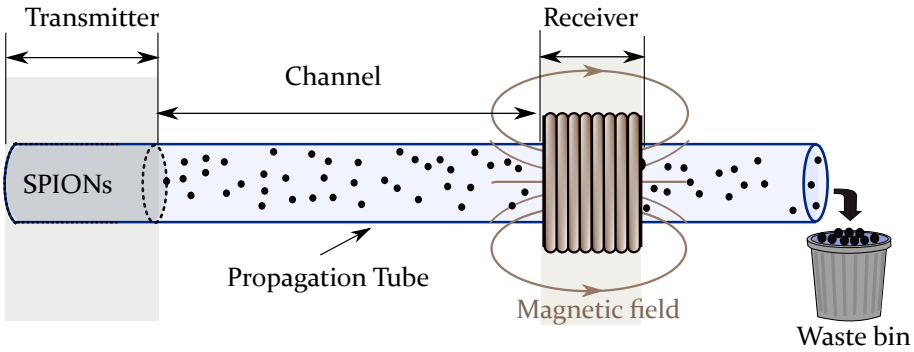

(a) Simplified geometry.

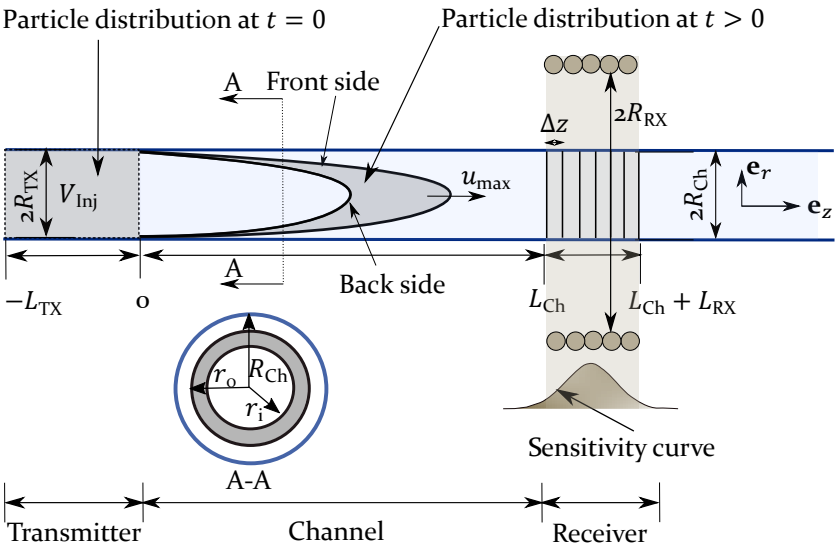

(b) Theoretical representation.

Figure 21: A 2D-axisymmertic naive model of the SPIONs-based testbed shown in Fig. 8b.

At the receiver side, the SPIONs are detected using an MS2G Bartington® susceptometer of length $L_{Susc} = 5\,mm$ and radius $R_{Susc} = 5\,mm$, whose inductance changes when the particles pass through its core and disturb its magnetic field.

The minimum and maximum values of the injection flow rates in this testbed are 1.4 mL/min and 5.26 mL/min, respectively. The corresponding values for the background flow rates are 5.0 mL/min and 20 mL/min, respectively. Also, the smallest and largest radii of the standard tubes used in the lab are 0.61 mm

Table 1: Extreme channel parameters considered in the testbed.

Flow rate	$Q_{\text{Inj},0}$ [mL/min]	Q_{BG} [mL/min]	Q_{Ch} [mL/min]	Tube size	R_{Ch} [mm]	u_{avg} [mm/s]	$u_{\text{avg}} \cdot 2R_{\text{Ch}}$ [mm²/s]
Min.	1.40	5.0	6.40	Min.	0.61	91.24	111.31
				Max.	1.585	13.51	42.83
Max.	5.26	20	25.26	Min.	0.61	360.14	439.37
				Max.	1.585	53.34	169.09

and 1.585 mm, respectively. Table 1 illustrates the different flow velocities in the channel when the extreme parameters are applied, which are used below to derive the characteristics of the propagating flow.

To describe the propagating flow in the testbed, the different characteristic numbers defined in section 3.1.4 are determined when the extreme parameters given in Table 1 are applied.

The largest Knudsen number Kn is given by

$$\text{Kn} = \frac{0.31\,\text{nm}}{2 \cdot 0.61\,\text{mm}} = 2.541 \cdot 10^{-7} \tag{77}$$

which ensures that Eq. (2) can be solved using a no-slip boundary condition. In addition, the largest Reynolds number Re is determined by

$$\text{Re} = \frac{439.37\,\text{mm}^2/\text{s}}{1.01 \cdot 10^{-6}\,\text{m}^2/\text{s}} = 435.02 < 2300 \tag{78}$$

that ensures laminar flow in the propagation tube.

The maximum channel length of the SPIONs-based testbed is assumed to be 100 mm. Therefore, the length of the propagation tube divided by its diameter is

$$\frac{L_{\text{Ch}}}{2R_{\text{Ch}}} = \frac{100\,\text{mm}}{2 \cdot 0.61\,\text{mm}} = 81.96 \tag{79}$$

while the minimum Péclet number is given by

$$\text{Pe} = \frac{42.83\,\text{mm}^2/\text{s}}{10^{-11}\,\text{m}^2/\text{s}} = 42.83 \cdot 10^5 \gg 81.96 \tag{80}$$

This value guarantees that the diffusion is negligible in the testbed.

4.1.2 Analytical Derivation of the SPIONs Propagation Profile

The testbed can be described theoretically as shown in Fig. 21b. Assume the particles have an initial volume density ρ_0 inside the transmitter, whose length and radius are L_{TX} and R_{TX}, respectively. As derived above, the diffusion in this model can be neglected, and the flow is considered laminar with a parabolic velocity profile described by

$$u(r,t) = u_{\max}(t) \cdot \left(1 - \left(\frac{r}{R_{\mathrm{Ch}}}\right)^2\right) \tag{81}$$

From Eq. (74) and Eq. (76), the length of the transmitter is defined by

$$L_{\mathrm{TX}} = u_{\mathrm{avg}} \cdot T_{\mathrm{Inj}} = \frac{V_{\mathrm{Inj}}}{\pi R_{\mathrm{Ch}}^2} \cdot \left(\frac{Q_{\mathrm{BG}}}{Q_{\mathrm{Inj},0}} + 1\right) \tag{82}$$

The radial coordinate $r(z,t)$, as a function of the axial position z and time t, is derived from the velocity $u(r,t)$ as follows

$$u(r,t) = \frac{dz}{dt} \tag{83}$$

$$z = \int_0^t u(r,t)dt + z_0 \tag{84}$$

$$= \int_0^{T_{\mathrm{Inj}}} u(r,t)dt + \int_{T_{\mathrm{Inj}}}^t u(r,t)dt + z_0 \tag{85}$$

Using Eq. (72), Eq. (73), Eq. (75) and Eq. (81), $r(z,t)$ is described by

$$r(z,t) = R_{\mathrm{Ch}} \sqrt{1 - \frac{z - z_0}{z_{\max}(t)}} \tag{86}$$

where $z_{\max}(t)$ is defined by

$$z_{\max}(t) = \frac{2}{\pi R_{\mathrm{Ch}}^2} \cdot \begin{cases} \left(Q_{\mathrm{Inj},0} + Q_{\mathrm{BG}}\right) t & \text{if } t \le T_{\mathrm{Inj}} \\ Q_{\mathrm{Inj},0} T_{\mathrm{Inj}} + Q_{\mathrm{BG}} t & \text{otherwise} \end{cases} \tag{87}$$

From Eq. (86) and Eq. (87), the outer $r_{\mathrm{o}}(z,t)$ and inner $r_{\mathrm{i}}(z,t)$ radii of the parabolic velocity profile can be found when $z_0 = 0$ and $-L_{\mathrm{TX}}$, respectively

$$\begin{aligned} r_{\mathrm{o}}(z,t) &= R_{\mathrm{Ch}}\sqrt{1-\frac{z-0}{z_{\max}(t)}} \\ r_{\mathrm{i}}(z,t) &= R_{\mathrm{Ch}}\sqrt{1-\frac{z+L_{\mathrm{TX}}}{z_{\max}(t)}} \end{aligned} \tag{88}$$

During the propagation, the SPIONs are confined between those two radii, i.e., front and back sides shown in Fig. 21b. Due to the particle propagation and mixing with the background flow within the channel, their volume density changes to become

$$\rho_{\mathrm{Ch}} = \rho_0\left(\frac{V_{\mathrm{Inj}}}{\pi R_{\mathrm{Ch}}^2 L_{\mathrm{TX}}}\right) \overset{(82)}{=} \rho_0\left(\frac{Q_{\mathrm{Inj,o}}}{Q_{\mathrm{Inj,o}}+Q_{\mathrm{BG}}}\right) \tag{89}$$

Hence, the time-dependent number of particles within the receiver, whose length and radius are L_{RX} and R_{RX} respectively, can be obtained from

$$N_{\mathrm{Par.}}(t) = \rho_{\mathrm{Ch}} \cdot \int_{-L_{\mathrm{RX}}/2}^{L_{\mathrm{RX}}/2} \pi\left[r_{\mathrm{o}}(z,t)^2 - r_{\mathrm{i}}(z,t)^2\right] dz \tag{90}$$

4.1.3 Time Durations

To determine the time delay T_{D} between the transmitter and receiver, a new term called threshold time T_{Th} is defined, which is the time required by the particles to reach the receiver if they are carried by both background and injection flow rates

$$T_{\mathrm{Th}} = \frac{L_{\mathrm{Ch}}}{u_{\max}(T_{\mathrm{Inj}})} \overset{(72),(73),(75)}{=} \frac{L_{\mathrm{Ch}}\pi R_{\mathrm{Ch}}^2}{2(Q_{\mathrm{inj,o}}+Q_{\mathrm{BG}})} \tag{91}$$

Hence, the time delay is calculated from

$$T_{\mathrm{D}} = \begin{cases} T_{\mathrm{Inj}} + T_{\mathrm{BG}} & \text{if } T_{\mathrm{Inj}} < T_{\mathrm{Th}} \\ T_{\mathrm{Th}} & \text{otherwise} \end{cases} \tag{92}$$

where T_{BG} is the time taken, after the injection ends, by the particles that being carried only by the background flow rate to reach the receiver, and it is defined by

$$T_{\mathrm{BG}} = \frac{\pi R_{\mathrm{Ch}}^2 L_{\mathrm{Ch}} - 2T_{\mathrm{Inj}}(Q_{\mathrm{Inj,o}} + Q_{\mathrm{BG}})}{2Q_{\mathrm{BG}}} \tag{93}$$

The time delay is typically essential for the synchronization between the transmitter and receiver. After the particle transmission, the receiver waits for a time duration T_{D} until it starts to detect particles and decodes them into digital bits. Another critical time duration is T_{max}, which is the time from the start of the particle injection until reaching the peak maximum of the detected signal. These durations will be used later to compare the performance of the system response due to varied parameters.

4.2 Particle Distribution During Propagation

In order to ensure a uniform volume density of particles inside the transmitter before the injection, their distribution is assumed to be directly proportional to the radial coordinate r, such that the number of particles in a ring-cylinder near the boundary of the transmitter is higher than the number of particles at the center. However, this distribution changes during the propagation through the channel. In this section, a 2D particle density matrix, obtained from the simulation for a slice taken from the channel at a specific time instance after or during the particle injection, is used to estimate the radial and angular density vectors. Besides, the translation from the particle density into volume susceptibility is explained.

4.2.1 Channel Segmentation to Predict Particle Density

To investigate the particle distribution inside a slice of the channel, its cross-sectional area is subdivided into X radial and Y angular sections, i.e., small compartments, seen in Fig. 22. Assume an $[X \times Y]$ volume density matrix $\mathrm{P}_0(r, \varphi)$ of particles is obtained directly from the simulation at a specific time instance

$$\mathrm{P}_0(r, \varphi) = \mathrm{P}_r(r) \cdot \mathrm{P}_\varphi(\varphi) \tag{94}$$

where $\mathrm{P}_r(r)$ and $\mathrm{P}_\varphi(\varphi)$ are the exact (unknown) radial and angular particle density vectors, respectively. From $\mathrm{P}_0(r,\varphi)$, approximated vectors of $\mathrm{P}_r(r)$ and $\mathrm{P}_\varphi(\varphi)$ can be initially represented by

$$\tilde{\mathrm{P}}_r(r) = \frac{1}{Y}\sum_{j=1}^{Y} \mathrm{P}_0(r,j) \tag{95}$$

$$\tilde{\mathrm{P}}_\varphi(\varphi) = \frac{1}{X}\sum_{i=1}^{X} \mathrm{P}_0(i,\varphi) \tag{96}$$

The estimated particle density matrix $\nu(r,\varphi)$ is then defined by

$$\nu(r,\varphi) = c_0 \cdot \tilde{\mathrm{P}}_r(r) \cdot \tilde{\mathrm{P}}_\varphi(\varphi) \tag{97}$$

where c_0 is a constant to be optimized. The Mean Square Error (MSE) e_P between the exact and estimated volume density matrices is calculated from

$$\begin{aligned} e_\mathrm{P}^2 &= \frac{1}{XY}\sum_{i=1}^{X}\sum_{j=1}^{Y}\left(\mathrm{P}_0(i,j) - \nu(r,\varphi)\right)^2 \\ &\overset{(97)}{=} \frac{1}{XY}\sum_{i=1}^{X}\sum_{j=1}^{Y}\left(\mathrm{P}_0(i,j) - c_0 \cdot \tilde{\mathrm{P}}_r(i)\,\tilde{\mathrm{P}}_\varphi(j)\right)^2 \end{aligned} \tag{98}$$

To find the optimized value of c_0 from Eq. (98)

$$\begin{aligned} \frac{\partial e_\mathrm{P}^2}{\partial c_0} &\overset{!}{=} 0 \\ 2\sum_{i=1}^{X}\sum_{j=1}^{Y}\left(\mathrm{P}_0(i,j) - c_0 \cdot \tilde{\mathrm{P}}_r(i)\,\tilde{\mathrm{P}}_\varphi(j)\right)\cdot\left(-\tilde{\mathrm{P}}_r(i)\,\tilde{\mathrm{P}}_\varphi(j)\right) &\overset{!}{=} 0 \end{aligned} \tag{99}$$

from which c_0 is defined by

$$c_0 = \frac{\sum_{i=1}^{X}\sum_{j=1}^{Y}\mathrm{P}_0(i,j)\,\tilde{\mathrm{P}}_r(i)\,\tilde{\mathrm{P}}_\varphi(j)}{\sum_{i=1}^{X}\sum_{j=1}^{Y}\tilde{\mathrm{P}}_r^2(i)\,\tilde{\mathrm{P}}_\varphi^2(j)} \tag{100}$$

Redefine the estimated density matrix $\nu(r,\varphi)$ as follows

$$\begin{aligned} \nu(r,\varphi) &= \left(\sqrt{c_0}\cdot\tilde{\mathrm{P}}_r(r)\right)\cdot\left(\sqrt{c_0}\cdot\tilde{\mathrm{P}}_\varphi(\varphi)\right) \\ &= R(r)\cdot A(\varphi) \end{aligned} \tag{101}$$

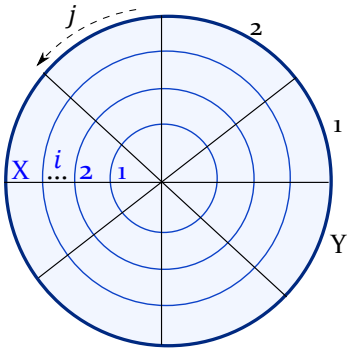

Figure 22: Subdivision of the channel cross-sectional area into $[X \times Y]$ small compartments.

where $R(r)$ and $A(\varphi)$ are the estimated radial and angular density vectors, respectively.

4.2.2 Particle Density to Volume Susceptibility

Before the injection, the initial volume density of particles inside the transmitter in the simulation and measurement are ρ_0^{Sim} and ρ_0^{Meas} Particles/µL, respectively. While the initial volume susceptibility of particles in the measurement is $\chi_{\text{m}}^{\text{Meas}}$. Due to the propagation within the channel, the particle distribution and hence the volume density $\rho_{\text{Ch}}^{\text{Sim}}(i,j)$ and susceptibility $\chi_{\text{m}}^{\text{Sim}}(i,j)$ in each ij-indexed compartment, shown in Fig. 22, change with time according to

$$\chi_{\text{m}}^{\text{Sim}}(i,j,t) = \frac{\chi_{\text{m}}^{\text{Meas}}}{\rho_0^{\text{Sim}}} \cdot \rho_{\text{Ch}}^{\text{Sim}}(i,j,t) \tag{102}$$

The direct proportionality between the volume susceptibility and particle density is explained in the next section.

4.3 General Concept of Detection

When magnetic materials, e.g., SPIONs suspension, disturb the field of a coil, its inductance changes accordingly. In this section, the detection scheme of all detecting coils is defined. In addition, the time-dependent relative inductance due to the particle propagation through the air-core of a solenoid is analytically derived.

4.3.1 Detection Scheme of All Coils

Generally, the system response $s(t)$ is calculated from

$$s(t) = \frac{L(t) - L_{\text{ref}}}{L_{\text{ref}}} \tag{103}$$

where $L(t)$ is the time-dependent coil inductance and L_{ref} is a reference inductance (will be defined later). However, in the case of an air-cored coil, L_{ref} equals to the coil self-inductance L_0, and its corresponding system response $s_0(t)$ is defined by

$$s_0(t) = \frac{L(t) - L_0}{L_0} \tag{104}$$

Note that the terms detected signal, relative inductance, volume susceptibility, and system response are used interchangeably in this manuscript.

4.3.2 Detection Scheme of a Solenoid

4.3.2.1 Self-Inductance

Ampère's circuital law is used to estimate the self-inductance of a solenoid [127]

$$\oint_{c_s} \mathbf{B}_0 \cdot d\mathbf{l}_s = \mu_0 NI \tag{105}$$

$$\int_{l_1} \mathbf{B}_0 \cdot d\mathbf{l}_s + \int_{l_2} \mathbf{B}_0 \cdot d\mathbf{l}_s + \underbrace{\int_{l_3} \mathbf{B}_0 \cdot d\mathbf{l}_s}_{\approx 0} + \int_{l_4} \mathbf{B}_0 \cdot d\mathbf{l}_s = \mu_0 NI \tag{106}$$

$$\frac{1}{c_{\text{L}}} B_0 \, L_{\text{Sol}} = \mu_0 NI \tag{107}$$

Therefore, we get

$$B_0 = c_{\text{L}} \, \mu_0 \frac{NI}{L_{\text{Sol}}} \tag{108}$$

where $d\mathbf{l}_s$ is an infinitesimal element of the closed contour c_s that encloses all wire-turns of the solenoid, see Fig. 23. The contour has four sides of lengths l_1, l_2, l_3, and l_4. The main field of the solenoid is assumed to exist inside its inner core along l_1, while the field along l_3 is neglected. However, the influence of the weak fields along the other two sides is taken through the use of an adjustment factor c_{L}.

For short solenoids, $L_{\text{Sol}} \leq 2R_{\text{Sol}}$, a prominent effect of non-homogeneous fields at both ends of the solenoid appears, therefore to include this effect,

the adjustment factor takes a value of $0.1 \leq c_{\mathrm{L}} < 1$ [49]. For long solenoids, $L_{\mathrm{Sol}} > 2R_{\mathrm{Sol}}$, the non-homogeneous fields can be neglected relative to the homogeneous field inside the coil, hence $c_{\mathrm{L}} \approx 1$.

The magnetic flux of the field lines that pass through the solenoid's cross-sectional area A_{Sol} is defined by

$$\Phi_{\mathbf{B}} = \iint_{A_{\mathrm{Sol}}} \mathbf{B} \cdot d\mathbf{A} \tag{109}$$

where $d\mathbf{A}$ is a vector area whose direction is perpendicular to A_{Sol}. Assuming a homogeneous field, the magnetic flux density will be approximated by

$$\Phi_{\mathrm{B}_0} = \iint_{A_{\mathrm{Sol}}} \mathbf{B}_0 \cdot d\mathbf{A} = B_0 \, A_{\mathrm{Sol}} \tag{110}$$

which is used together with Eq. (108) to estimate the self-inductance of the solenoid [49]

$$L_0 = \frac{N \, \Phi_{B_0}}{I} = \frac{N \, B_0 \, A_{\mathrm{Sol}}}{I} = c_{\mathrm{L}} \, \mu_0 \, \frac{N^2 \, A_{\mathrm{Sol}}}{L_{\mathrm{Sol}}} \tag{111}$$

4.3.2.2 Relative Inductance Derivation

In order to analytically derive the change of the solenoid inductance due to the presence of the magnetic materials in its air core, assume its length is subdivided into Z slices (see Fig. 23), each of width ΔZ_l and has ΔN_l windings, where $l \in \{1, 2, ..., Z\}$ is the slice number indicator. During the particle propagation, the inductance can be calculated from

$$L = \frac{\Phi_{\mathbf{B}}}{I} = \frac{1}{I} \sum_{l=1}^{z} \sum_{k_l=1}^{\Delta N_l} \phi_{\mathbf{B}}(l, k_l) \tag{112}$$

where $k_l \in \{1, 2, ..., \Delta N_l\}$ is an indicator to the wire-turn number in each slice l, which results in a magnetic flux density $\phi_{\mathbf{B}}(l, k_l)$. However, by assuming uniformly distributed wire-turns, the magnetic flux can be approximated

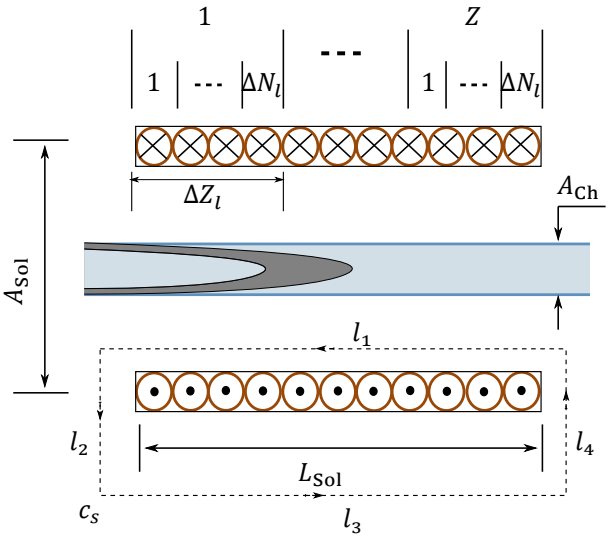

Figure 23: A closed contour c_s, which has four sides of lengths l_1, l_2, l_3, and l_4, is taken around all wire-turns of the solenoid. Also, the solenoid is subdivided into Z slices, each is of length ΔZ_l and has ΔN_l wire-turns. The propagation tube with the propagating particles is placed along the center-axis of the solenoid.

to be only due to each slice times the number of windings it contains, i.e. $\phi_{\mathbf{B}}(l, k_l) \approx \phi_{\mathbf{B}}(l)$

$$L = \frac{1}{I} \sum_{l=1}^{Z} \phi_{\mathbf{B}}(l) \cdot \sum_{k_l=1}^{\Delta N_l} 1 \tag{113}$$

$$= \frac{1}{I} \sum_{l=1}^{Z} \phi_{\mathbf{B}}(l) \cdot \Delta N_l \tag{114}$$

$$= \frac{1}{I} \sum_{l=1}^{Z} \phi_{\mathbf{B}}(l) \cdot \frac{\Delta N_l}{\Delta Z_l} \cdot \Delta Z_l \tag{115}$$

$$= \frac{1}{I} \sum_{l=1}^{Z} \phi_{\mathbf{B}}(l) \cdot n_z(l) \cdot \Delta Z_l \tag{116}$$

where $n_z(l) = \frac{\Delta N_l}{\Delta Z_l}$ is the linear density of the wire-turns.

For infinitesimally short slices, the summation operator in Eq. (116) can be replaced by an integral

$$L \overset{(116)}{=} \frac{1}{I} \int_{-L_{\mathrm{Sol}}/2}^{L_{\mathrm{Sol}}/2} n_z(z)\, \phi_{\mathbf{B}}(z)\, dz \tag{117}$$

$$\overset{(109)}{=} \frac{1}{I} \int_{-L_{\mathrm{Sol}}/2}^{L_{\mathrm{Sol}}/2} n_z(z) \cdot \left[\iint_{A_{\mathrm{Sol}}} \mathbf{B} \cdot d\mathbf{A} \right] dz \tag{118}$$

$$\overset{(20)}{=} \frac{1}{I} \int_{-L_{\mathrm{Sol}}/2}^{L_{\mathrm{Sol}}/2} n_z(z) \cdot \left[\iint_{A_{\mathrm{Sol}}} \mu \mathbf{H} \cdot d\mathbf{A} \right] dz \tag{119}$$

$$\overset{(20)}{=} \frac{1}{I} \int_{-L_{\mathrm{Sol}}/2}^{L_{\mathrm{Sol}}/2} n_z(z) \cdot \left[\iint_{A_{\mathrm{Sol}}} \mu_0 \mathbf{H} \cdot d\mathbf{A} + \iint_{A_{\mathrm{Sol}}} \mu_0 \chi_{\mathrm{m}} \mathbf{H} \cdot d\mathbf{A} \right] dz \tag{120}$$

$$\overset{(21)}{=} \frac{1}{I} \int_{-L_{\mathrm{Sol}}/2}^{L_{\mathrm{Sol}}/2} n_z(z) \cdot \left[\iint_{A_{\mathrm{Sol}}} \mathbf{B}_0 \cdot d\mathbf{A} + \iint_{A_{\mathrm{Sol}}} \mu_0 \chi_{\mathrm{m}} \mathbf{H} \cdot d\mathbf{A} \right] dz \tag{121}$$

$$\overset{(110)}{=} \frac{N\, \Phi_{B_0}}{I} + \frac{\mu_0}{I} \int_{-L_{\mathrm{Sol}}/2}^{L_{\mathrm{Sol}}/2} n_z(z) \cdot \left[\iint_{A_{\mathrm{Sol}}} \chi_{\mathrm{m}}\, \mathbf{H} \cdot d\mathbf{A} \right] dz \tag{122}$$

$$\overset{(111)}{=} L_0 + \frac{\mu_0}{I} \int_{-L_{\mathrm{Sol}}/2}^{L_{\mathrm{Sol}}/2} n_z(z) \cdot \left[\iint_{A_{\mathrm{Sol}}} \chi_{\mathrm{m}}\, \mathbf{H} \cdot d\mathbf{A} \right] dz \tag{123}$$

This area integral can be subdivided into two regions, namely inside the propagation tube whose cross-sectional area is A_{Ch}, i.e., through which the SPIONs suspension propagates and contributes to the inductance change, and outside the tube where the medium is air, $\chi_{\mathrm{m}} = 0$, and hence its integral tends to zero. From this, Eq. (123) becomes

$$L = L_0 + \frac{\mu_0}{I} \int_{-L_{\mathrm{Sol}}/2}^{L_{\mathrm{Sol}}/2} n_z(z) \cdot \left[\iint_{A_{\mathrm{Sol}} - A_{\mathrm{Ch}}} \underbrace{\chi_{\mathrm{m}}}_{0}\, \mathbf{H} \cdot \mathrm{d}\mathbf{A} + \iint_{A_{\mathrm{Ch}}} \chi_{\mathrm{m}}\, \mathbf{H} \cdot \mathrm{d}\mathbf{A} \right] \mathrm{d}z \tag{124}$$

$$= L_0 + \frac{\mu_0}{I} \int_{-L_{\mathrm{Sol}}/2}^{L_{\mathrm{Sol}}/2} n_z(z) \cdot \left[\iint_{A_{\mathrm{Ch}}} \chi_{\mathrm{m}}\, \mathbf{H} \cdot \mathrm{d}\mathbf{A} \right] \mathrm{d}z \tag{125}$$

In order to relate the volume susceptibility of the SPIONs suspension to its iron concentration, an experiment was conducted in the lab, where a test tube was filled with SPIONS suspension of different concentrations and placed inside the detection unit of the employed susceptometer to measure the volume susceptibility of the suspension. Fig. 24 visualizes the relation between the iron concentration of the SPIONS and their measured volume

susceptibility. The results show that the magnetic volume susceptibility is linearly proportional to the iron concentration of the SPIONs suspension and hence the particle density [46]. H. Unterweger also approved this result in his doctoral thesis [137].

In case of particle propagation through the channel, the volume density becomes time- and space-dependent

$$\chi_{\mathrm{m}}(\mathbf{x}, t) \propto \rho_{\mathrm{v}}(\mathbf{x}, t) \tag{126}$$

$$= k_0 \, \rho_{\mathrm{v}}(\mathbf{x}, t) \tag{127}$$

where k_0 is a constant of proportionality and $\rho_{\mathrm{v}}(\mathbf{x}, t)$ is the number of particles per unit volume, i.e., volume particle density. By substituting Eq. (127) into Eq. (125), the time-dependent inductance is estimated by

$$L(t) = L_0 + \frac{k_0 \, \mu_0}{I} \int_{-L_{\mathrm{Sol}}/2}^{L_{\mathrm{Sol}}/2} n_z(z) \cdot \left[\iint_{A_{\mathrm{Ch}}} \rho_{\mathrm{v}}(\mathbf{x}, t) \, \mathbf{H} \cdot d\mathbf{A} \right] dz \tag{128}$$

Due to the dot product with the vector area, whose direction is perpendicular to the cross-sectional area of the solenoid, only the axial component $H_z(\mathbf{x})$ of the magnetic field contributes to the magnetic flux. By assuming a uniform linear

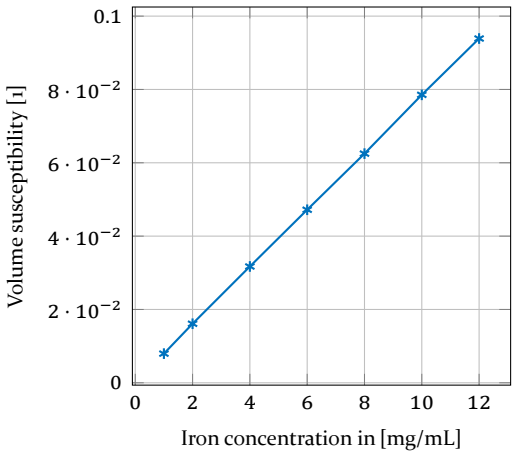

Figure 24: Relation between iron concentration of the SPIONs and their measured volume susceptibility.

density of windings, $n_z(z)$ can be replaced by $\frac{N}{L_{\mathrm{Sol}}}$. Hence, the inductance can be further described by

$$L(t) = L_0 + \frac{k_0\,\mu_0 N}{I L_{\mathrm{Sol}}} \int_{-L_{\mathrm{Sol}}/2}^{L_{\mathrm{Sol}}/2} \left[\iint_{A_{\mathrm{Ch}}} \rho_{\mathrm{v}}(\mathbf{x}, t)\, H_z(\mathbf{x})\, dA \right] dz \tag{129}$$

If Eq. (129) is compared with Eq. (104), the system response of the solenoid can be estimated analytically by

$$s_0(t) = \frac{k_0\,\mu_0 N}{I L_0 L_{\mathrm{Sol}}} \int_{-L_{\mathrm{Sol}}/2}^{L_{\mathrm{Sol}}/2} \left[\iint_{A_{\mathrm{Ch}}} \rho_{\mathrm{v}}(\mathbf{x}, t)\, H_z(\mathbf{x})\, dA \right] dz \tag{130}$$

This equation provides an efficient way to estimate the system response, where the Multiphysics simulation can be decoupled to two separate single domain simulations. One simulation is used to get the magnetic field distribution of the detector. The other simulation is used to get the particle density inside the detector during the propagation. Then, substitute in Eq. (130) to analytically estimate the system response.

If the field is uniformly distributed inside the propagation tube (no radial dependency), $H_z(\mathbf{x})$ in Eq. (130) can be replaced by $H_z(z)$

$$s_0(t) = \frac{k_0 \mu_0 N}{I L_0 L_{\mathrm{Sol}}} \int_{-L_{\mathrm{Sol}}/2}^{L_{\mathrm{Sol}}/2} \left[\iint_{A_{\mathrm{Ch}}} \rho_{\mathrm{v}}(\mathbf{x}, t)\, H_z(z)\, dA \right] dz \tag{131}$$

$$= \frac{k_0 \mu_0 N}{I L_0 L_{\mathrm{Sol}}} \int_{-L_{\mathrm{Sol}}/2}^{L_{\mathrm{Sol}}/2} H_z(z) \cdot \left[\iint_{A_{\mathrm{Ch}}} \rho_{\mathrm{v}}(\mathbf{x}, t)\, dA \right] dz \tag{132}$$

$$= k_{\mathrm{s}} \cdot \int_{-L_{\mathrm{Sol}}/2}^{L_{\mathrm{Sol}}/2} H_z(z)\, \rho_{\mathrm{l}}(z, t) dz \tag{133}$$

$$= \int_{-L_{\mathrm{Sol}}/2}^{L_{\mathrm{Sol}}/2} w(z)\, \rho_{\mathrm{l}}(z, t) dz \tag{134}$$

where $\rho_{\mathrm{l}}(z, t)$ is the number of particles per unit length inside the detector (linear particle density) and $w(z)$ is the sensitivity curve of the solenoid along its axial direction, and it is defined by

$$w(z) = k_{\mathrm{s}} \cdot H_z(z) \tag{135}$$

where k_{s} is a scaling parameter that will be defined later. As $H_z(z)$ can be analytically derived in case of a negligible radius dependency, only a single domain fluidic simulation is needed. The sensitivity curve is also called

the weighting function, which describes how the particles contribute to the generated signal based on their axial positions.

Note that Eq. (134) can be used to estimate the system response only in the region where the magnetic field is considered homogeneous, and the radial change is negligible. Otherwise, Eq. (130) should be used. However, both equations estimate the system response when assuming an ideal detector, i.e., the field is confined to the inner core of the solenoid, and only the particles that exist within its air core contribute to the detected signal.

5 Coils Simulation and Detection Mechanism

This chapter is subdivided into two main sections, namely cylindrical and planar coils. Each type is studied separately using the simulation, which is also used to analyze their corresponding magnetic fields and understanding their detection mechanism.

In order to reduce the computational complexity in this chapter, the SPIONs are assumed to be distributed in cylinders or ring cylinders that move in steps through or parallel to the employed coils. The particle suspension is assumed to have a volume susceptibility of $\chi_m = 0.0446$ for SPIONs or $\chi_m = 99$ for ferromagnetic particles. All coils are built using the Magnetic Fields submodule from the AC/DC module in COMSOL Multiphysics simulation software.

5.1 Cylindrical Coils

As stated in subsection 3.2.3.5, it is very challenging to analytically derive the exact magnetic field of a thick solenoid, which is also the basic unit for building other cylindrical coils such as Helmholtz and Maxwell (see Fig. 25). This section includes building FEM models of the employed coils and obtaining the system response due to the propagation of particles through their cores. Various distributions, positions, and trajectories of particles are applied to study their effect on the detected signal.

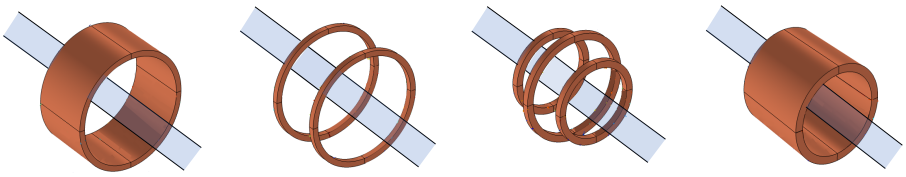

(a) Susceptometer, R_{Susc} (b) Helmholtz, R_{Susc} (c) Maxwell, R_m (d) Solenoid, R_m

Figure 25: Different geometries of the cylindrical coils with the propagation tube passes their cores.

5.1.1 Simulation Setup

A similar solenoid to that being used in the susceptometer, i.e., reference detector, is initially implemented (Fig. 25a). Then, Helmholtz coil that has the same radius is built and compared with it (Fig. 25b). To keep a fixed detection length of $L_{\text{Susc}} = 5\,\text{mm}$, the radius of the side coils of the Maxwell coil (Fig. 25c) has to be $R_{\text{m}} = \frac{R_{\text{Susc}}}{\sqrt{3}}$, and to make a fair comparison with it, another solenoid of the same radius R_{m} is built (Fig. 25d). All coils are made of copper and have the same thickness $\Delta R = 0.5\,\text{mm}$.

5.1.2 Magnetic Field Analysis

A detailed analysis of the magnetic field of the susceptometer in the radial and axial directions is shown in Fig. 26.

Moving radially from the center axis towards the inner boundary at different z-positions is indicated by colored arrows in Fig. 26a, and the corresponding values of the magnetic field strength $H(r, z)$ are shown in Fig. 26c. Inside the solenoid, a minor change in its magnetic field strength is noticed about the center axis, i.e., $r \leq 1\,\text{mm}$. In this region, the field can be considered homogeneous (uniformly distributed). However, when moving towards the inner boundary, the magnetic field increases in an exponential manner. This behavior is explained by Ampere's circuital law given by Eq. (105). The closed-loop of the magnetic field that contains the solenoid's wire-turns becomes relatively small for a field point near the inner boundary than about the center axis. Therefore, a relatively high magnetic field near the boundary is obtained if the current and permeability do not change. This effect is prominent in short solenoids, whose lengths are relatively shorter than their diameters. If a tube of radius $R_{\text{Ch}} < 1\,\text{mm}$ is placed axially along the center-axis of the susceptometer, where the field is considered homogeneous, any change in the radial positions of the particles will not significantly affect the detected signal and can be neglected.

On the other hand, the change of the solenoid's magnetic field strength along the z-axis at different radial positions (Fig. 26b) is shown in Fig. 26d. The axial magnetic field is symmetric about the center ($z = 0$), where the maximum is located and decreases on either side. As known from the radial analysis, for $r \leq 1\,\text{mm}$, the field is considered homogeneous. Therefore, the discrepancy between the first two curves, $r = 0$ and $1\,\text{mm}$, is not significant. However, for $r > 1\,\text{mm}$, the curves become narrower and tend to be flatter directly at the inner boundary. This behavior agrees with the results obtained in

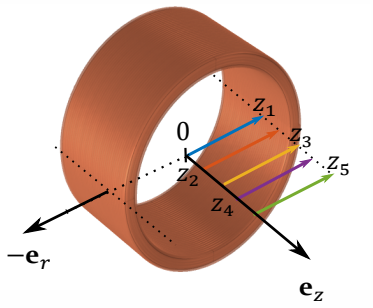

(a) Solenoid with radial vectors at different z-coordinates

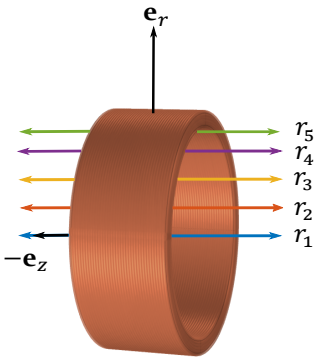

(b) Solenoid with axial vectors at different r-coordinates.

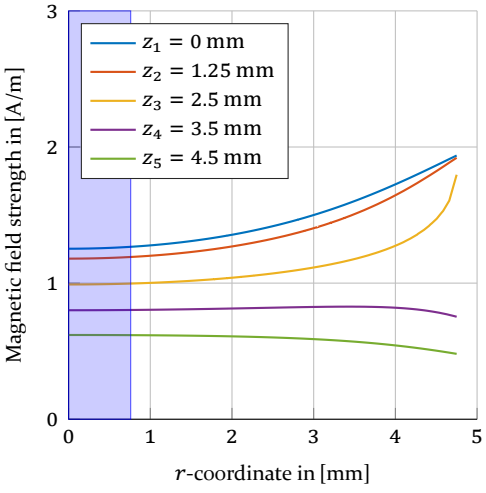

(c) Field strength in the radial direction. Blue shaded area shows where the propagation tube is placed.

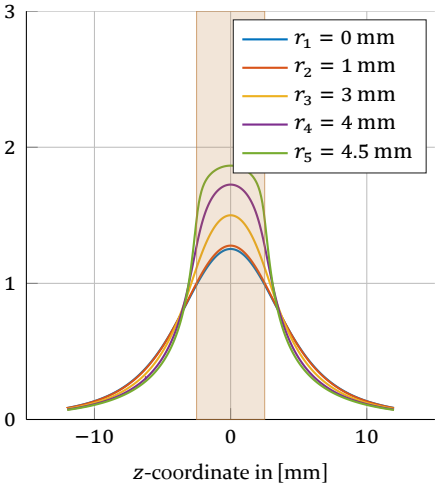

(d) Field strength in the axial direction. Brown shaded area shows where the coil exists.

Figure 26: Magnetic field of the simulated solenoid of the susceptometer.

subsection 3.2.3.5, where the magnetic field of the thin solenoid is analytically derived.

Fig. 27 shows the 3D- and 2D-view of the magnetic fields due to the different cylindrical coils for a detection length of $L_{\text{Susc}} = 5$ mm. As shown in Fig. 27a, the susceptometer is considered a short coil whose field is not entirely homogeneous, i.e., only about its center axis. Fig. 27b shows that the region of homogeneity increases in the Helmholtz coil at the expense of the amplitude, increasing the resilience to misalignment. However, the homogeneity is lost near the inner boundary, which is also noticed in Fig. 27c for the Maxwell coil. In order to improve the field uniformity, longer solenoids of small aspect ratio (diameter/length) can be used, as demonstrated in Fig. 27d.

A detailed comparison between the magnetic field strengths at two different radial positions is shown in Fig. 28. For a fixed length, when the radius of the coil is reduced, a relatively strong magnetic field strength is detected, which also decays faster outside the detection region. In addition, the obtained magnetic fields from the solenoids are, in general, relatively strong compared to their corresponding named coils. In Fig. 28a, as known, the fields due to the Helmholtz and Maxwell coils are almost uniform along their axes, while those from the solenoids look like a bell curve. These profiles mean that when the particles pass through a solenoid, those that exist at its center will significantly contribute to the detected signal than those exist at both ends. While in Helmholtz and Maxwell coils, all particles will contribute almost equally to the system response regardless of their axial positions within the detection region. However, when leaving the region of uniformity in the Helmholtz and Maxwell coils towards their inner boundaries, as shown in Fig. 28b, the field fluctuates and loses its homogeneity due to the contributions from their individual coils.

5.1.3 Different Studied Scenarios

In the following subsections, different scenarios are studied based on the susceptometer. In addition, the system responses due to the other cylindrical coils are obtained and compared with it. In all scenarios, the detected signal is calculated from Eq. (103) except that the inductance here is a space- not a time-dependent variable with L_{ref} defined separately in each scenario. Some of these studies were already published in [4].

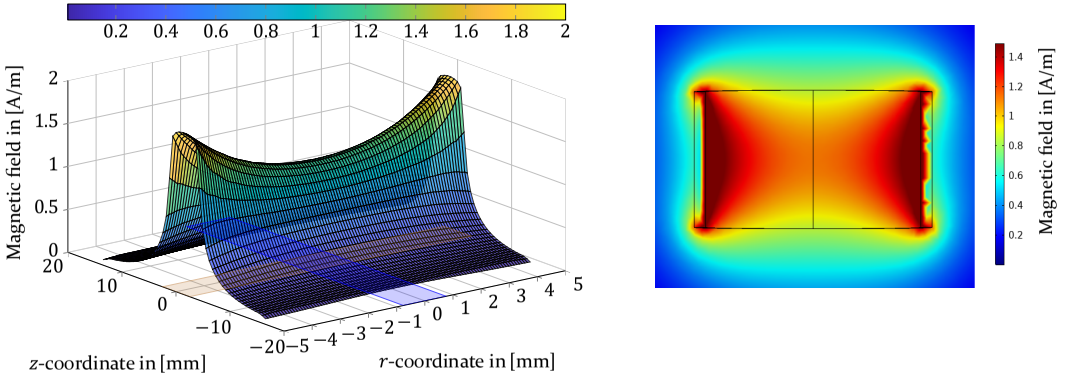

(a) Susceptometer, R_{Susc}

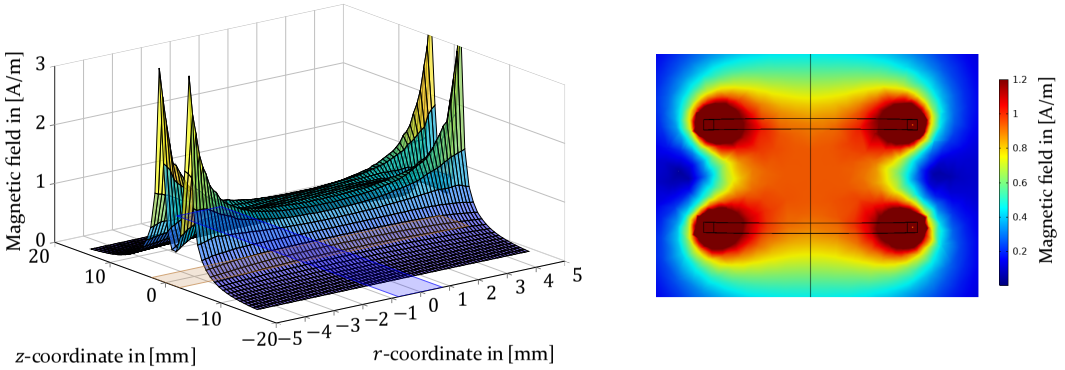

(b) Helmholtz coil, R_{Susc}

Figure 27: 3D-view (left) and 2D-view (right) of the magnetic field in [A/m] due to the different cylindrical coils for a detection length of $L_{\text{Susc}} = R_{\text{Susc}} = 5$ mm. Shaded blue and brown colors show where the propagation tube and coil exist, respectively.

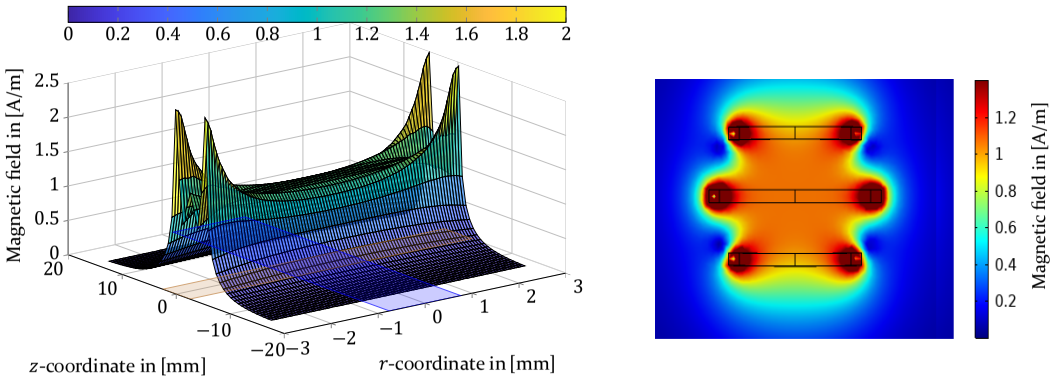

(c) Maxwell coil, $R_{\mathrm{m}} = \frac{R_{\mathrm{Susc}}}{\sqrt{3}}$

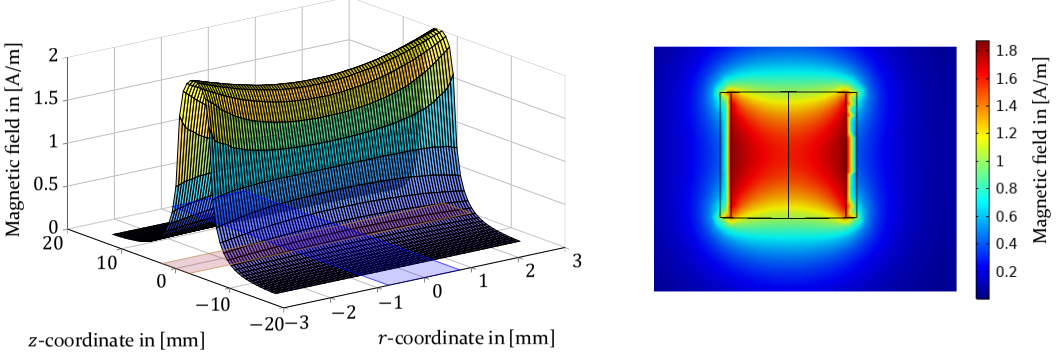

(d) Solenoid of the same radius as Maxwell, R_{m}

Figure 27: 3D-view (left) and 2D-view (right) of the magnetic field in [A/m] due to the different cylindrical coils for a detection length of $L_{\mathrm{Susc}} = R_{\mathrm{Susc}} = 5$ mm. Shaded blue and brown colors show where the propagation tube and coil exist, respectively (cont.).

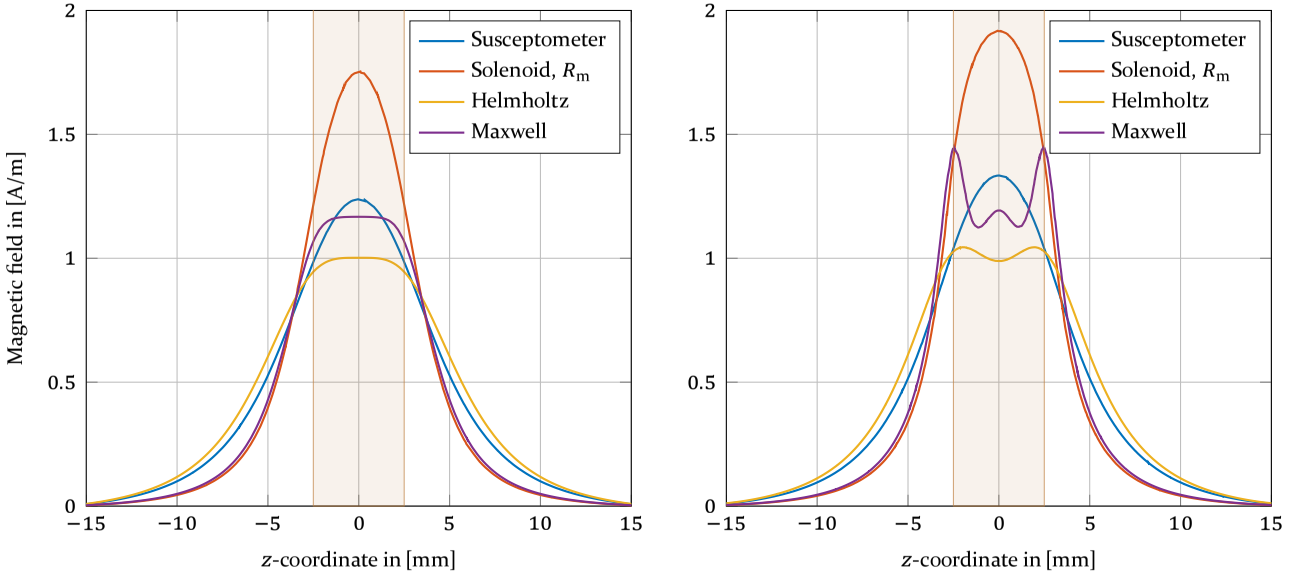

(a) $r = 0$ mm

(b) $r = 2$ mm

Figure 28: Magnetic field strength due to the cylindrical coils at two different radial positions for a fixed detection length of $L_{\text{Susc}} = R_{\text{Susc}} = 5$ mm, and $R_m = \frac{R_{\text{Susc}}}{\sqrt{3}}$. Shaded area shows where the coils exist.

5.1.3.1 Change of Axial Position

In this subsection, changing the axial position of the particles inside the suseptometer is studied numerically and validated by experiments, as seen in Fig. 29. Heuristically, a test tube filled with a uniformly distributed SPIONs suspension is inserted into the susceptometer in steps of 1 mm. The tube has a length and diameter of 27 mm and 6 mm, respectively. In the FEM model, shown in Fig. 29a, a cylinder of the exact dimensions and magnetic properties is used. In the same step-wise manner, the cylinder is inserted axially into the solenoid, starting from 12 mm away from its center (reference setup) until it is pulled out.

A comparison between the detected signal from simulation and measurement is shown in Fig. 29b. The results show a good agreement between the simulation and measurement. Far from the coil, no magnetic field exists, and hence no signal is detected. When the cylinder is moved axially towards the solenoid, the detected signal slightly increases because the magnetic field is not confined to its air-core. However, the signal gradually increases when the tube enters the coil. The saturation occurs when the cylinder fills the coil-core, and its front end begins to move outward.

5.1.3.2 Change of Radial Position

Here, the effect of changing the radial position of the magnetic material inside the solenoid is studied, as seen in Fig. 30. A SPIONs-filled cylinder

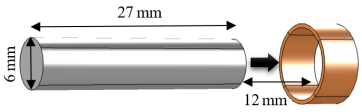

(a) SPIONs-filled cylinder is inserted in steps of 1 mm into the solenoid.

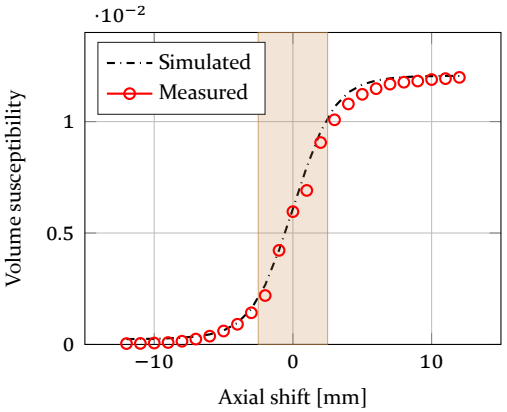

(b) Volume susceptibility obtained from simulation and measurement. Shaded area represents where the coil exists.

Figure 29: A study of the axial movement of a SPIONs-filled cylinder into the solenoid.

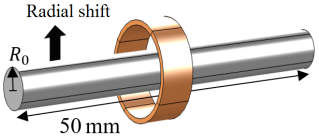

(a) SPIONs-filled long cylinder is moved radially inside the solenoid.

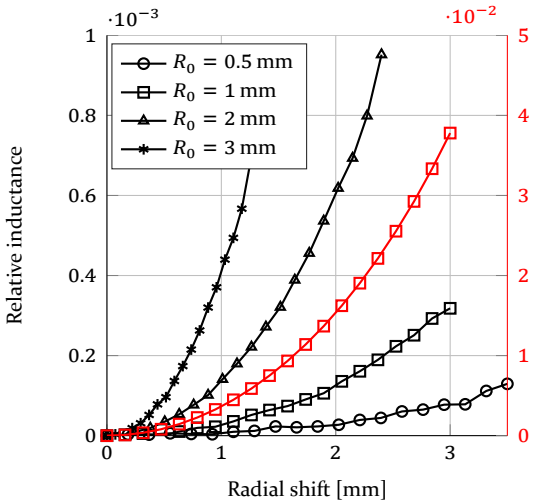

(b) Relative inductance. Black curves for $\chi_m = 0.0446$ and red curve for $\chi_m = 99$.

Figure 30: A study of the radial movement of a SPIONs-filled cylinder inside the solenoid.

of length 50 mm and variable radius $R_0 \in \{0.5, 1, 2, 3\}$ mm is placed axially along the center axis of the solenoid (reference setup) and moved towards its inner boundary (Fig. 30a), which imitates the radial movement of the tube (or particles) inside the susceptometer.

The detected signal is depicted in Fig. 30b. As expected, when the smallest cylinder, $R_0 = 0.5$ mm, is moved radially through the region where the magnetic field is considered homogeneous, a negligible change in the detected signal is observed. However, a slight increase is shown during its movement close to the inner boundary of the solenoid, where the magnetic field is relatively high. Also, when the cylinder radius slightly increases, $R_0 = 1$ mm, an inconsiderable change in the detected signal is observed unless it has a higher susceptibility, $\chi_m = 99$, which results in much higher relative inductance. For larger radii with the same particle density, the detected signal considerably increases. The increase seems to be directly proportional to the magnetic field strength of the solenoid in the radial direction.

5.1.3.3 Additive Behavior in Axial Direction

In this subsection, a study is conducted to test whether changes in inductance due to partial volumes are additive in the axial directions, see Fig. 31. First, a SPIONs-filled cylinder of a fixed diameter of 8 mm and a variable length

$l_n \in \{0.5, 1, ..., 25\}$ mm is placed 12 mm away from the coil center, such that any increase in its length is in the direction where the coil exists. The air-cored coil is assumed to be the reference setup, $L_{ref} = L_0$. For each length l_n, the coil inductance $L_{1:n}$ is obtained, which is also considered the inductance due to a concatenation of n discs each of thickness 0.5 mm, shown in Fig.31a. Second, a SPIONs-filled disc of the same diameter and initial position of the cylinder but a thickness of 0.5 mm is moved axially into the coil-core in steps of 0.5 mm until being pulled out. The inductance L_n of the coil due to different positions of the disc is recorded during the simulation.

In Fig. 31b, the relative inductance due to the discs concatenation (cylinder) is compared with the sum of the relative inductances due to the single disc at different axial positions. Before entering the solenoid, both curves agree well with each other; however, the discrepancy increases, and the curves mismatch when moving further into it. This gives a nonlinear behavior of inductance summation in the axial direction, which means that the inductance change caused by a SPIONs-filled cylinder is not equivalent to that caused by a summation of separate discs that form this cylinder.

5.1.3.4 Additive Behavior in Radial Direction

In this subsection, we test whether changes in inductance due to partial volumes are additive in the radial direction, see Fig. 32. First, a SPIONs-filled

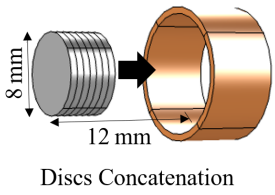

(a) A concatenation of SPIONs-filled discs are added up in steps inside the coil.

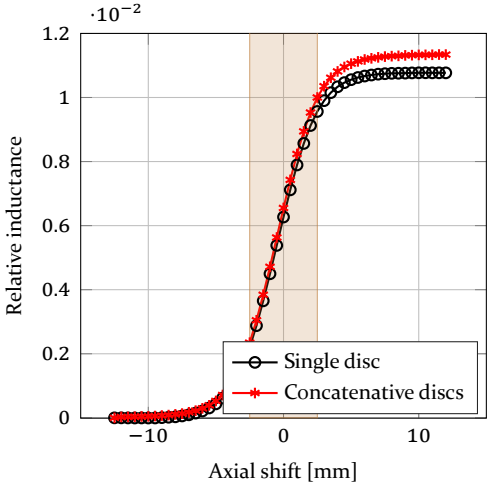

(b) Relative inductance due to the single-disc and discs concatenation.

Figure 31: Investigated scenario to test for axial additive behavior.

cylinder of length 25 mm and variable radius $R_k \in \{0.5, 1, ..., 4\}$ mm is placed axially along the center axis of the coil . The reference setup is considered when $R_k = 0.5$ mm. For each radius, the coil inductance $L_{1:k}$ is detected, which is also the inductance due to a concatenation of rings each of thickness 0.5 mm, seen in Fig. 32a. Second, a SPIONs-filled ring cylinder of the same length, fixed thickness of 0.5 mm and variable outer radius R_k is placed axially along the coil's center axis. For each ring cylinder, the coil inductance L_k is obtained.

In Fig.32b, the relative inductance due to the concatenation of rings (cylinder) is compared to the sum of the relative inductances due to the single ring-cylinder of each radius. Because the solenoid's magnetic field is rotationally symmetric, the change in inductance caused by a magnetic cylinder is equivalent to that caused by a summation of separate ring cylinders that form this cylinder, which gives a linear behavior of summation in the radial direction.

5.1.3.5 Concentric Increase of Particles

In this subsection, the effect of a concentric increase of particles inside the coil is studied, as shown in Fig. 33. A cylinder of uniformly distributed particles is placed axially along the center axis of the solenoid (reference setup). The cylinder has a fixed length of 50 mm, variable radius $R_{2,\,\mathrm{ref}} \in \{1.5, 2.5, 3.5\}$ mm and volume V_{ref}. The same particles are assumed to be distributed inside a

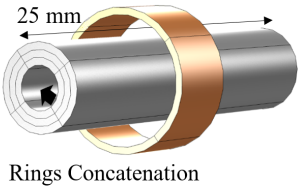

(a) A concatenation of SPIONs-filled ring cylinders are added up in steps inside the coil.

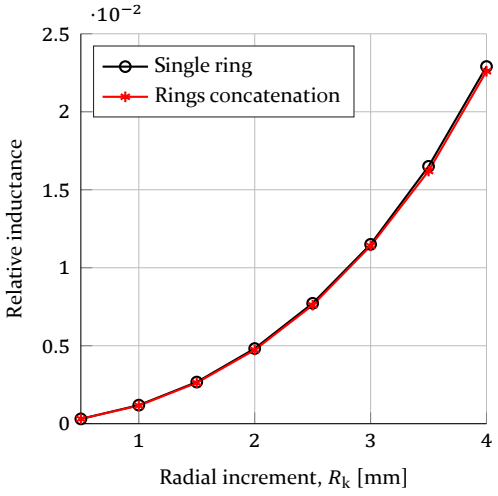

(b) Relative signal due to the single-ring cylinder and rings concatenation.

Figure 32: Investigated scenario to test for radial additive behavior.

ring cylinder (Fig. 33a) that has the same volume with variable inner and outer radii R_1 and R_2, respectively. Hence, the radii are related to the volume of the cylinder through

$$V_{\text{ref}} = 50\,\text{mm} \cdot \pi(R_2^2 - R_1^2) = 50\,\text{mm} \cdot \pi R_{2,\,\text{ref}}^2 \tag{136}$$

Therefore,

$$R_1 = \sqrt{R_2^2 - R_{2,\,\text{ref}}^2} \tag{137}$$

where the outer radius R_2 takes the values from $R_{2,\text{ref}}$ until R_{Susc}.

The results are demonstrated in Fig. 33b. When the particles are concentrated along the center axis of the coil, where the magnetic field is relatively low, a relatively weak signal is detected. On the contradict, when the same volume and density of particles are distributed near the inner boundary of the solenoid, its detected signal increases. As expected, the increase occurs in the same exponential manner of the magnetic field density in the radial direction. This result means that for a given volume and particle density, changing the position of particles inside the solenoid can significantly affect its detected signal. Also, the signal is directly proportional to the volume susceptibility of particles that exist in the detection region, e.g., increment by a factor of

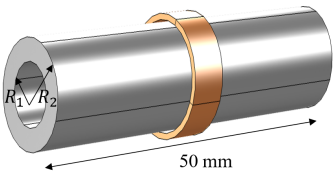

(a) SPIONs-filled ring cylinder of fixed volume and length but different radii.

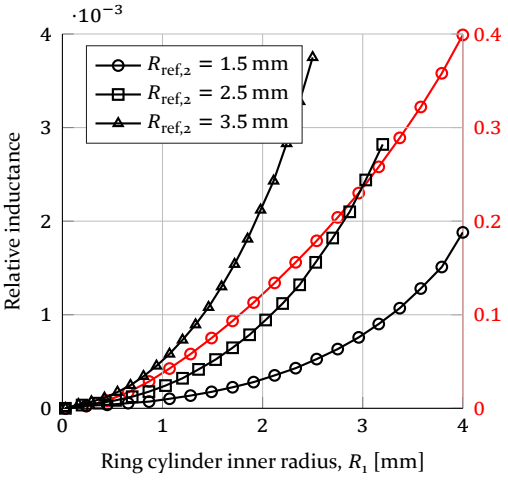

(b) Relative inductance. Black curves for $\chi_m = 0.0446$ and red curve for $\chi_m = 99$.

Figure 33: Investigated scenario to test for the effect of a concentric increase of particles inside the coil.

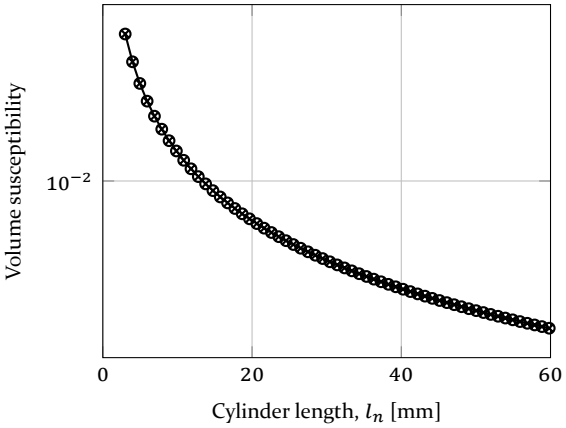

Figure 34: Volume susceptibility of the SPIONs-filled cylinder versus its length.

ca. 200 when the volume susceptibility increases from $\chi_{\mathrm{m}} = 0.0446$ to 99 at $R_1 = 4\,\mathrm{mm}$ and $R_{2,\,\mathrm{ref}} = 1.5\,\mathrm{mm}$.

In all previously mentioned scenarios, the particles are assumed to be contained within cylinders or ring cylinders that move inside the detector with no particle deformation over distance or time. In the following scenarios, including those for the planar coils, the SPIONs-filled cylinder is assumed to be of a fixed radius, a variable length, and fastened at a certain distance away from the detector. Its length increases in the direction where the detector exists. When the cylinder length increases, its volume increases accordingly, which reduces the particle density and hence the volume susceptibility, as shown in Fig. 34. This structure imitates the release of the particles into the propagation tube to be detected by the receiver. The air-cored solenoid is assumed to be the reference setup.

5.1.3.6 Different Propagation Trajectories Inside the Solenoid

In this subsection, the effect of changing the particle trajectory inside the solenoid is studied, see Fig. 35. The particles are distributed inside a cylinder of radius 1 mm and variable length $l_n \in \{2, 3, ..., 60\}$ mm fastened at a distance of 15 mm away from the solenoid center. Two different particle trajectories are considered, namely along the center axis of the solenoid and directly next to its inner boundary, as shown in Fig. 35a.

As illustrated in Fig. 35b, the system response obtained from the center trajectory is weaker and broader than that obtained from the boundary trajectory, where the field is relatively high and decays faster. The maximum value of

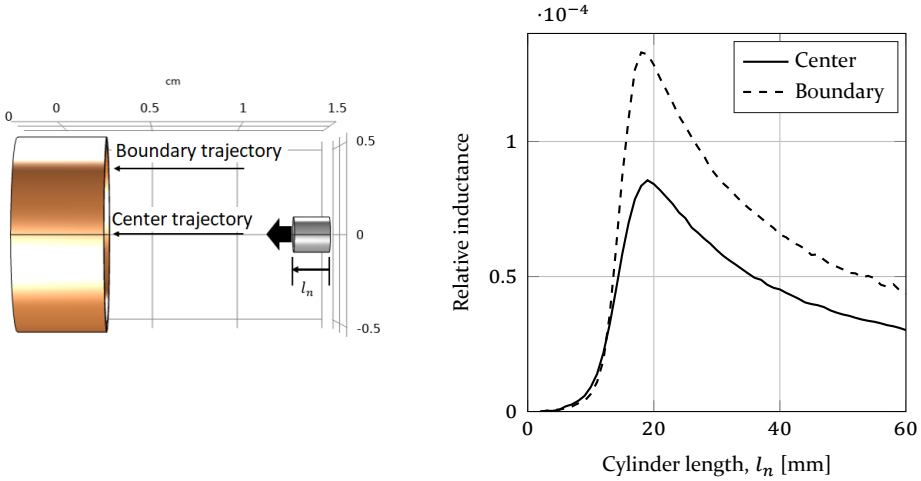

(a) Geometry description

(b) System response.

Figure 35: Particle propagation along two different trajectories inside the susceptometer.

the signal obtained from the boundary trajectory is approximately 1.5 times greater than that obtained from the center trajectory. Therefore, to avoid the discrepancy arising from misalignment problems, a homogeneous magnetic field is required. Otherwise, an adaptive threshold might be needed for decoding.

5.1.3.7 Comparision of System Responses by the Cylindrical Coils

In this subsection, only the central trajectory is considered to compare the system response (Fig. 36) due to the different cylindrical coils shown in Fig. 25. A cylinder of a variable length $l_n \in \{3, 4, ..., 50\}$ mm and a fixed radius of 2 mm is fastened 15 mm away from the center of the corresponding coil. As described before, increasing the length of the cylinder decreases its volume susceptibility.

The system responses from the susceptometer and Helmholtz coil are illustrated in Fig. 36a. Comparing the magnetic field profiles of both coils in Fig. 28 within the detection region explains the superiority of the susceptometer (solenoid) over the Helmholtz coil. Because the magnetic field strength of the susceptometer is relatively high, its corresponding detected signal is sharper. The same effect is also noticed in Fig. 36b when comparing the Maxwell coil with the solenoid of the corresponding radius. Again the solenoid shows better performance. The system response of each coil in both comparisons is directly proportional to the density of its magnetic field in the propagation path of

the particles. For instance, in Fig.28, the distance between the fields from the susceptometer and Helmholtz coil is relatively small, which is translated here into a relatively small difference between the system responses from both coils. In contrast to the larger distance between the magnetic fields of the small solenoid and Maxwell coil, which introduces a relatively large difference between their corresponding curves. This result is confirmed by the analytical solution derived in subsection 4.3.2.2, where the system response is estimated directly from the integral of the particle density weighted by the magnetic field strength within the detection region. As the particle density and volume susceptibility are similar in all four scenarios, only the magnetic field strength influences the detected signal.

5.1.3.8 Different Positions of the Solenoid

Here, changing the position of the susceptometer relative to the propagation tube is studied. The particles are assumed to be uniformly distributed inside a cylinder of radius 6 mm and variable length $l_n \in \{3, 4, ..., 60\}$ mm placed 20 mm away from the center of the coil in each corresponding position. The same solenoid and the same SPIONs-filled cylinder are employed in all positions. Different trajectories of the cylinder are considered, as shown in Fig. 37. In position 1 (Fig. 37a) and position 2 (Fig. 37b), the cylinder is placed outside the solenoid parallel and perpendicular to its center axis, respectively. The vertical distance between the cylinder and the outer surface of the solenoid is set to 2 mm. In position 3, the cylinder is placed axially along the center axis, as shown in Fig. 37c.

As depicted in Fig. 37d, in positions 1 and 2, the cylinder is placed outside the solenoid, where the field is relatively weak; hence, as expected, the detected signals are weaker than that obtained from position 3. However, the signal from position 2 is much stronger than that from position 1, where the field is negligible, as shown in the 2D-view of the magnetic field in Fig. 27a. Also, due to the large cross-sectional area of the solenoid relative to its length, the pulse obtained from position 2 is comparatively wide, and its peak maximum is slightly delayed; however, it is still detectable. Motivated by this scenario, planar coils are proposed so that no need to wrap the coil around the tube.

One should notice that the pulse obtained from position 2 is relatively strong and distinguishable because the susceptometer is considered a short coil of notable stray fields at its ends. However, if a long solenoid is employed, such as the one given in Fig. 25d, the detected signal will be comparatively weak.

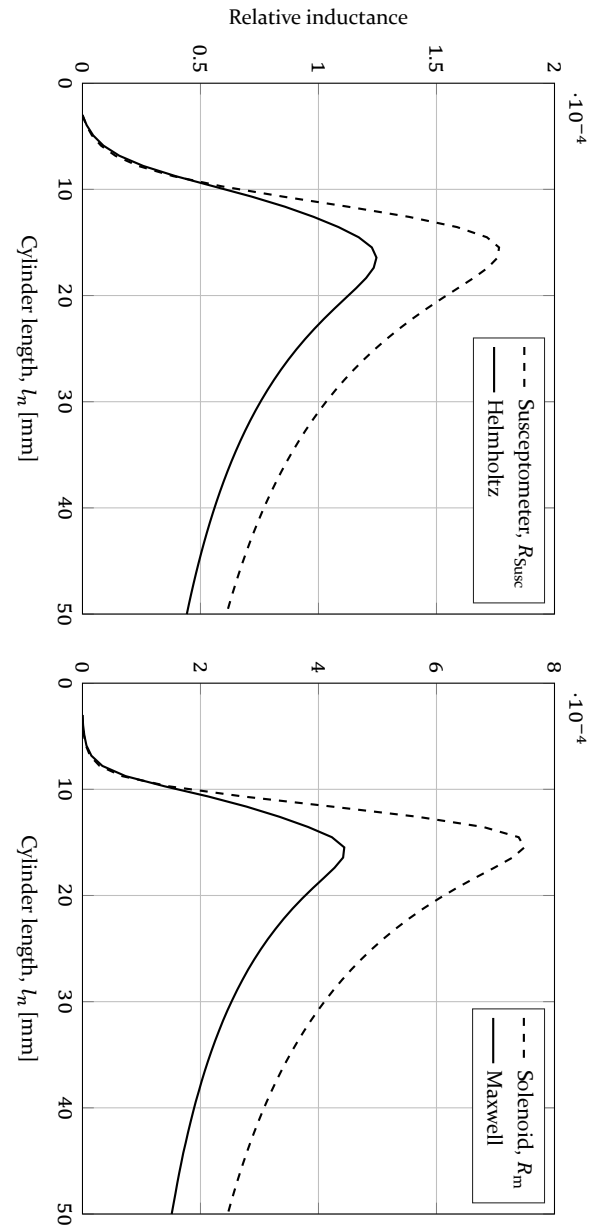

(a) Susceptometer (R_{Susc}) versus Helmholtz.

(b) Solenoid (R_m) versus Maxwell

Figure 36: System response due to the different cylindrical coils.

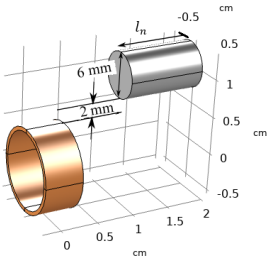

(a) Position 1: Axially parallel.

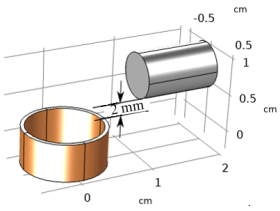

(b) Position 2: Perpendicular.

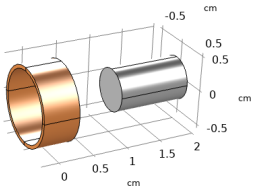

(c) Position 3: Along the axial.

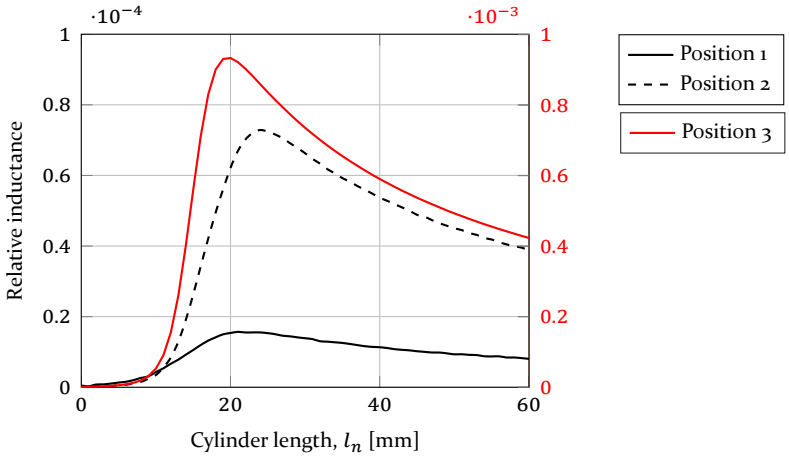

(d) System response.

Figure 37: Different positions of the SPIONs-filled cylinders to the solenoid and their corresponding system responses.

5.2 Planar Coils

Planar coils are applicable in regions where solenoids are difficult or inconvenient to be utilized. For instance, it is easier to embed a planar coil in a smart device and place it on the skin rather than wrapping a solenoid around the targeted vessel. Therefore, this section presents simulations of the different planar coils introduced in subsection 3.2.3.6. Also, in order to understand their detection behavior, the system responses due to the movement of the SPIONs-filled cylinders through their detection regions are obtained, compared and briefly analyzed.

5.2.1 Simulation Setup

As shown in Fig. 38, three different planar coils are built, namely square (Fig. 38a), circular (Fig. 38b), and rectangular (Fig. 38c). All coils are composed of 15 wire-turns with ≈ 0.1 mm wire thickness made of copper. The dimensions of the coils are chosen to be consistent with the employed susceptometer such that the length, diameter, and width of the square, circular and rectangular coils are identical and equal to the detection length $L_{\text{Susc}} = 5$ mm, respectively. The length of the rectangular coil is two times its width. However, two different geometries are considered for the circular coil, i.e., when the spiral starts directly at the origin (Fig. 38b) or when it starts at a specific distance about the origin, introducing a central aperture of radius 1.1 mm (Fig. 38d).

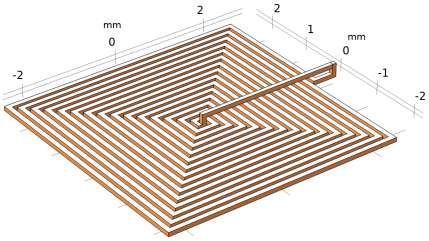

(a) Square

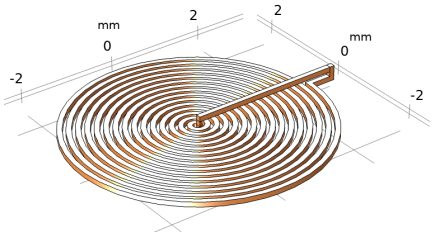

(b) Circular

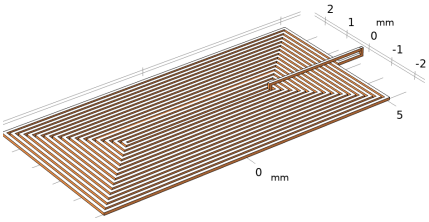

(c) Rectangle

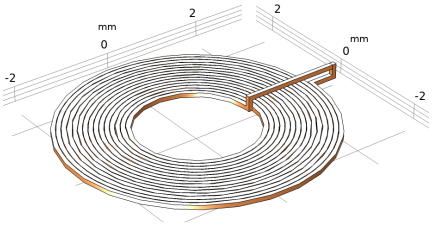

(d) Circular-aperture

Figure 38: Simulated planar coils made of copper, each of which has a wire thickness of 0.1 mm and 15 wire-turns.

5.2.2 Magnetic Field Analysis

In Fig. 39, a comparison between the magnetic fields of the first three coils at a vertical distance of 1 mm above their surfaces is given. In Fig. 40, the field is plotted at different z-positions to investigate how it decays in the vertical direction.

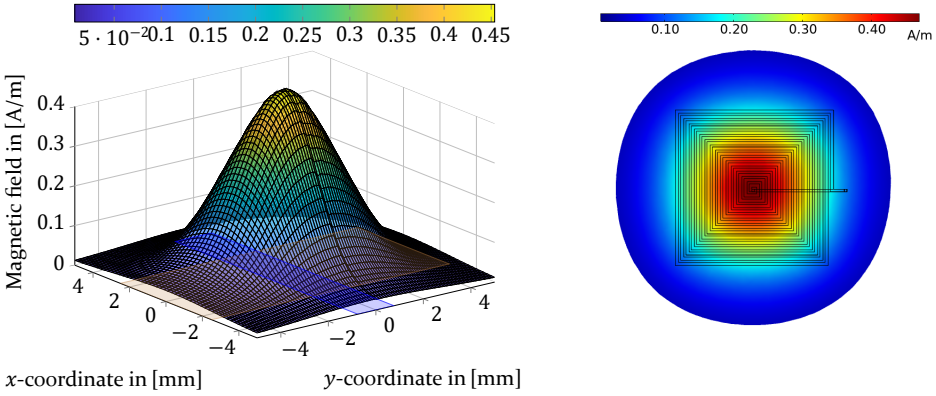

(a) Square

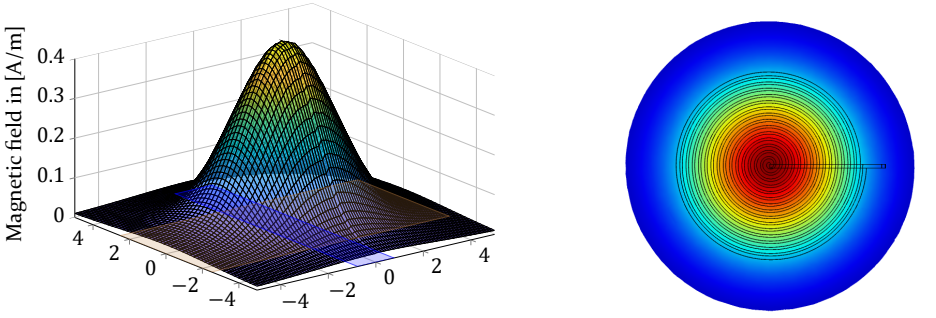

(b) Circular

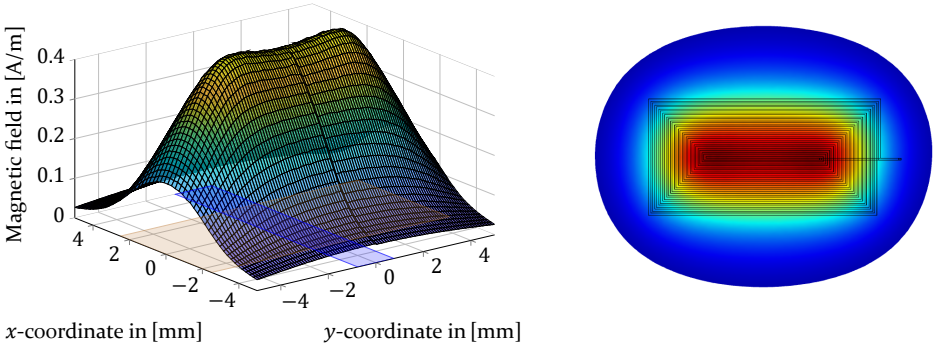

(c) Rectangle

Figure 39: Comparison between the magnetic field strength in [A/m] from different planar coils at distance 1 mm above their surfaces. 3D-view of the fields exist on the left-side, while the 2D-view is shown on the right-side. Shaded blue and brown colors show where the propagation tube and coil exist, respectively.

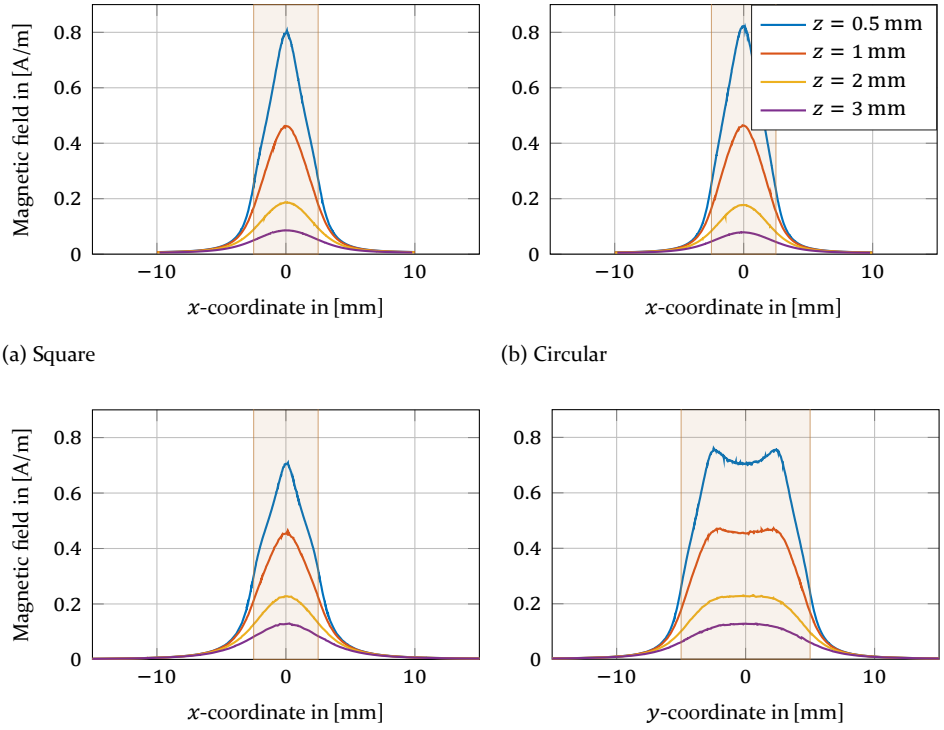

(a) Square

(b) Circular

(c) Rectangular, along the $x-$axis

(d) Rectangular, along the $y-$axis

Figure 40: Magnetic field strength due to the different planar coils at different z-positions above their surfaces. Shaded area shows where the coils exist.

For the square (Fig. 39a) and circular (Fig. 39b) coils, which are centered on the xy-plane, the magnetic field obtained is maximum directly along the z-axis. Although the geometry of the square coil is rotationally asymmetric, its magnetic field is similar to the circular coil, whose field is symmetric about the z-axis. The fields of the planar coils are mostly confined to the regions directly above their surfaces, with non-significant stray fields outside their borders. However, the field decays very fast (almost by half for double distance) in the vertical direction, as shown in Figs.40a and 40b. These results are consistent with the field analysis concluded from the analytical solution in subsection 3.2.3.6. The rectangular planar coil is also studied, as shown in Fig. 39c. Its field is maximum along the length of its (smallest) center loop. The field strength is relatively low compared to the other two planar coils, as seen Figs. 40c and 40d. However, it decays comparatively slow in the vertical direction.

5.2.3 Different Studied Scenarios

In this subsection, the system response for each planar coil is obtained separately when the particles propagate horizontally parallel to its surface. In all scenarios, the particles are assumed to be uniformly distributed inside a cylinder of a fixed radius of 1 mm and a variable length of $l_n \in \{3, 3.5, ..., 30\}$ mm fastened at a horizontal distance of 10 mm away from the center of the employed coil. As before, increasing the length of the cylinder decreases its volume susceptibility. The vertical distance between the cylinder and all detectors is set to 0.1 mm, which describes the direct contact with the cylinder. The detected signal is calculated according to Eq. (104).

5.2.3.1 Comparison of System Responses by the Different Coils

The system responses due to the different planar coils are obtained and compared with that detected by a solenoid of the same detection length $L_{\text{Susc}} = 5$ mm, an inner radius of 1.1 mm, a thickness of 0.1 mm, and has 15 wire-turns.

As shown in Fig. 41, the detected signal by the solenoid is almost five times stronger than that is detected by the circular planar coil, which also shows superiority over the other two coils. The signal from the rectangular planar coil appears to be the weakest. Although the signal detected by the circular coil is relatively weak, it is distinguishable and can be amplified and decoded correctly. Because the employed solenoid is considered long, the

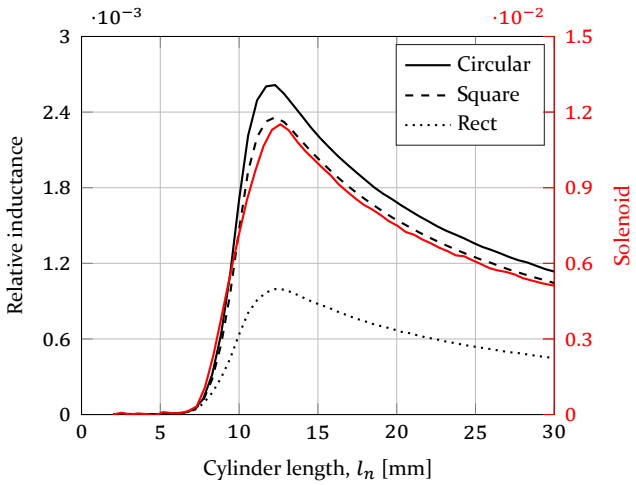

Figure 41: System responses due to the different coils.

non-homogeneous field at its ends is negligible, and the field is assumed to be confined to its inner domain. Therefore, no signal is expected to be detected before the particles enter the solenoid, and its corresponding curve is detected simultaneously with the curves from the planar coils.

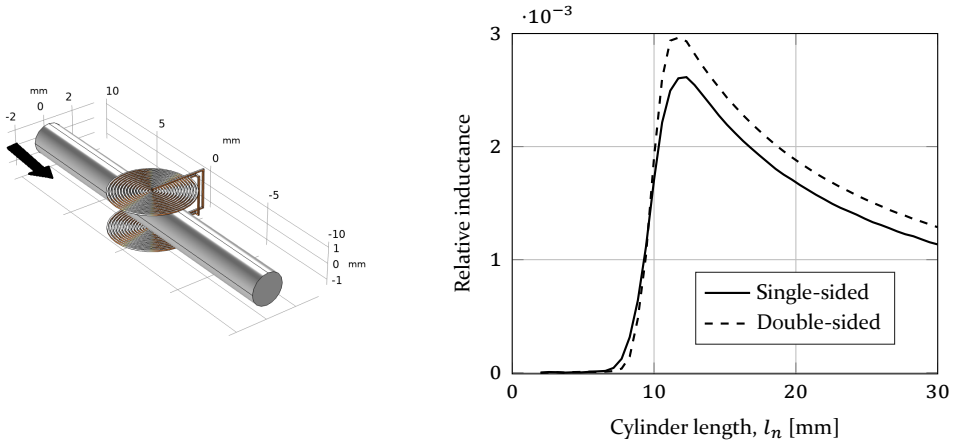

(a) SPIONs-filled cylinder goes through a double-sided planar coil

(b) System response

Figure 42: Geometry and system response for a double-sided planar coil.

5.2.3.2 Double-sided Planar Coil

In Fig. 42, instead of using a single-sided coil, the circular planar coil is chosen to be placed above and below the tube, as shown in Fig. 42a. Its detected signal due to movement of particles is compared with the system response from the single-sided circular coil, as shown in Fig. 42b.

Distributing multiple numbers of planar coils around the tube strengthens the detected signal. However, the coils should be distributed such that their magnetic fields are constructively added in the detection region. Also, instead of using flat coils, the new technologies for coil manufacturing can be used to build folding and bending coils, which are flexible and take the shape of the surface on which they are placed.

5.2.3.3 Multi-layer Planar Coils

In Fig. 43, the system responses of the circular planar coils with and without aperture are compared. In addition, the coil with aperture (Fig. 38d) is replicated eight times within the detection region such that the distance between

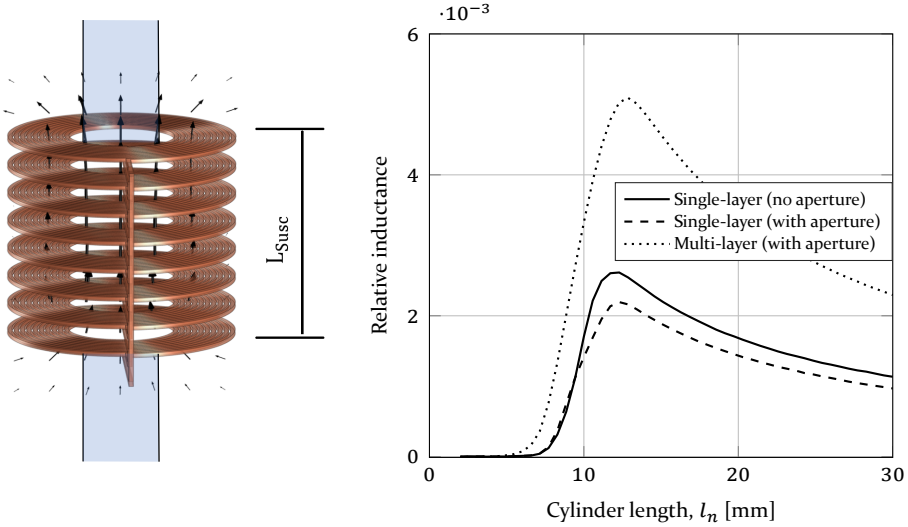

(a) Multi-layer planar coil. Black arrows represent its magnetic field.

(b) System response

Figure 43: System responses due to the movement of a SPIONs-filled cylinder through the detection regions of different planar coils.

the first and last coil equals the detection length L_{Susc} with an equal separate distance between every two successive coils, see Fig. 43a. This structure imitates a cylindrical coil made of planar coils, which can be easily embedded into a Printed Circuit Board (PCB), i.e., sandwiched between the layers. However, instead of the propagation parallel to the surface of the single-layer coil, in the multi-layer structure, the tube passes through the aperture.

The results are depicted in Fig. 43b. As expected, the detected signal by the multi-layer coil is stronger than that detected by the other two coils. The performance of the single-layer coil with aperture is considered the worst. Also, because the fields at both ends of the multi-layer coil are not limited to its physical length L_{Susc}, it has a longer virtual length, and it detects the particles before they enter its borders. Hence, its corresponding curve precedes the curves of the single-layer coils despite the channel length is equal in all three scenarios, reducing the delay between the transmitter and receiver. However, because the particles stay longer before they leave the magnetic field of the multi-layer coil on the exit-side, its detected pulse is relatively wide, reducing its aspect ratio (height/width). Therefore, the difference between the virtual and physical length of the detector should be taken into consideration during the design process of such systems.

6 Modeling and Experimental Verification

6.1 Overview of All Applied Analysis Methods

In this chapter, five different methods, collected in Fig. 44, are used to estimate the system response of the SPIONs-based testbed.

The first method is fully numeric, where an FEM model of the testbed is entirely built in the COMSOL multiphysics simulator. The particles are released into the channel and detected by the susceptometer (reference detector).

In contrast, the second method is purely analytic, in which the weighting function derived in subsection 4.3.2.2 together with the analytical laminar profile derived in subsection 4.1.2 are used to estimate the relative inductance. However, as seen in Table 2, this method involves three assumptions: a rotationally symmetric model, an ideal detector, and a negligible radial dependency ($R_{\mathrm{Ch}} << R_{\mathrm{RX}}$) to ensure that the tube is placed in a homogeneous magnetic field.

In the third method, the particles are assumed to be uniformly distributed and confined between the inner and outer radii of the parabolic laminar profile, which is built in COMSOL Multiphysics as a solid geometry of a specific volume susceptibility, i.e., similar to the SPIONs-filled cylinders used in Chapter 5. Then, this solid laminar profile is moved in time-steps into the susceptometer. This method is valid only in the case of a rotationally symmetric model.

In the fourth method, the Muliphysics simulation between the fluidic and magnetic domains is decoupled to two separate simulations. One is a single domain model of the fluidic channel with its propagating particles simulated to obtain their distribution within the detection region. In the thesis, this model is used (similar to the second method) together with the sensitivity curve of the susceptometer. Instead of exploiting the magnetic properties of the particles, their distribution and density within the detector are employed for estimating the system response. Two assumptions are taken: no radial dependency and an ideal detector. However, if the channel is placed in a region where the field is non-homogeneous, another single domain simulation for the detector is needed to export its magnetic field distribution to be used together with the particle density in Eq. (130) to efficiently estimate the system response. In that case, only one assumption is taken, i.e., ideal detector.

Table 2: Assumptions and solutions used in estimating the system response of the SPIONs-based testbed.

Method	Solution	Assumptions	Rotationally symmetric channel	Effort
1.	Fully numeric	-	Not mandatory	☹
2.	Fully analytic	$R_{Ch} << R_{RX}$, ideal detector	Mandatory	☺
3.	Hybrid	-	Mandatory	😐
4.	Hybrid	$R_{Ch} << R_{RX}$, ideal detector	Not mandatory	😐
5.	Fully experimental	-	Not mandatory	n. d.

Finally, experimental studies are conducted in the fifth method to obtain the volume susceptibility directly from the susceptometer.

In the following, for simplicity, the 2D rotationally symmetric SPIONs-based testbed is initially employed to study the varied parameters of the system. Then, the first four methods are compared. Finally, only the fourth method is used with a 3D simulated-based model of the testbed to estimate its system response, which is then compared with the conducted experiments.

6.1.1 Standard Setup

Many parameters, collected in Table 3, can affect the overall system response. Due to the large parameter space, each parameter is studied separately, assuming the other parameters are fixed. The standard setup parameters used in this model are $Q_{\text{inj,o}} = 5.26\,\text{mL/min}$, $Q_{BG} = 5\,\text{mL/min}$, $V_{Inj} = 14\,\mu\text{L}$, $L_{Ch} = 50\,\text{mm}$, $R_{Ch} = 0.76\,\text{mm}$, $L_{RX} = 5\,\text{mm}$ and $R_{RX} = 5\,\text{mm}$, unless any change is introduced in each of the following subsections.

6.1.2 Performance Metrics

Digital filters are used in conventional communication systems to shape the transmitted pulses such that the ISI is reduced. However, this feature is not yet applicable in the MC system and received pulses suffer from a relatively high delay spread (long-tail). Hence, two performance metrics are used to investigate and compare the system response due to the different parameters, namely the Peak Maximum of the detected signal to its Full Duration at Half Maximum (PMFDHM) and Delay to Peak Maximum (DPM). Having a large PMFDHM gives a tall and narrow system response profile, reducing the ISI. The DPM is the time from the start of the particle injection to the time where the peak maximum is reached, T_{max}, divided by the peak maximum. The

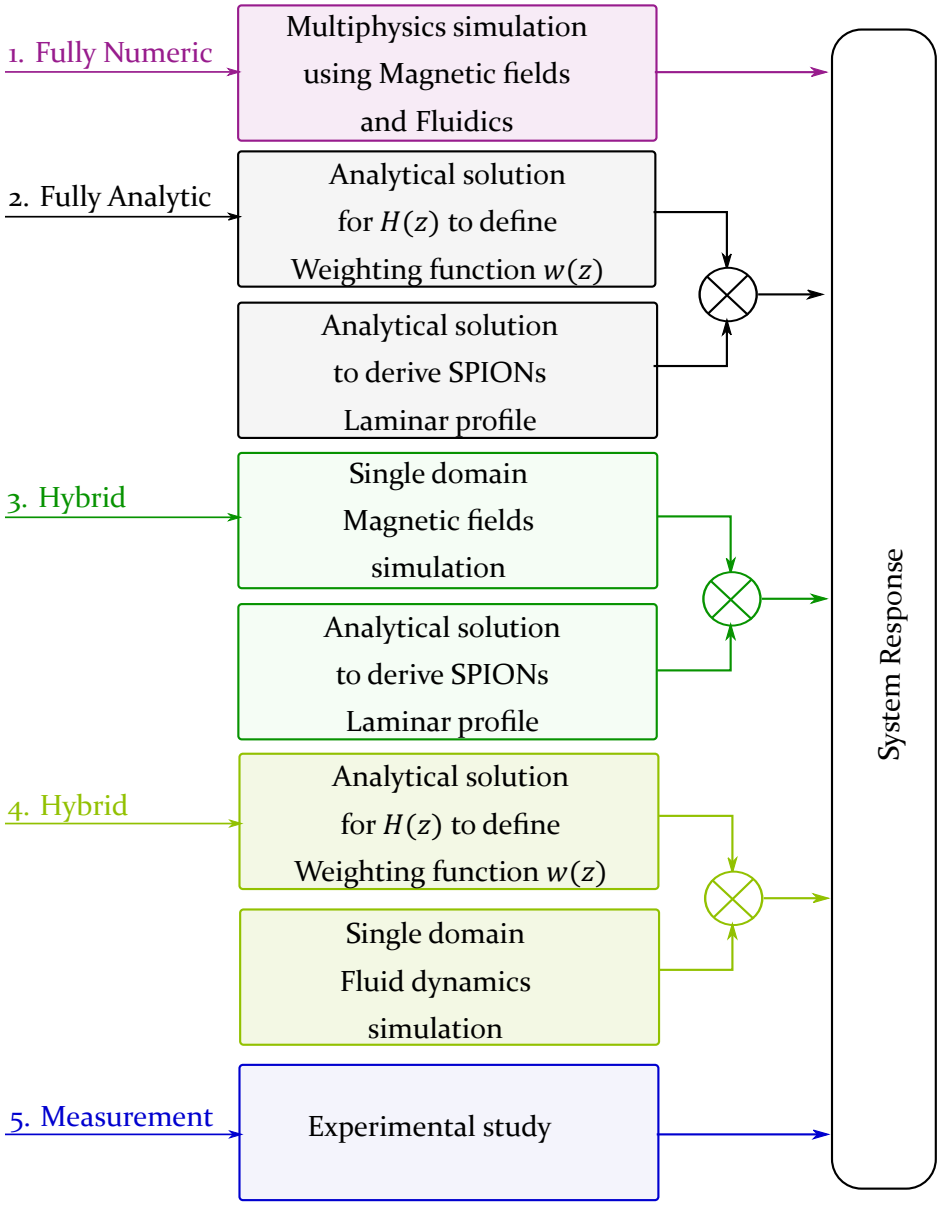

Figure 44: Schematic view of the different methods that can be used to estimate the system response of the SPIONs-based testbed.

shorter this time delay, the faster the signal is detected and decoded. In addition, some of the time durations defined in subsection 4.1.2 are employed.

6.2 Fully Numerical Detection Method

An FEM model of the simplified SPIONs-based testbed is built in the COMSOL multiphysics simulation software. The testbed parameters defined in Table 3 are studied for the transmitter, channel, and receiver. The values of the standard setup in the table are consistently applied, except for the parameters to be studied.

6.2.1 Simulation Setup

As shown in Fig. 45, the model is built in a 2D axisymmetric domain due to its rotational symmetry. Nanoparticles of diameter $d_\mathrm{p} = 50\,\mathrm{nm}$, mass $m_\mathrm{p} = 2.3258 \times 10^{-21}\,\mathrm{kg}$ and volume susceptibility $\chi_\mathrm{m} = 7.28 \times 10^{-3}$ are injected into the propagation channel to be detected by the susceptometer. In order to simulate the injection of particles into the water flow, Laminar Flow and Particle Tracing for Fluid Flow modules are employed. For the susceptometer, the Magnetic Fields submodule from the AC/DC Electric Currents module is utilized.

According to the results from section 4.1.1, a No-slip boundary condition is applied in the Laminar Flow module. Also, a sparse flow is considered, which means that the particles have a negligible effect on the flow; only the flow affects their propagation, i.e., unidirectional coupling. An Inlet with the assigned flow rate is used to imitate the pump. An Outlet is placed at the position where the flow is supposed to reach the waste bin.

In the Particle Tracing for Fluid Flow module, a Drag force based on Stokes's law is applied to the model. The channel wall is chosen to be Bounce, which is typically used to trace microscopic particles in a fluid to conserve their kinetic energy when reflected from the wall. A Release boundary condition is used to inject the particles into the channel. The initial velocity and distribution of particles are proportional to the fluid velocity and the radial coordinate r, respectively. A maximum mesh element size of 0.05 mm is considered. In order to introduce the magnetic properties of the particles, the particle density in each mesh element is obtained by an Accumulator and translated during propagation into volume susceptibility according to Eq. (102). However, in order to reduce the computational complexity, the number of particles injected into the simulated channel is 10^5, which is much lower than that used in the measurement, i.e., $\approx 6 \times 10^{11}$ for $V_\mathrm{Inj} = 14\,\mu\mathrm{L}$.

Table 3: Varied parameters used in the SPIONs-based testbed.

Component	Parameter	Symbol	Standard setup	Studied values
Transmitter	Injection volume	V_{Inj}	14 µL	4.7 : 2.3 : 18.7 µL
	Injection flow rate	$Q_{\text{Inj,o}}$	5.26 mL/min	1.4 : 0.7 : 5.26 mL/min
	Particle distribution	-	Full radius	Center, inner-ring, boundary-ring
Information carrier	Volume susceptibility	χ_m	7.28×10^{-3}	-
	Diameter	d_{P}	50 nm	-
	Mass	m_{P}	2.33×10^{-21} kg	-
Channel	Length	L_{Ch}	50 mm	50 : 10 : 100 mm
	Radius	R_{Ch}	0.76 mm	0.61, 0.875, 1.145, 1.38, 1.585 mm
	Background flow rate	Q_{BG}	5 mL/min	5 : 2.5 : 20 mL/min
Receiver	Coil length	L_{RX}	5 mm	4 : 4 : 24 mm
	Radius	R_{RX}	5 mm	1 : 0.5 : 3.5 mm
	Thickness (or Wire-turns)	ΔR	0.5 mm	0.27 : 0.27 : 1.35 mm

The setup of the susceptometer is defined in subsection 5.1. However, to calculate the system response, the time-dependent coil inductance $L(t)$ due to the particle propagation is first calculated with a sampling rate of 100 Sa/s for a time duration of 3 s. Then, the system response is calculated according to Eq. (104).

6.2.2 Transmitter

In this subsection, only changing the initial position or distribution of the particles inside the transmitter is studied. However, in the next section, different injection volumes and flow rates are applied, from which the system responses due to the fully numeric and the fully analytic methods are compared and analyzed.

6.2.2.1 Changing Initial Particle Distribution

Instead of distributing the particles uniformly across the whole cross-sectional area of the transmitter, three different scenarios are considered, as shown in Fig. 46. In the former scenario (Fig. 46a), the particles are assumed to be injected from a cylinder of radius 0.57 mm placed directly at the center of the transmitter, i.e., imitating the injection using a needle fixed at the tube center. This scenario is convergent with a case in which the particles are distributed along the radial direction of the transmitter proportional to the parabolic velocity profile, i.e., more particles exist at the center of the tube

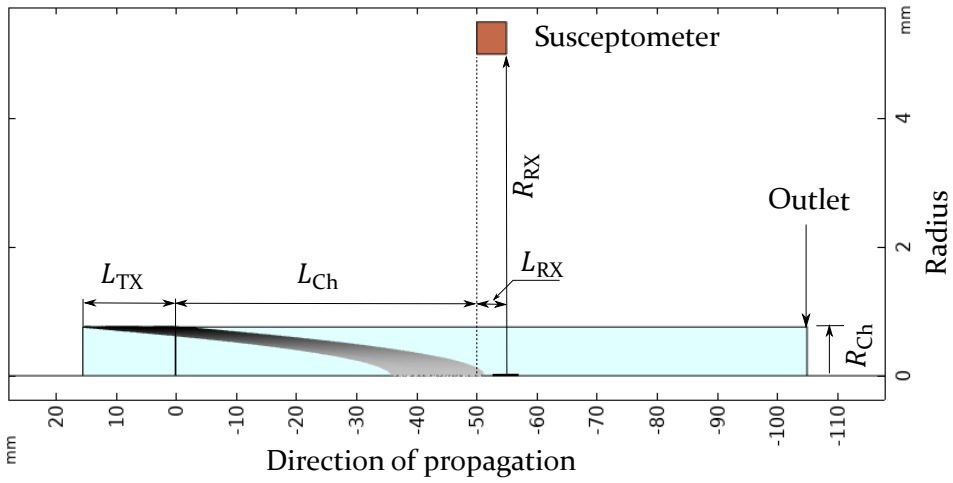

Figure 45: A 2D axisymmetric FEM model of the testbed, in which the nanoparticles are released from the transmitter into a laminar water flow and detected by the susceptometer.

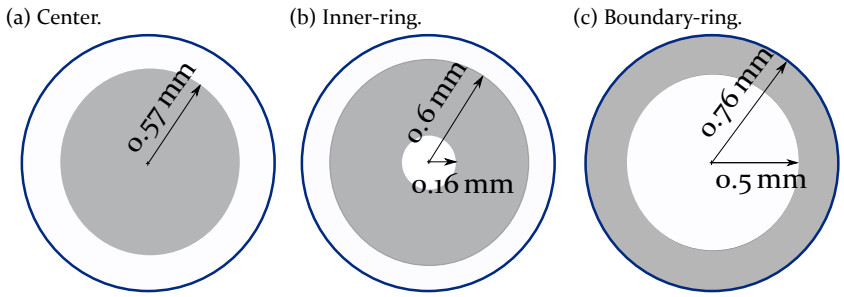

Figure 46: Cross-sectional area of the transmitter. Grey color represents the distributed SPIONs.

and fewer particles near the boundary. In the second scenario (Fig. 46b), the position of injection is shifted in the radial direction such that the particles are assumed to be confined inside an inner-ring cylinder, whose inner and outer radii are 0.16 mm and 0.6 mm, respectively. In the latter scenario (Fig. 46c), the particles are injected into the channel from a boundary-ring cylinder, whose inner radius is 0.5 mm and has the same outer radius as the standard channel. This scenario is convergent with a case in which the particles are distributed along the radial direction of the transmitter proportional to the radial coordinate r, i.e., more particles exist near the inner boundaries of the tube and fewer particles near the center. For a fixed transmitter length, the radii are chosen such that the particles are confined inside the same volume.

The results are demonstrated in Fig. 47. The receiver curves are depicted in Fig. 47a and performance metrics in Fig. 47b. When the particles are injected directly at the tube center, where the flow velocity is maximum, the time delay between the particle injection and detection becomes relatively short. Also, the magnetic field in this region is relatively weak, which leads to weak system response. Note that at high propagation velocities, a very high sampling rate is required. Otherwise, the detector does not precisely detect the propagating particles, negatively affecting the accuracy of the detected signal. However, because the particles propagate with high velocities inside the channel, a negligible tail is observed. On the contrary, the injection near the boundary, where the flow velocity is either low or zero directly at the boundary, elongates the curve due to the slow motion of particles within the detector. Also, it introduces a longer time delay. A compromise choice between these two cases is the inner-ring scenario, in which the particles propagate roughly at the average velocity, improving the performance.

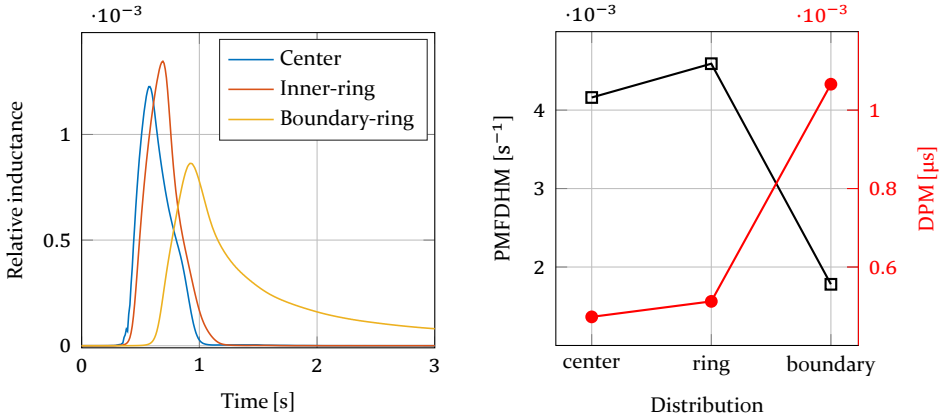

(a) Relative inductance.

(b) Performance metrics.

Figure 47: Relative inductance and performance metrics due to different particle distribution inside the transmitter.

6.2.3 Propagation Channel

In this subsection, only changing the length and width of the channel is investigated. However, the effect of different propagation flow rates and injected volume is studied in section 6.3 using the numerical and analytical methods.

6.2.3.1 Propagation Lengths

From subsection 3.1.5.2, for the SPIONs-based testbed, the longest hydrodynamic entry length required by the laminar flow to fully develop is $L_{h,\text{Laminar}} \approx 26.5$ mm. Hence, in this study, longer transmission lengths are considered $L_{\text{Ch}} \in \{50, 60, ..., 100\}$ mm, as shown in Fig. 48.

The system response is depicted in Fig. 48a. As the transmission distance increases, a considerable signal decay is observed. However, despite the transmission length increases linearly, the PMFDHM decays exponentially, as shown in Fig. 48b. As expected, decreasing the transmission length improves the detected signal. The time delay T_{D} and time required to reach the peak maximum T_{max} are linearly reduced (see Fig. 48c), achieving higher performance metrics.

6.2.3.2 Channel Widths

Restricted by the dimensions of the standard tubes used in the experimental study, a tube of variable radius $R_{\text{Ch}} \in \{0.61, 0.875, 1.145, 1.38, 1.585\}$ mm

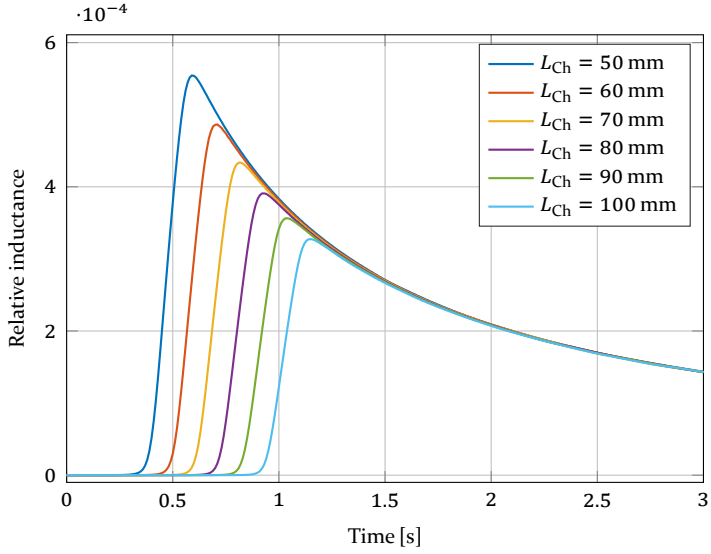

(a) Relative inductance

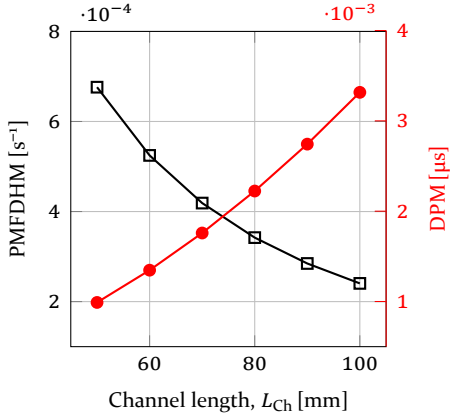

(b) Performance metrics

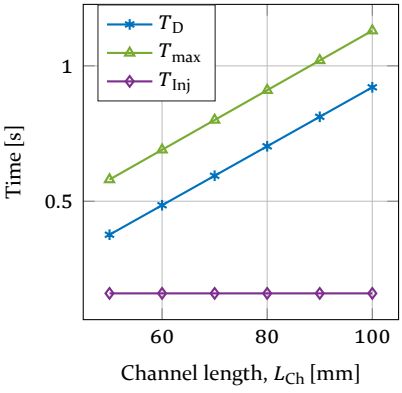

(c) Important time durations

Figure 48: System response due to different channel lengths.

is employed (see Fig. 49). According to Eq. (76), for larger tube radii, the propagation velocity of the particles decreases. Hence, in this study, a longer duration of 10 s is assigned to get the full system response and calculate the corresponding performance metrics.

As shown in Fig. 49a, for the same injected particle suspension, increasing the channel radius reduces the particle density inside the detector, which accordingly should reduce its detected signal. However, because the particles are shifted towards the inner boundary of the solenoid, where the magnetic field strength is relatively high and compensates for this reduction in density, the signal is slightly amplified. Although the curves have relatively large heights, they suffer from a high delay spread due to the slow-motion of the propagating particles, degrading the overall system performance, as depicted in Fig. 49b. Increasing the channel radius significantly affects the time delay T_{D} and $T_{\max}$ that increase, as shown in Fig. 49c. In order to speed up the system, higher background flow rates are recommended to compensate for the lack of velocity due to the wide channels. However, turbulence should be then taken into consideration.

Another study that involves varied injection and background flow rates through channels of different widths is given in subsection 6.3.1.3.

6.2.4 Receiver

Detector optimization is a challenging process that aims to design a high-sensitivity receiver to get the optimum system response. In this subsection, we study how changing the coil geometry affects the system response when the parameters of the transmitter and channel are kept fixed.

6.2.4.1 Detection Length

In Fig. 50, the detector length changes from 4 mm to 24 mm in steps of 4 mm. For the standard setup values given in Table 3, the length of the transmitter can be calculated from Eq. (82), which gives $L_{\mathrm{TX}} \approx 15$ mm.

When the detector is relatively shorter than the transmitter, some particles lie outside its detection region and hence do not contribute to the detected signal, as shown Fig. 50a. Increasing the detector's length helps capturing more particles, improving the system response (Fig. 50b), until the whole particles lie within the detection region. After that, any further increment in its length does not significantly contribute to the signal amplitude. However, when the detector length increases, its center of gravity, where the magnetic field is maximum, is shifted in the direction away from TX, which leads

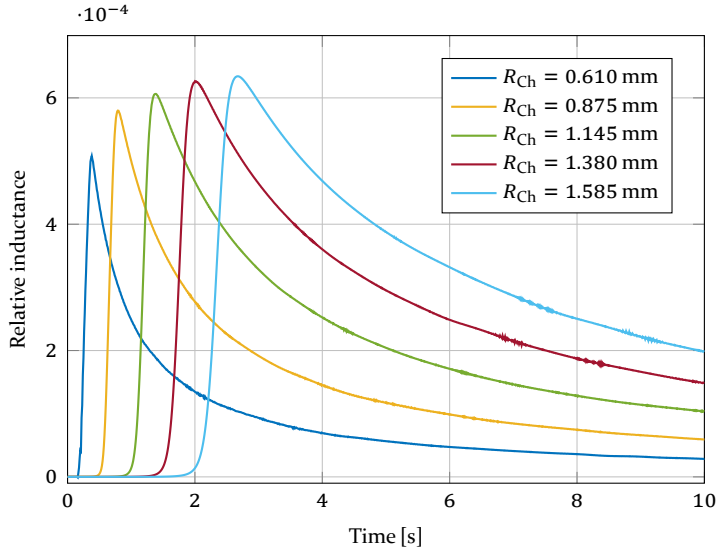

(a) Relative inductance

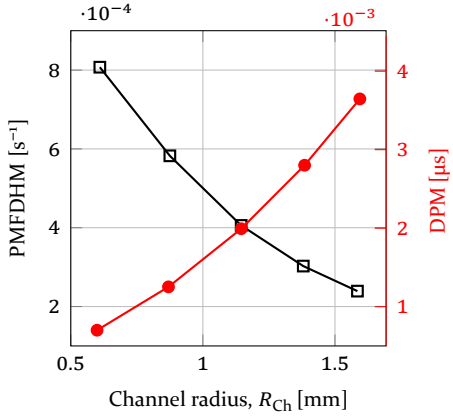

(b) Performance metrics

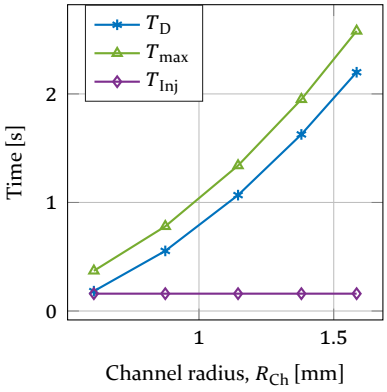

(c) Important time durations

Figure 49: System response due to different channel widths.

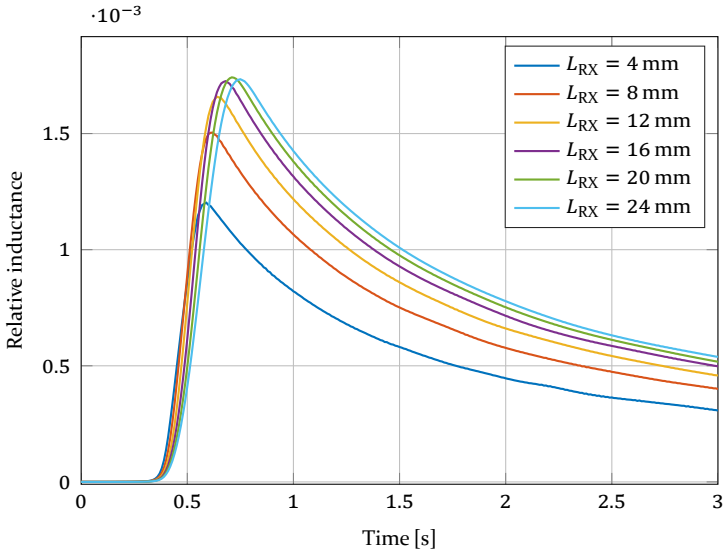

(a) Relative inductance

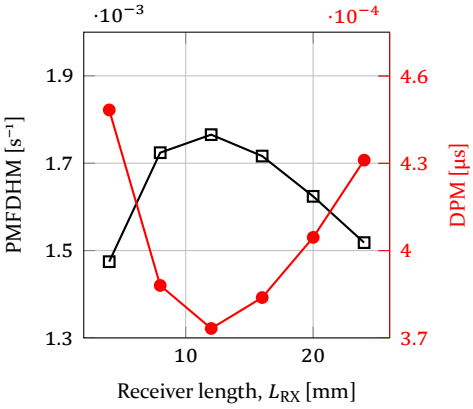

(b) Performance metrics

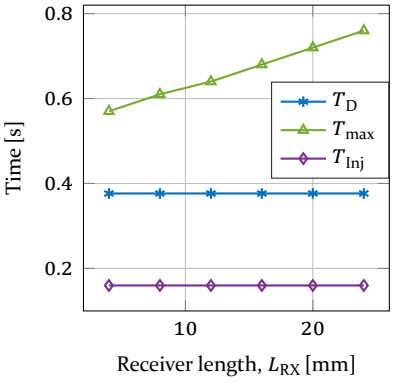

(c) Important time durations

Figure 50: System response due to different receiver lengths.

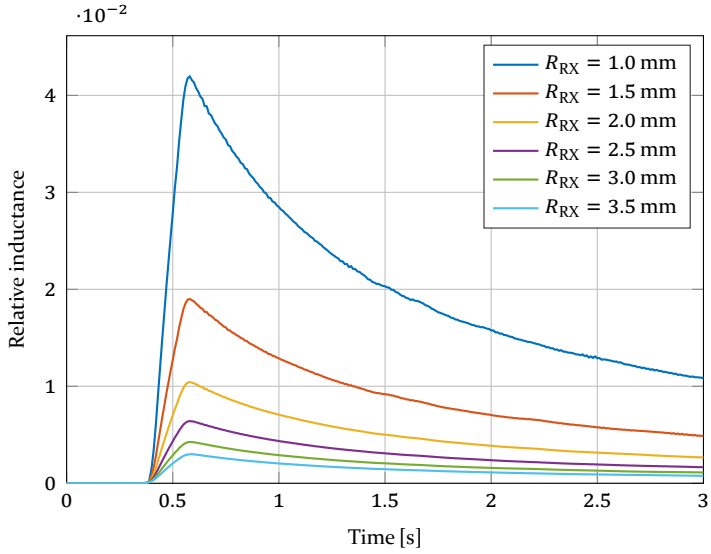

(a) Relative inductance

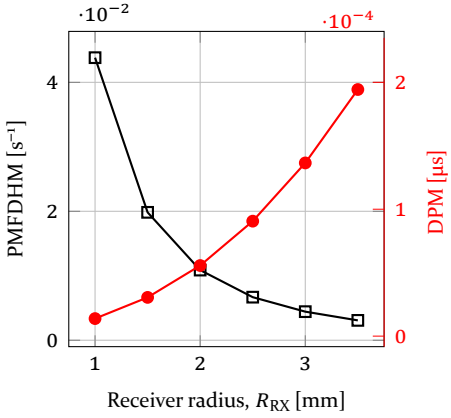

(b) Performance metrics

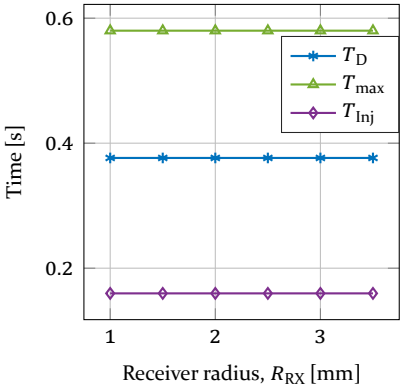

(c) Important time durations

Figure 51: System response due to different receiver widths.

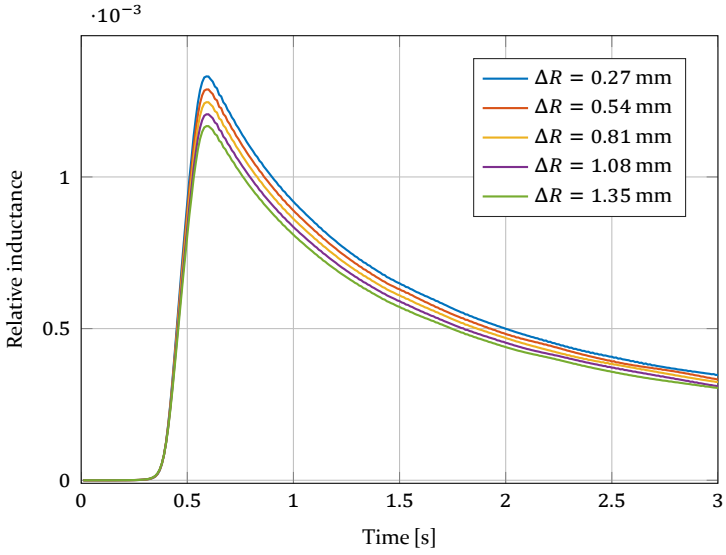

(a) Relative inductance

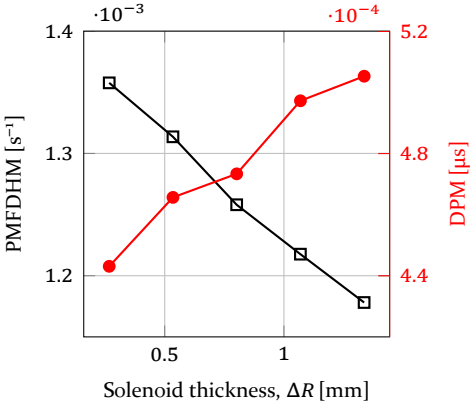

(b) Performance metrics

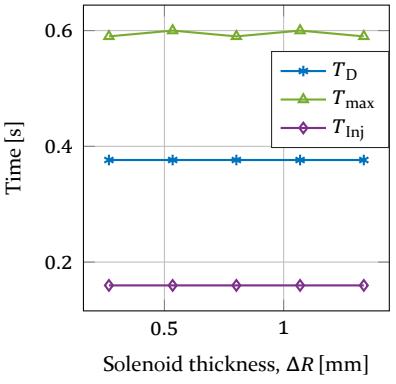

(c) Important time durations

Figure 52: System response due to changing the thickness of the solenoid.

to delaying the peak maximum of the detected pulse and slightly widens it, increasing $T_{\max}$, as depicted in Fig. 50c. Wide pulses with almost fixed amplitudes degrade the system response. As expected, for different detector lengths, the time delay and injection duration remain constant.

6.2.4.2 Receiver width

In Fig. 51, changing the cross-sectional area of the coil is studied, which significantly affects the system response, as seen in Fig. 51a. The radius of the detector is changed from 1.0 mm to 3.5 mm in steps of 0.5 mm.

Although the self-inductance of the solenoid is directly proportional to its cross-sectional area as given in Eq. (111), the relative inductance is inversely proportional to it. A concentric increase of a solenoid about a tube fixed along its center axis degrades the system response, as seen in Fig. 51b. Therefore, it is recommended to build a solenoid of a small cross-sectional area such that the particles propagate directly next to its inner boundary. In all studied scenarios, the position of the maximum peak does not change because the center of gravity of the solenoid is fixed regardless of its diameter. As expected, all time durations remain constant for the different detector radii (see Fig. 51c).

6.2.4.3 Detector Thickness

Here, the effect of changing the number of wire-turns (thickness) on the system response is studied, and the results are depicted in Fig. 52. To keep the detector's length fixed, the increment of the wire-turns appears in adding more wire layers; each layer is of thickness $\Delta R = 0.27$ mm and has approximately 18 wire-turns.

As derived in subsection 4.3.2.2, the detected signal is affected by the field distribution within the detection region, which is influenced by changing the thickness of the solenoid, as described in subsection 3.2.3.5. Adding more layers to the solenoid leads to a large ΔR that accordingly enlarges the average cross-sectional area of the solenoid and reduces its detected signal (see Fig. 52a). Therefore, the performance metrics are inversely proportional to the thickness of the solenoid, seen in Fig. 52b. As expected, changing the number of wire-turns or the solenoid thickness has no effect on the time durations, as demonstrated in Fig. 52c.

Keep in mind that, in this study, the wires are assumed to be uniformly distributed with a negligible separate distance between every two wires.

6.3 Fully Analytical Detection Method

As mentioned in subsection 4.3.2.2, if the radial dependency is negligible, the sensitivity curve of the susceptometer $w(z)$ together with the particle density in its detection region can be used to estimate the system response. However, the particle density can be obtained either directly from the simulation or derived analytically, as described in subsection 4.1.2. Hence, from Eq. (134), Eq. (89), and Eq. (90), the fully analytic estimated system response for the 2D rotationally symmetric model is given by

$$s_{\text{analytic}}(t) = \rho_{\text{Ch}} \cdot \int_{-L_{\text{Sol}}/2}^{L_{\text{Sol}}/2} w(z)\,\pi\left[r_{\text{o}}(z,t)^2 - r_{\text{i}}(z,t)^2\right] dz \tag{138}$$

The sensitivity curve of the susceptometer is directly proportional to its magnetic field along its center axis and it is defined by

$$w(z) \overset{(135),(64)}{=} k_{\text{w}} \cdot w_{\text{B}}(z) \tag{139}$$

where $w_{\text{B}}(z)$ is defined by Eq. (64) and k_{w} is a scaling factor that ensures a minimum MSE between the system responses from the fully numeric and fully analytic methods, its mean value is $7.05878 \cdot 10^{-8}$ with a standard deviation of $8.36237 \cdot 10^{-10}$.

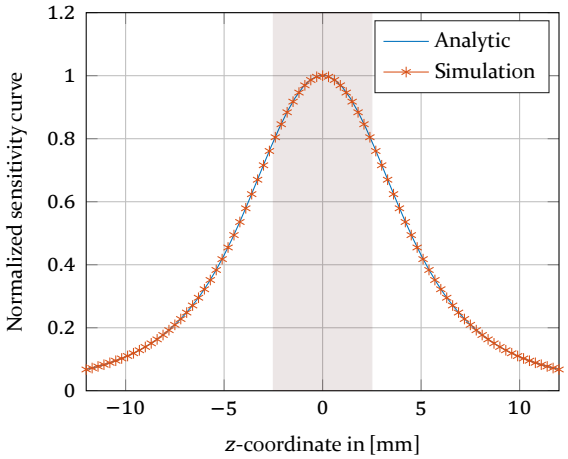

Figure 53: Normalized sensitivity curve of the susceptometer. Shaded area represents where the coil exists.

In Fig. 53, the normalized sensitivity curve of the susceptometer from both the analytical solution and simulation are compared. A perfect agreement between the curves is noticed. The maximum point is located directly at the coil center point, where the contribution of the particles to the signal should be high. Away from the center, the function decays; therefore, their contribution becomes less, i.e., ≈ 80% at both ends of the coil.

6.3.1 Fully Analytical Versus Fully Numerical Solutions

In the previous section, most of the system parameters defined in Table 3 are numerically studied. Here, the remaining parameters: the injection volume and flow rates are studied. Both the analytical and numerical methods are employed to obtain the system responses in a time duration of 2.5 s, from which the scaling factor k_w given in Eq. (139) is determined. In a separate study, varied flow rates are applied to a channel of different widths to compare the system responses and determine MSE between the simulation and analytical solution when the channel width is increased beyond the region where the radial dependency is assumed negligible.

6.3.1.1 Variation of Injection Volumes

Changing the injected volume , $V_{\mathrm{Inj}} \in \{4.7, 7.0, ..., 18.7\}$ µL, of the SPIONs suspension at different injection and background flow rates are investigated in Fig. 54.

As can be seen, there is a good agreement between the results from the analytical and numerical methods. Because the initial particle density is fixed, larger volumes are translated into more SPIONs within the detection region, resulting in higher amplitudes. Also, according to Eq. (74), when large volumes of the particle suspension are injected into the channel with relatively low injection flow rates, the injection duration increases, which reaches approximately 30% of the total detection duration (shown in the last row of Fig. 55) and hence contributes to a relatively long delay of the peak maximum T_{max}, as shown in the corresponding row in Fig. 54. This delay can be mitigated by increasing the injection flow rate, as shown in the first row of the same figures. During the injection, the flow velocity inside the channel is the summation of both background and injection velocities. After that, only the background flow remains that carries the particles to the receiver. This means that for large injection volumes and hence long durations, the particles propagate with high velocities for a relatively long time that accordingly reduces the time delay T_{D} between TX and RX. However, if the particles reach the receiver during the injection, i.e., $T_{\mathrm{Inj}} > T_{\mathrm{th}}$, this time delay remains constant regardless of the injected

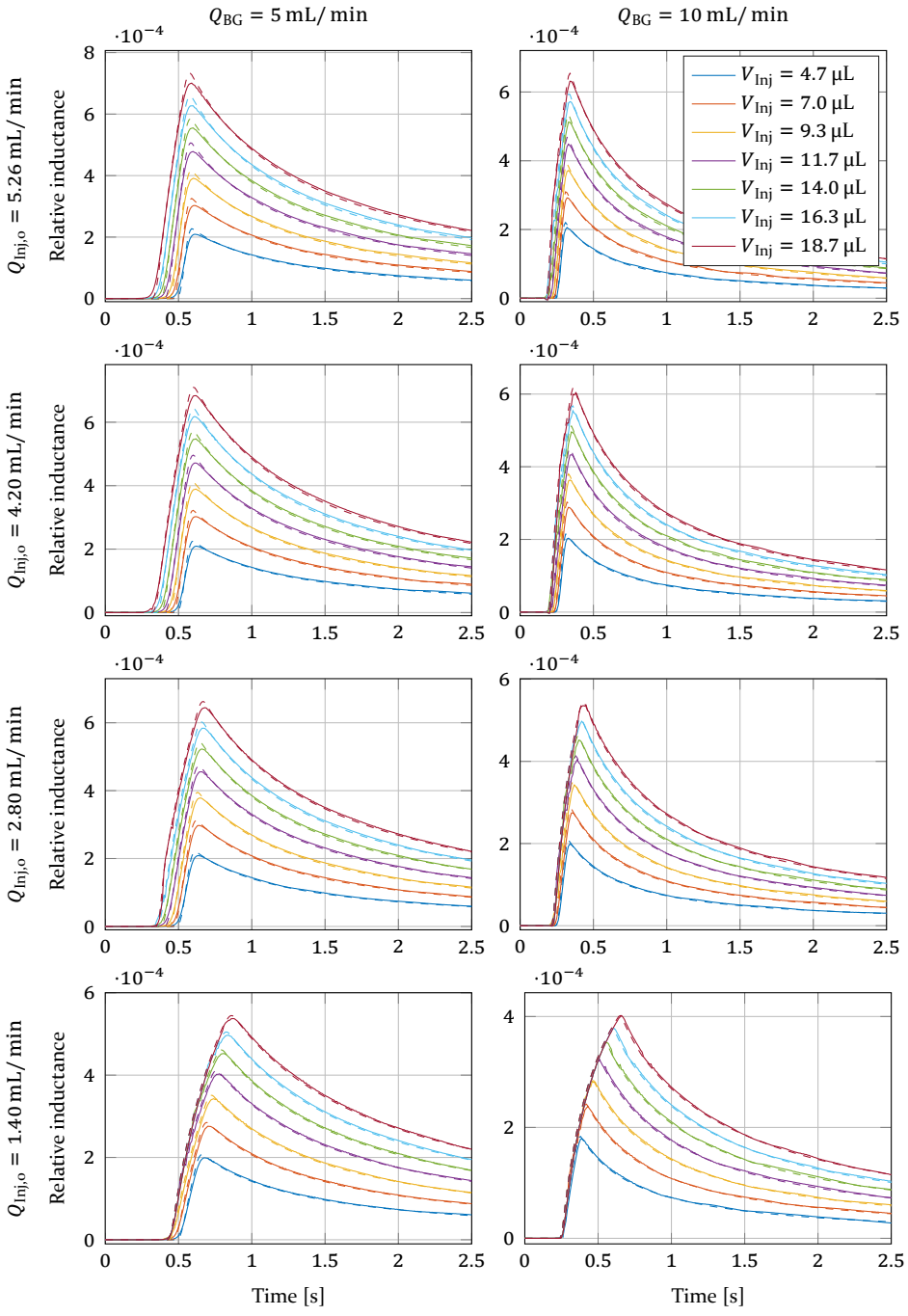

Figure 54: Relative inductance: variation of injection volumes at different flow rates. Background flow rate Q_{BG} and particle injection flow rate $Q_{Inj,o}$ are varied along rows and columns, respectively. Solid and dashed lines are from the numeric and analytic solutions, respectively.

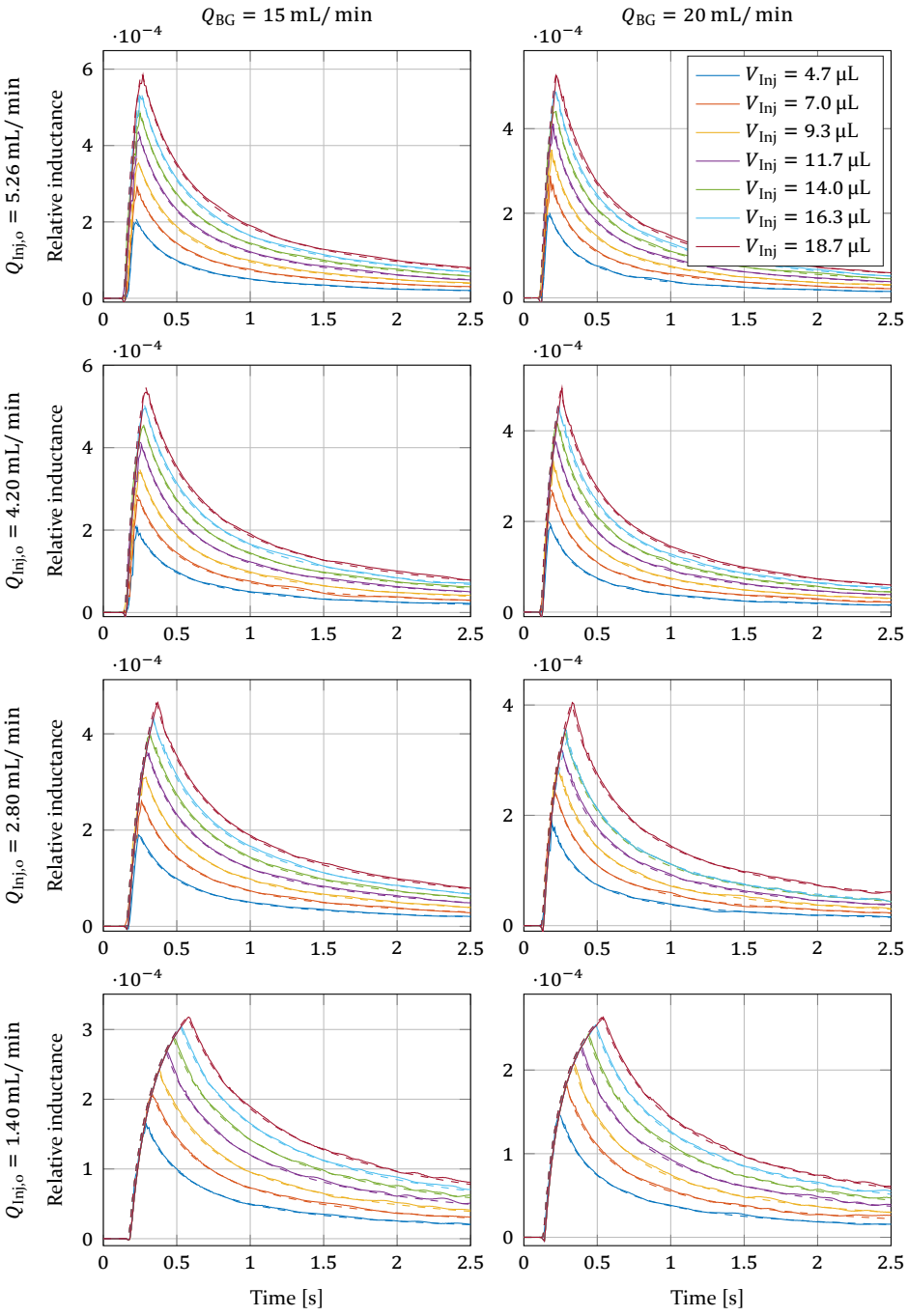

Figure 54: Relative inductance: variation of injection volumes at different flow rates. Background flow rate Q_{BG} and particle injection flow rate $Q_{Inj,o}$ are varied along rows and columns, respectively. Solid and dashed lines are from the numeric and analytic solutions, respectively (cont.).

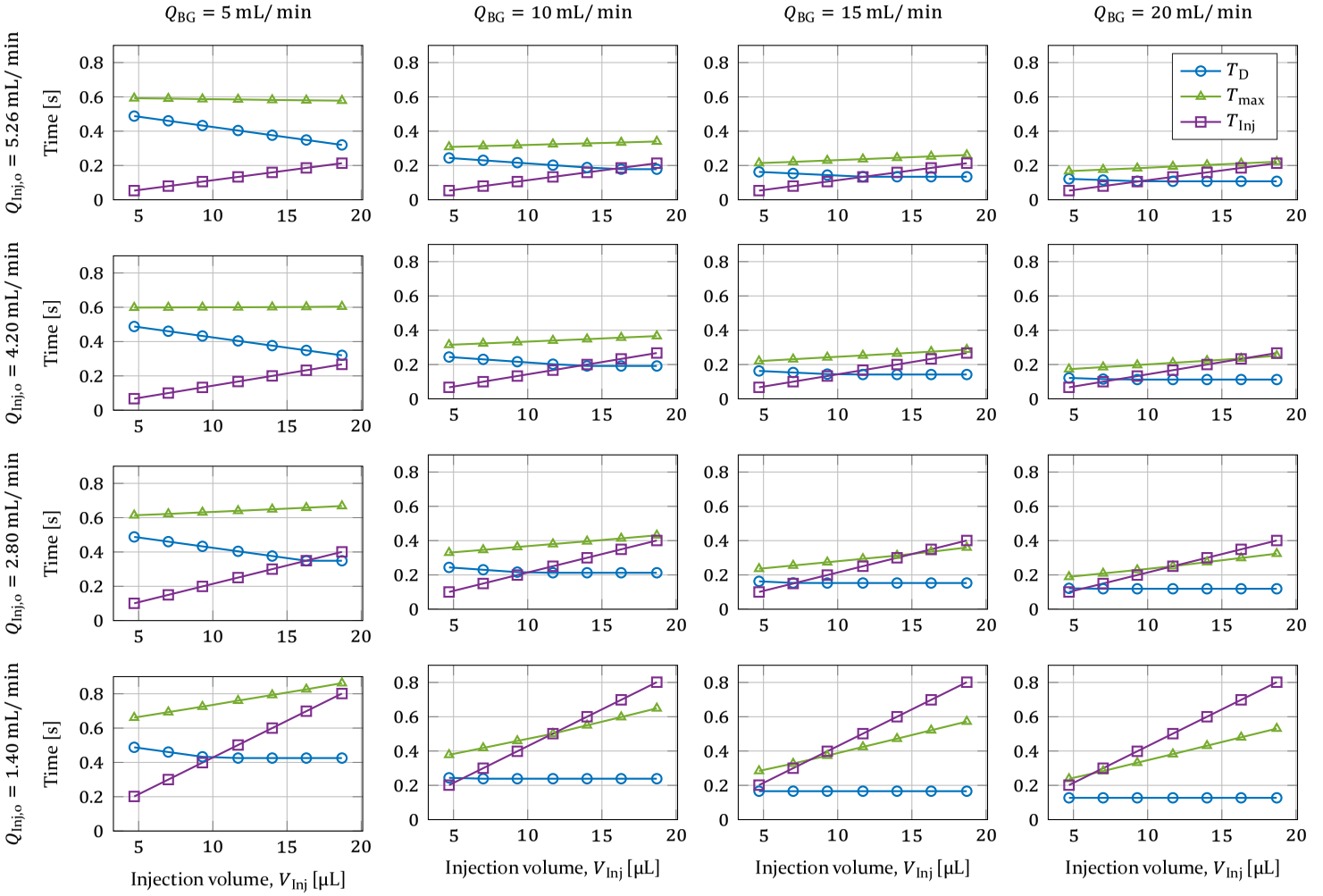

Figure 55: Important time durations due to different injection volumes at varied flow rates. Background flow rate Q_{BG} and particle injection flow rate $Q_{Inj,o}$ are varied along rows and columns, respectively.

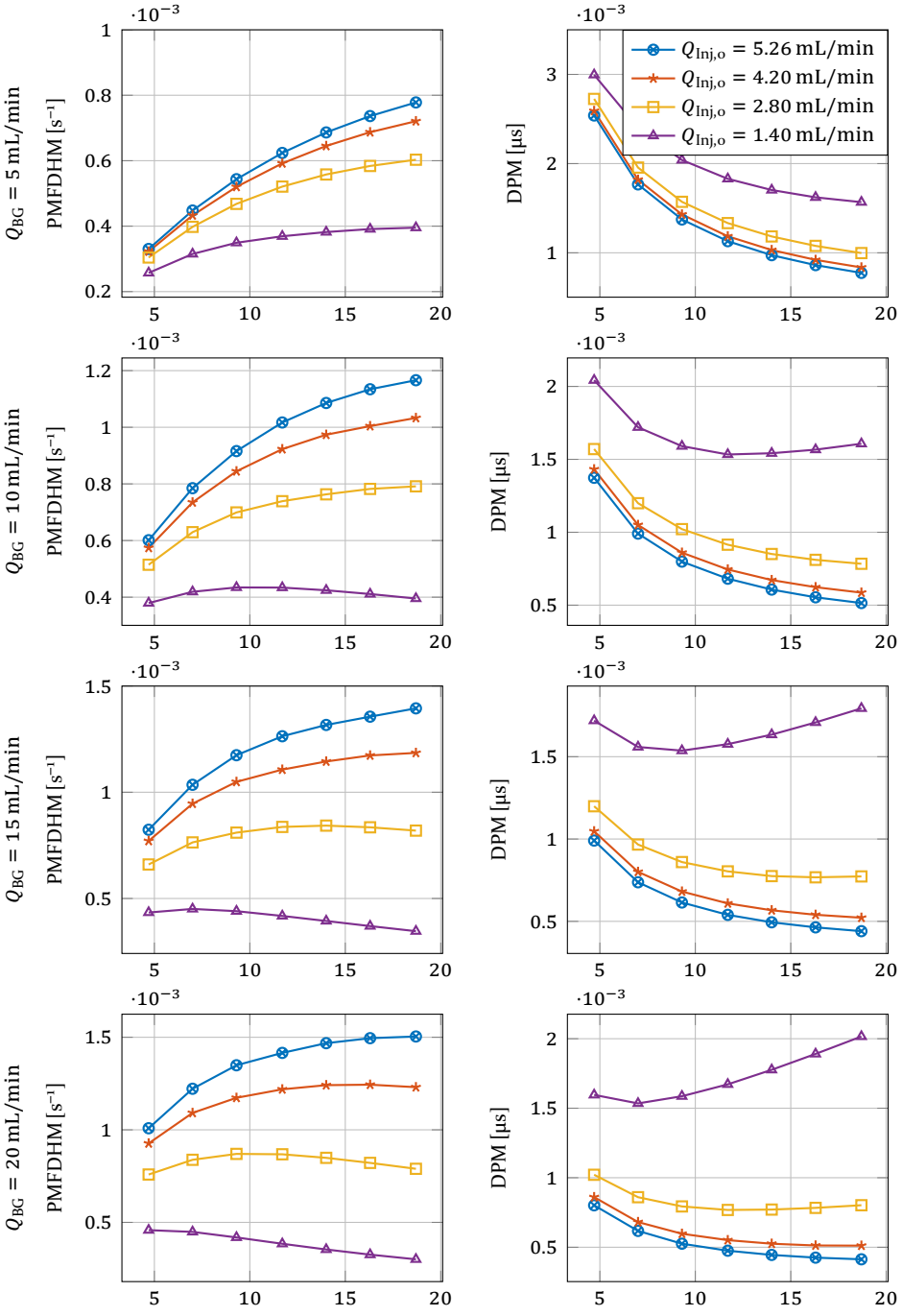

Figure 56: Performance metrics due to different injection volumes at varied flow rates. Each row represents the results at a different background flow rate Q_{BG}.

volume. The system's performance metrics are depicted in Fig. 56. Increasing the injection volume at relatively high flow rates improves the system response. However, when the background flow rate, i.e., $Q_{\mathrm{BG}} \geq 10.0\,\mathrm{mL/min}$, is much higher than the injection flow rate, i.e., $Q_{\mathrm{Inj,o}} = 1.40\,\mathrm{mL/min}$, increasing the volume lengthens the transmitter according to Eq. (82), which may become longer than the channel and/or the receiver, deforming the detected signal and hence reduces the performance metrics.

6.3.1.2 Different Flow Rates

In Fig. 57, the effect of changing the injection flow rate, $Q_{\mathrm{Inj,o}} \in \{\, 1.40, 2.10, \ldots, 5.26 \,\}\,\mathrm{mL/min}$, is studied at different background flow rates, $Q_{\mathrm{BG}} \in \{\, 5.0, 7.50, \ldots, 15.0, 20.0 \,\}\,\mathrm{mL/min}$, and a fixed injection volume of $V_{\mathrm{Inj}} = 14\,\mu\mathrm{L}$.

According to Eq. (82), increasing the injection flow rate shortens the transmitter relative to the employed receiver, strengthening the detected signal as mentioned in subsection 6.2.4.1. Also, it reduces the injection duration and delay required by the pulse to reach its maximum value, as shown in Fig. 58. Hence, the system response is improved, particularly at relatively high background flow rates, i.e., $Q_{\mathrm{BG}} \geq 10.0\,\mathrm{mL/min}$, as depicted in Fig. 59.

Fig. 60 shows the system response when the background flow rate changes at different injection flow rates, while the corresponding essential time durations are depicted in Fig. 61. Signals with relatively low amplitudes are obtained when the background flow rate increases. This result is consistent with the findings in subsection 6.2.2.1 when the particles are injected at the tube center, where the propagation velocity is maximum. In order to improve the system response, the particles are recommended to propagate at medium velocities. As mentioned before, very high background flow rates with very low injection velocities give long transmitters compared to the employed receiver, which reduces the detected signal and accordingly the performance metrics as depicted in Fig. 62. Hence, the transmitter is recommended to be of comparable length to the receiver. For high background velocities and appropriate injection volumes, the particles are carried relatively fast to the receiver, reducing the pulse width and both time delay T_{D} and T_{max}.

In conclusion, the injected volume, flow rate of SPIONs, and background velocity in the channel are three interconnected parameters that should be chosen in line with the other system parameters to improve the overall system performance.

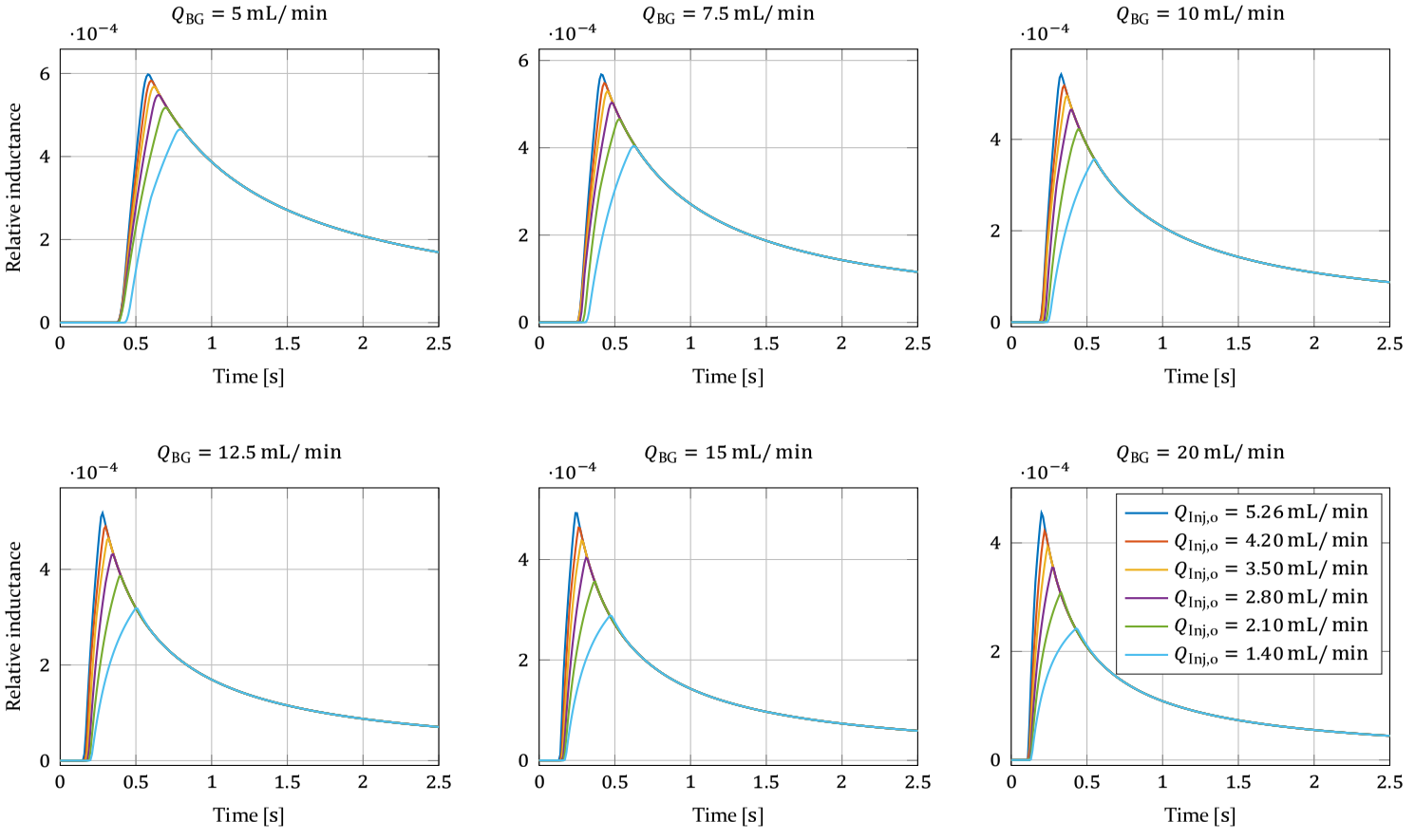

Figure 57: Relative inductance due to different injection flow rates at varied background velocities.

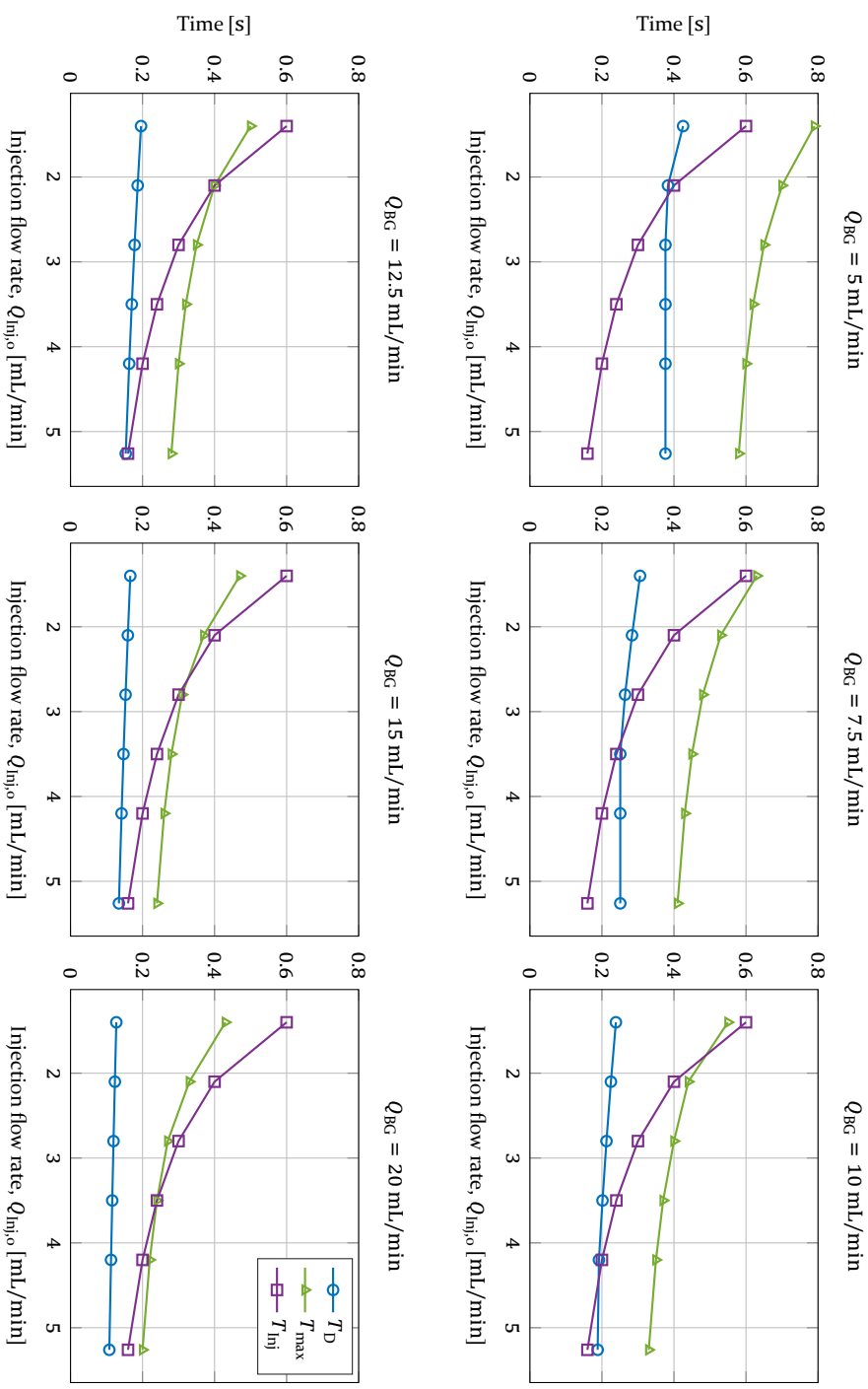

Figure 58: Time durations due to different injection flow rates at varied background velocities.

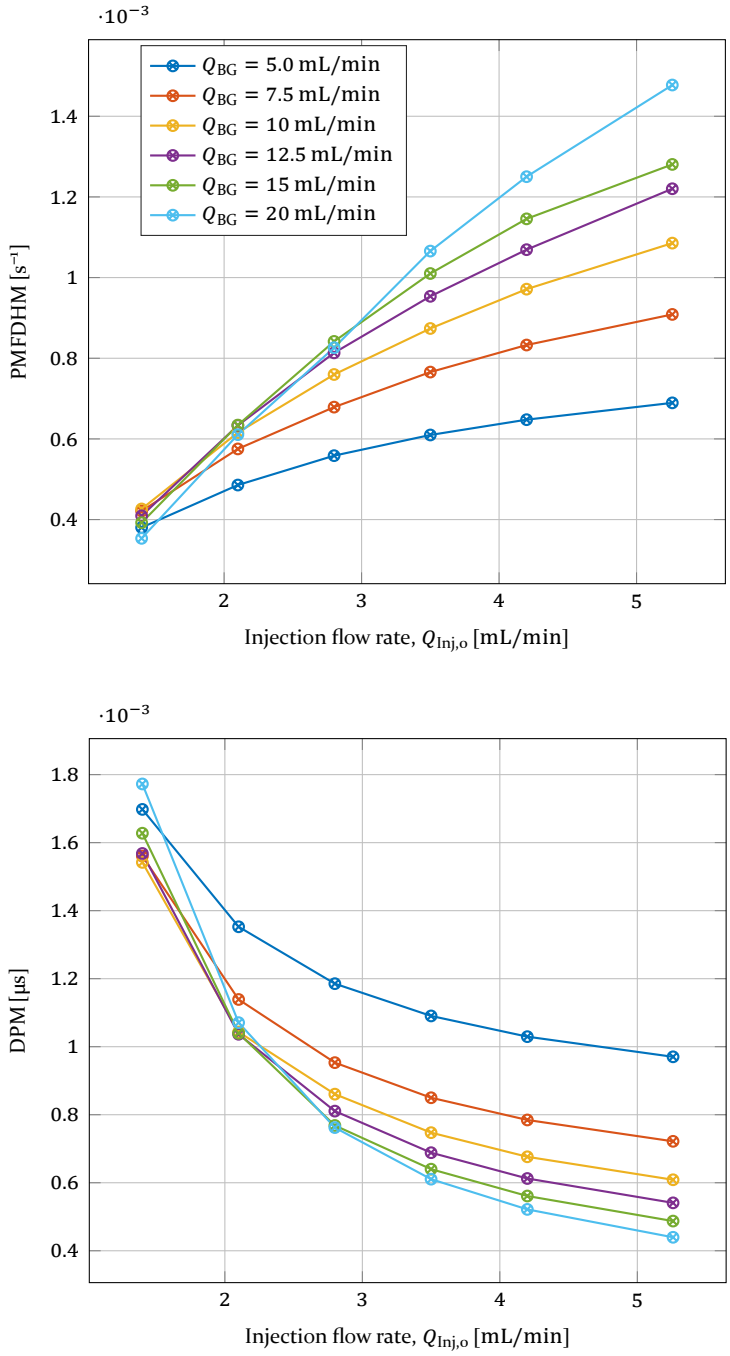

Figure 59: Performance metrics due to different injection flow rates at varied background velocities.

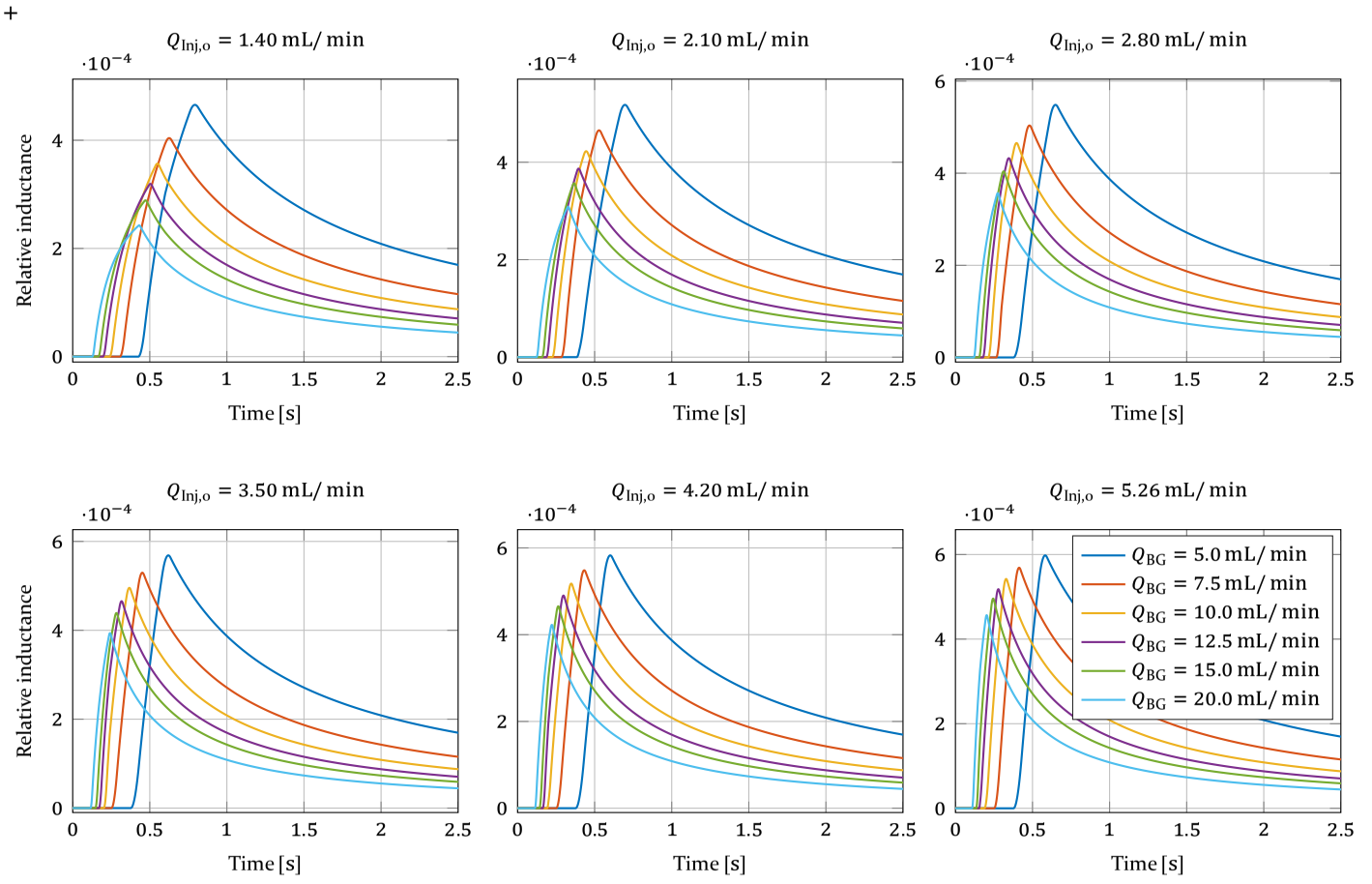

Figure 60: Relative inductance due to different background flow rates at varied injection velocities.

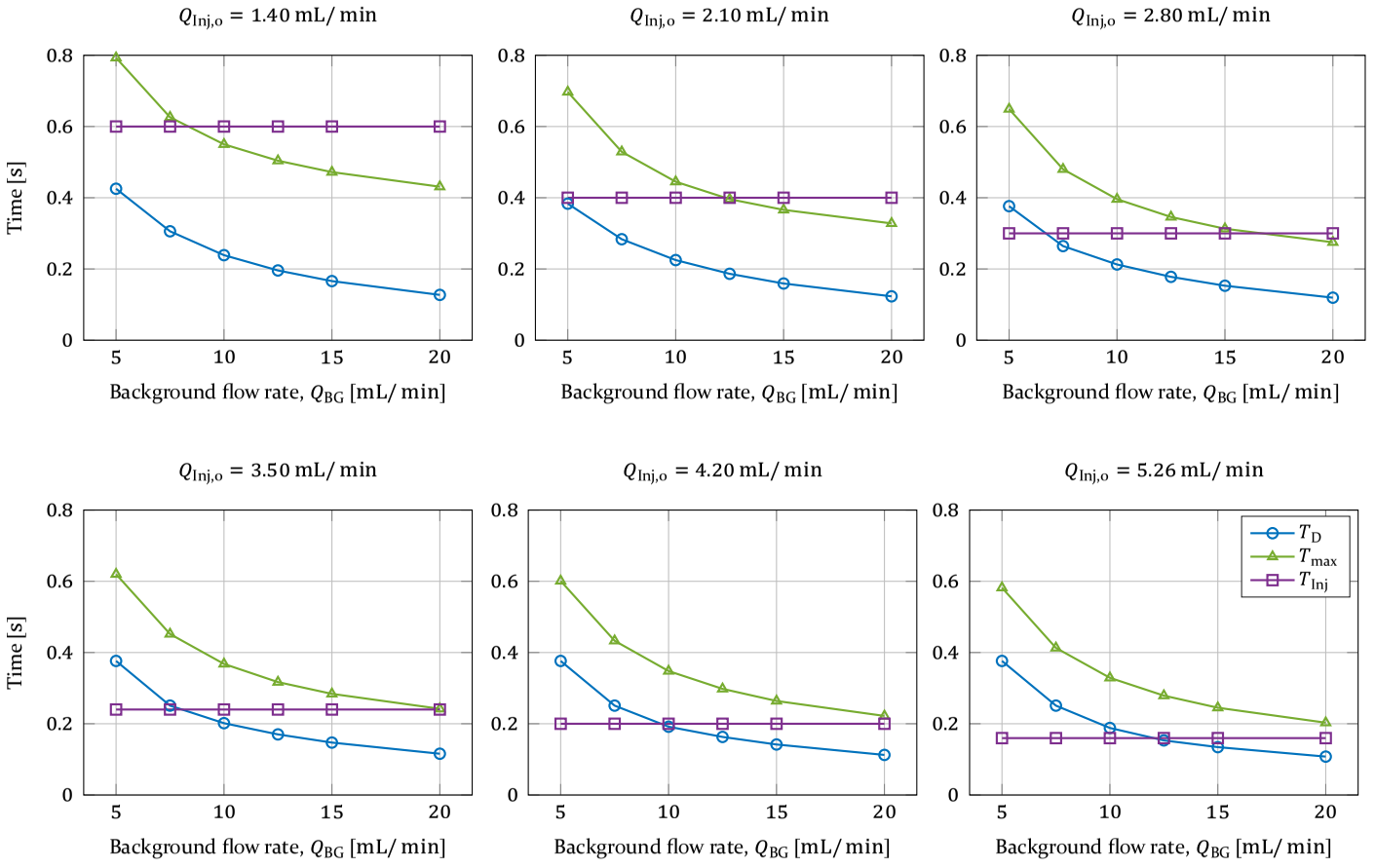

Figure 61: Time durations due to different background flow rates at varied injection velocities.

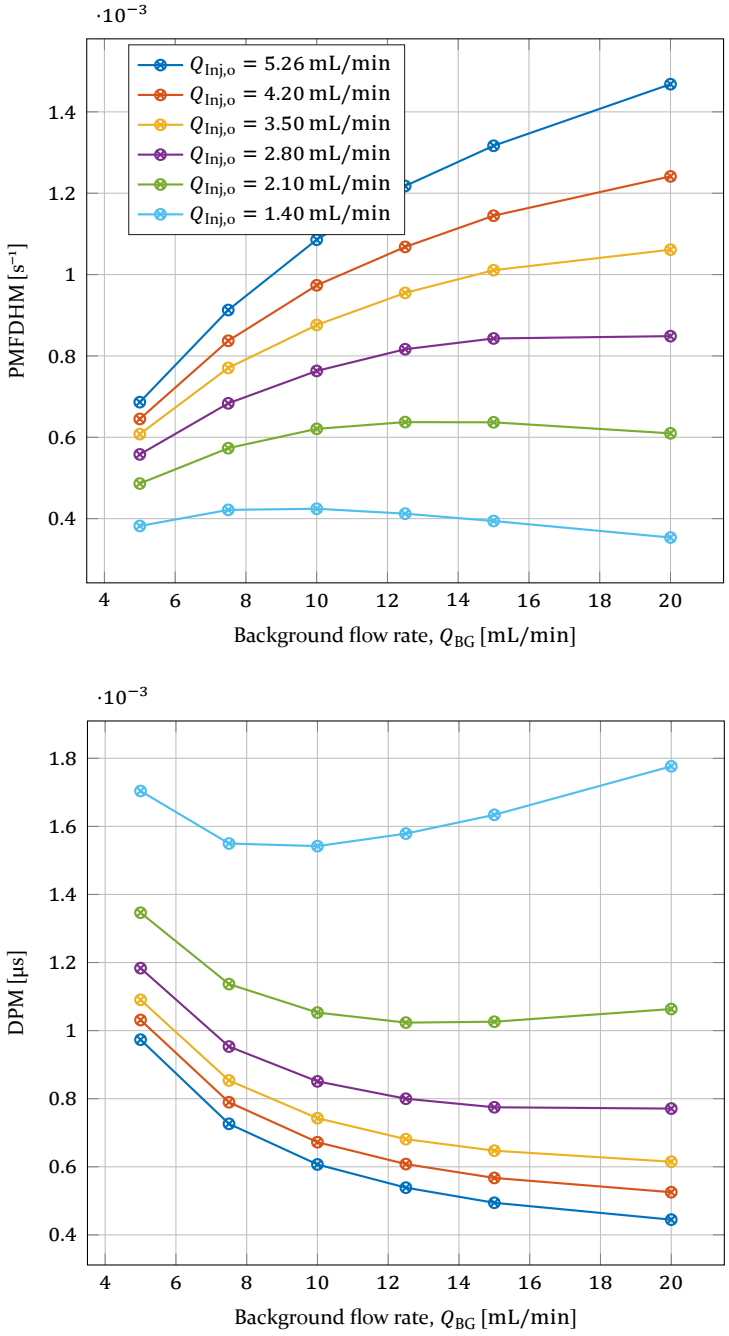

Figure 62: Performance metrics due to different background flow rates at varied injection velocities.

6.3.1.3 Channel Limit

In order to determine how precisely the analytical solution describes the simulated (numerical) model when the channel width is increased beyond the region in which a negligible radial dependency is assumed, varied flow rates are applied to channels of different widths, $R_{\mathrm{Ch}} \in \{$ 0.61, 0.76, 0.875, 1.03, 1.145, 1.27, 1.38, 1.585, 2.0 $\}$ mm. For the latter width, the condition of having laminar flow and negligible diffusion still holds. In this study, a long time duration, 10 s, is needed to get the full system response (Figs. 63) and to calculate the corresponding performance metrics (Fig. 64). If the channel width is further increased, $R_{\mathrm{Ch}} > 2$ mm, a much longer time duration is required to capture the full response, which is not included in this study. For better visualization, some curves are discarded in Fig. 63. However, they are included in calculating the performance metrics and MSE. Also, only a duration of 3 s is shown when the background flow rate is 20 mL/min.

As expected, a perfect agreement between the analytical and numerical solutions is obtained at small channel widths, $R_{\mathrm{Ch}} \leq 1$ mm, because the tubes are placed in the region where the radial dependency is considered negligible. However, a distinguishable discrepancy is observed upon increasing the channel width, which is translated into higher MSE between the curves in Fig. 65. Keep in mind that the maximum channel width considered in this study still lies about the center axis of the solenoid and relatively far from its inner boundaries, where the discrepancy is supposed to be significant. The MSE depends not only on the channel width but also on the other system parameters. For instance, for the same channel radius and injection parameters, increasing the background flow rate from $Q_{\mathrm{BG}} = 5$ mL/min to $Q_{\mathrm{BG}} = 20$ mL/min reduces the error. Moreover, it improves the performance metrics for the large tubes.

6.4 Single Domain Magnetic Simulation With Solid Laminar Profile

In this method, the parabolic profile derived in subsection 4.1.2 is used to represent the SPIONs. Uniformly distributed particles are assumed to be confined between the inner and outer radii of the laminar profile, whose shape changes with time to imitate the propagation of the SPIONs through the solenoid. Because the system parameters are studied in the previous sections, only the simulation setup is given in this section until a comparison between all the analytical and numerical methods is conducted in section 6.6.

In COMSOL, due to the rotational symmetry of the model, a 2D axisymmetric space dimension is chosen, as shown in Fig. 66. A single domain Magnetic

Fields simulation is used to simulate the susceptometer. At the same time, two similar parametric curves defined by Eq. (88) are used to build the front and back sides of the laminar parabolic profile, which is then converted into solid magnetic material, whose volume susceptibility is defined in Table 3. In order to calculate the system response, the time-dependent coil inductance $L(t)$ is first obtained with a sampling rate of 100 Sa/s. Then, the system response is calculated according to Eq. (104).

6.5 Single Domain Fluidic Simulation With Weighting Function

This method is similar to the full analytical method given in section 6.3, since they both do not consider the magnetic properties of the SPIONs. However, the analytically derived particle density is replaced here by the density obtained directly from a single domain fluidic simulation. Again, in this section, no studies are conducted; only the simulation setup is given.

The simulation setup is similar to the setup employed in the fully numerical method given in section 6.2. However, only the Laminar Flow and Particle Tracing for Fluid Flow are used, while the susceptometer is excluded, as seen in Fig. 67. During the simulation, the positions of the particles that pass through the detection region are exported to MATLAB2019a software in order to calculate their densities weighted by the sensitivity curve of the detector. The system response is estimated according to Eq. (134).

6.6 Comparison of System Responses of All Computational Schemes

This section compares the system responses obtained from the analytical, numerical, and hybrid methods when applying the standard parameters specified in Table 3. The comparison is shown in Fig. 68, which includes the system responses in Fig. 68a and MSE in Fig. 68b. The fully numerical method is considered as a reference.

As mentioned before, the first and third methods use the susceptometer for detection. Therefore, their curves are perfectly matched. Also, due to the stray fields at the solenoid's ends, the signal is detected a bit earlier. On the other hand, the other two methods consider only the sensitivity curve of the susceptometer within its detection region, i.e., ideal detector. Therefore, the peak maximum is slightly amplified.

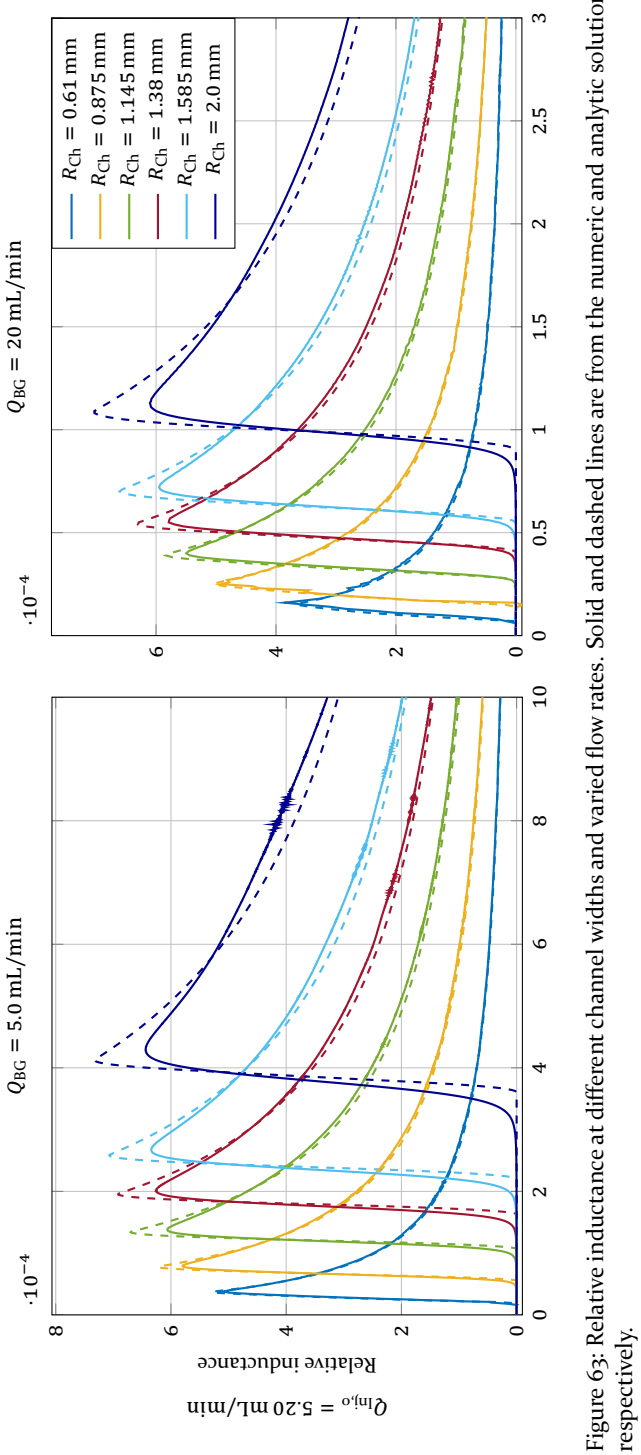

Figure 63: Relative inductance at different channel widths and varied flow rates. Solid and dashed lines are from the numeric and analytic solutions, respectively.

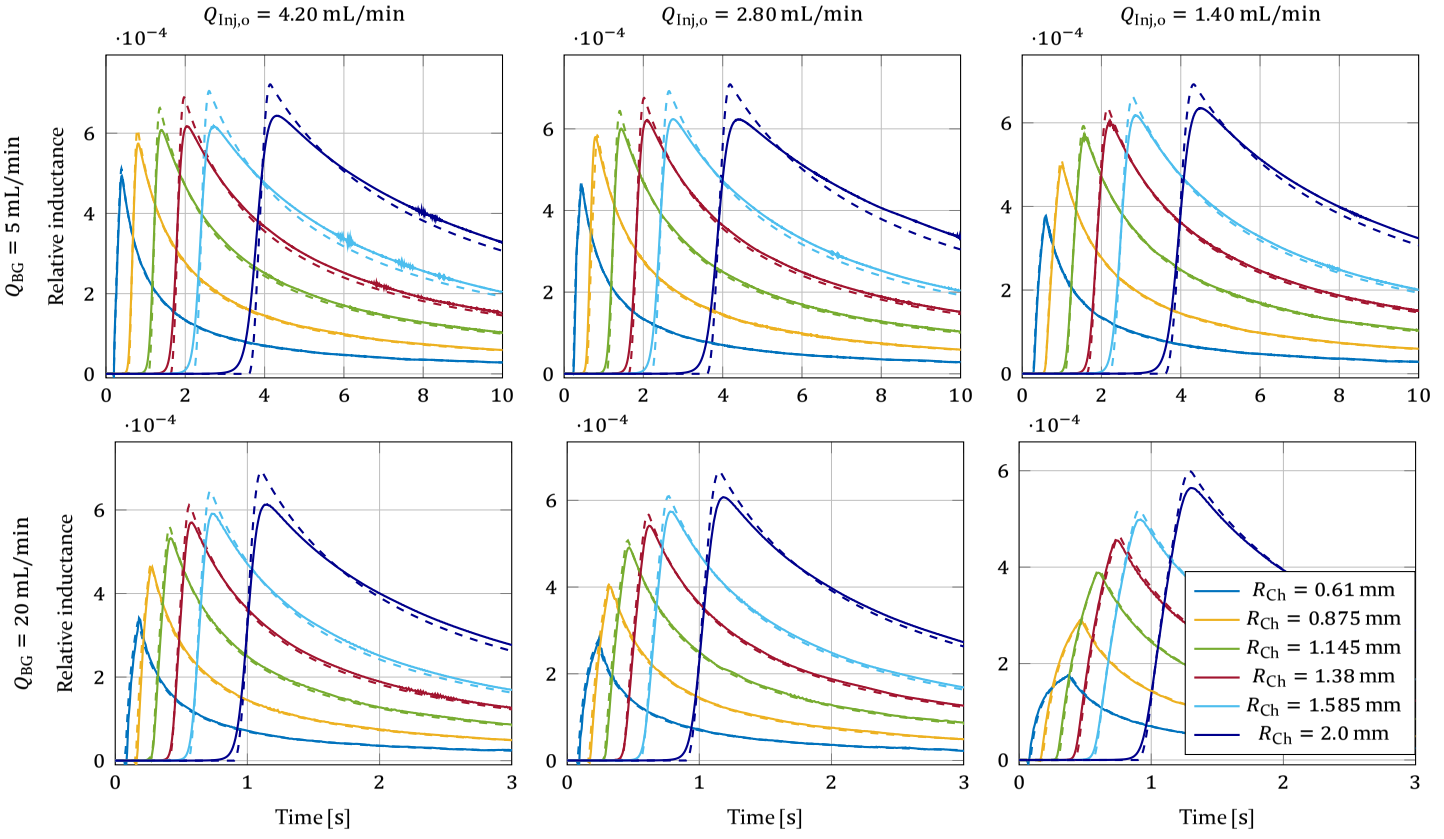

Figure 63: Relative inductance at different channel widths and varied flow rates. Solid and dashed lines are from the numeric and analytic solutions, respectively (cont.).

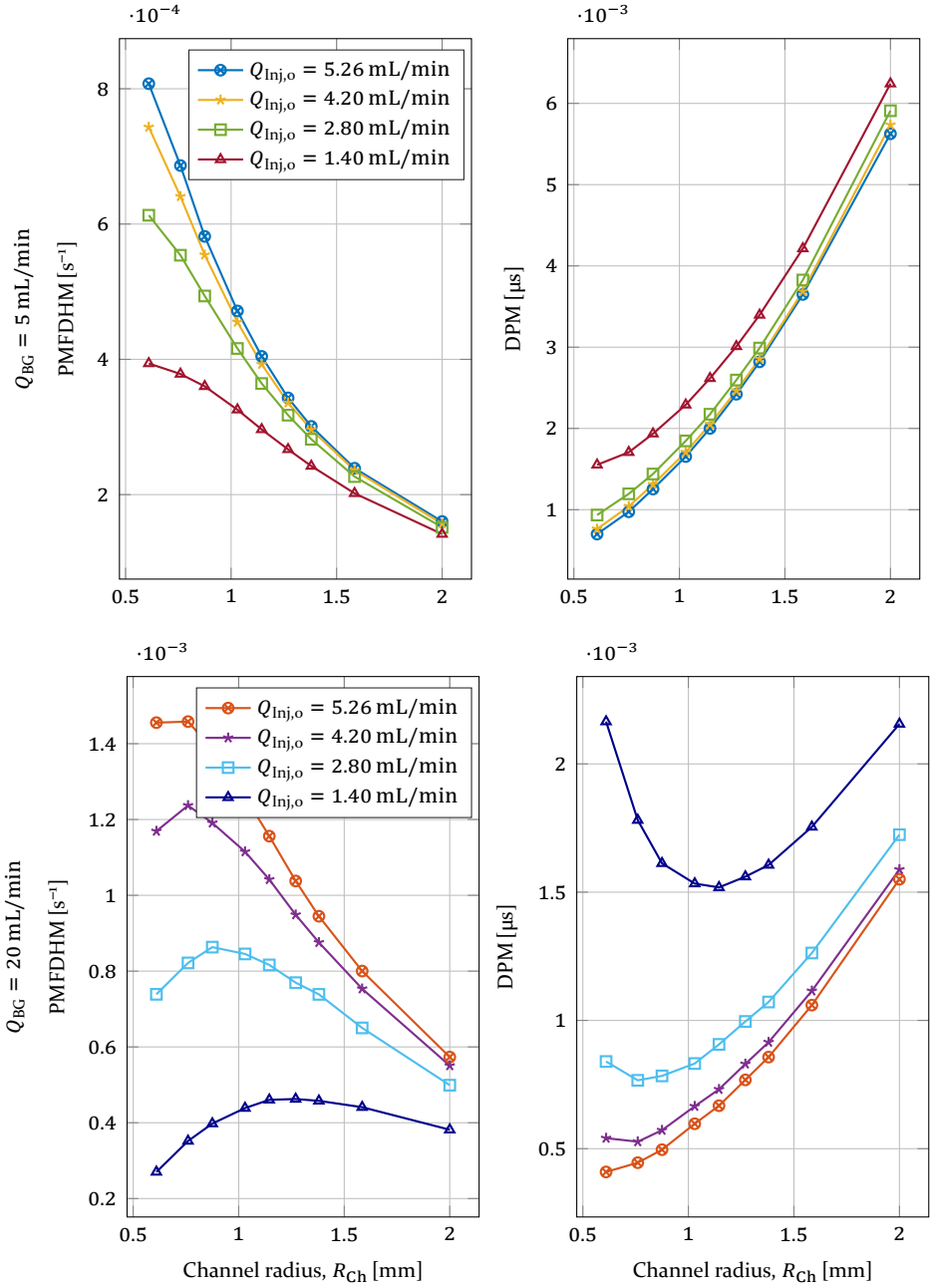

Figure 64: Performance metrics due the propagation of varied flow rates through channels of different widths. Each row represents the results at a different background flow rate Q_{BG}.

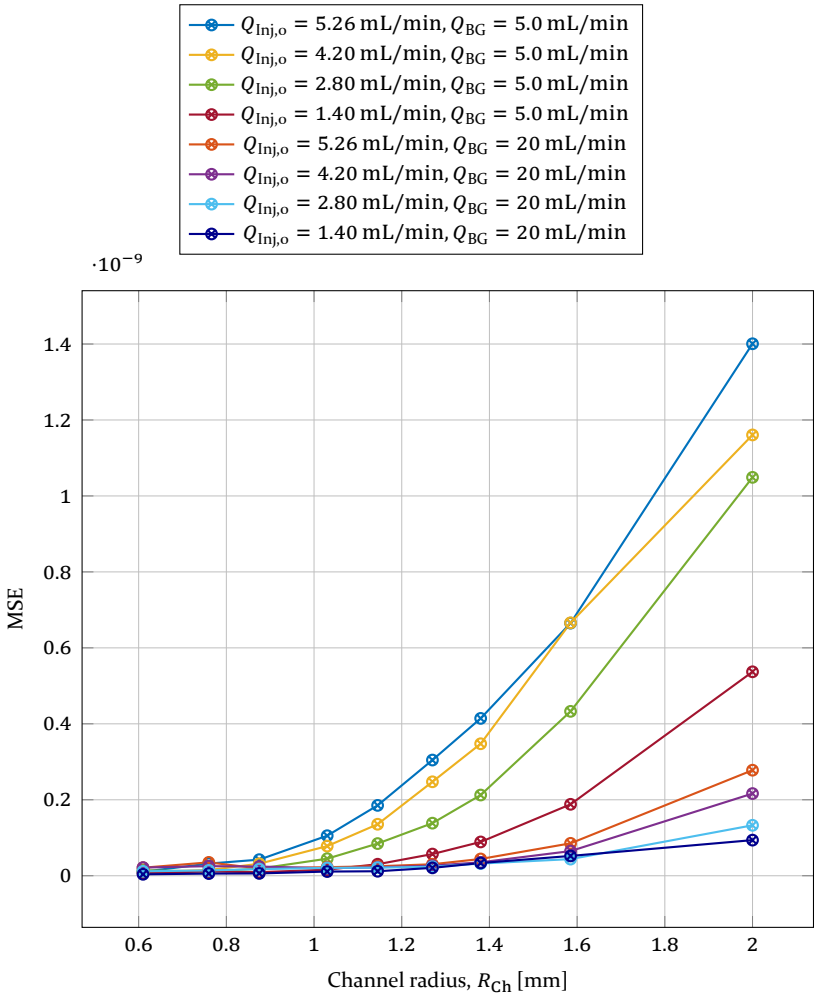

Figure 65: Mean square error between the analytical and numerical solutions when varied flow rates are applied to channels of different widths, $R_{\mathrm{RX}} = L_{\mathrm{RX}} = 5$ mm.

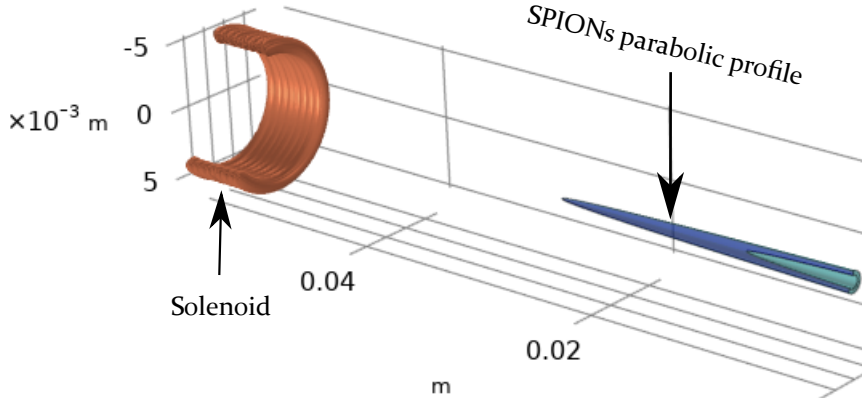

Figure 66: 2D axisymmetric model of the SPIONs parabolic profile goes through the solenoid.

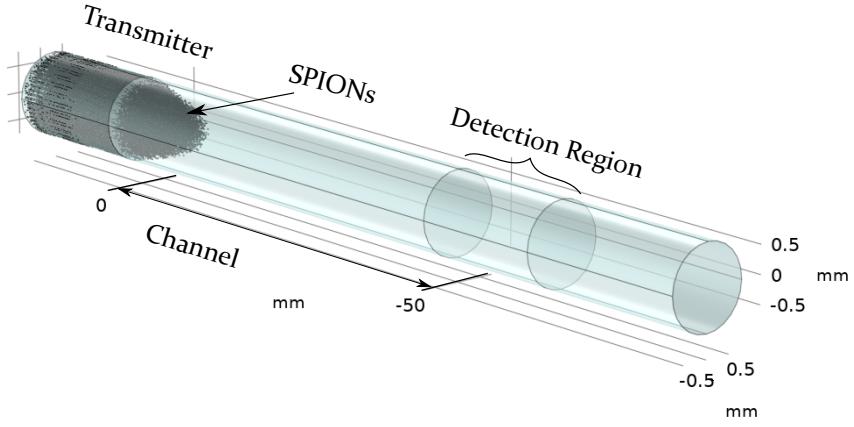

Figure 67: SPIONs are released into the channel and passed through the detection region, where their densities are calculated and weighted by the sensitivity curve of the solenoid to estimate the system response.

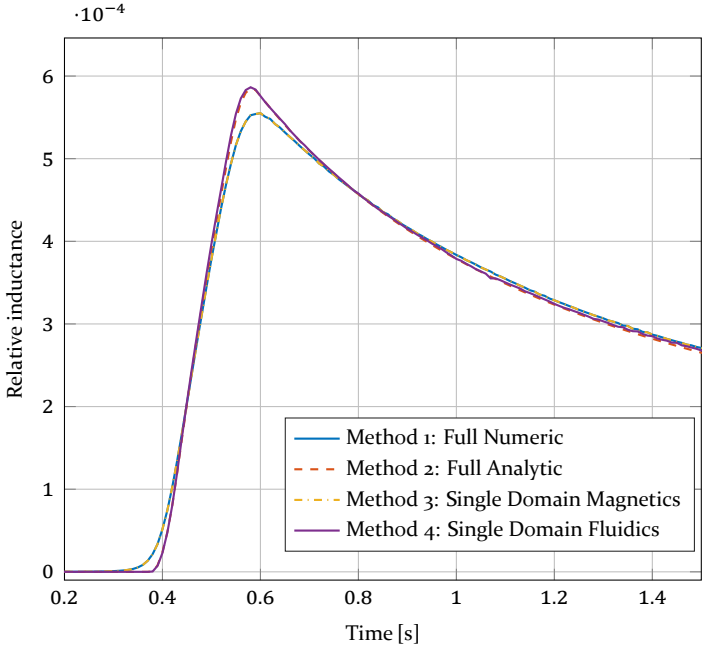

(a) System response

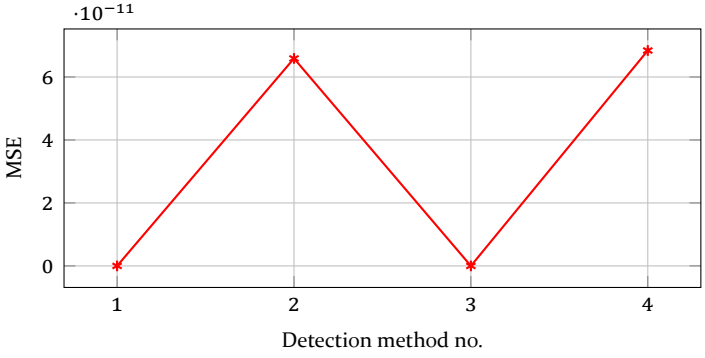

(b) Error Calculation

Figure 68: Comparison between the different computational schemes when the standard setup parameters defined in Table 3 are used.

6.7 Experimental Study

In this section, experiments are conducted, and compared with simulation based on method 4, i.e., the decoupling of the magnetic and fluidic domains.

6.7.1 Experimental Setup

As shown in Fig. 69 (schematic diagram of the testbed is already illustrated in Fig. 8b), SPIONs are dispersed in an aqueous suspension and stored in a syringe connected to the particle tube whose inner radius is 0.4 mm. The injection of the particles into the tube is controlled by a peristaltic pump (Ismatec® Reglo Digital, Germany), which provides pumping actions at different flow rates $Q_{\mathrm{Inj,o}}$ and injection volumes V_{Inj}. The stationary background water flow Q_{BG} in the propagation tube is maintained by a second peristaltic pump (Ismatec® IPC, Germany). Both propagation and background tubes have the same inner radius of 0.76 mm. As mentioned before, the tubes are connected via a Y-connector, and MS2G Bartington® susceptometer coil is used for particle detection.

6.7.2 Simulation Setup

When the Y-connector is added to the model, the rotationally symmetric property is lost, and a 3D domain is required for simulation. However, to reduce the computational complexity, instead of using the susceptometer for particle detection and due to the negligible radial dependency, method 4 is utilized, where the system response is estimated using particle density together with the sensitivity curve of the susceptometer. The same fluidic simulation setup given in subsection 6.5 is applied to obtain the particle density within

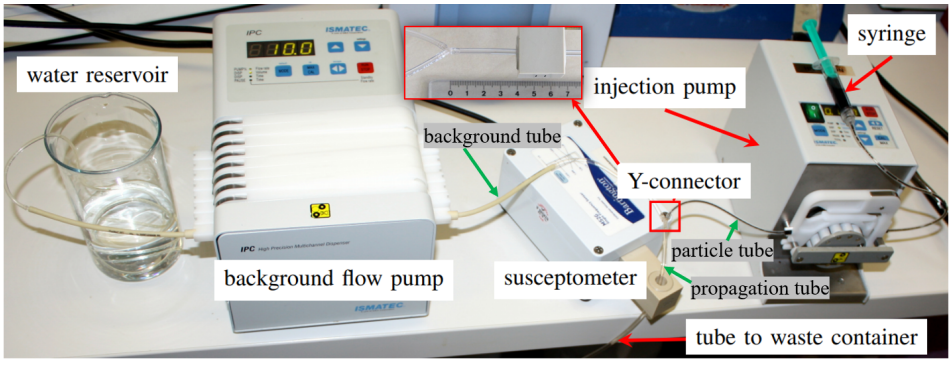

Figure 69: Experimental setup of the SPIONs-based testbed [138].

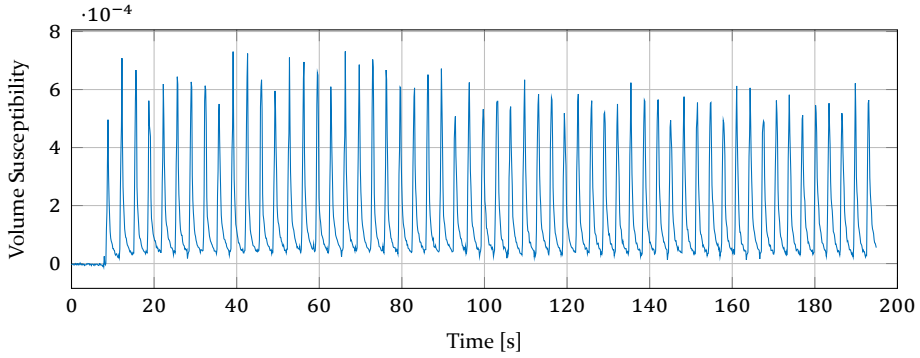

Figure 70: Receiver curves obtained from measurement when the standard setup is applied.

the detection region. Generally, the standard setup given in Table 3 is used unless other parameters are considered in the following subsections.

6.7.3 Agreement of Measurement and Simulation

In this subsection, the obtained system responses from both simulation and measurement are compared for varied flow rates.

In order to obtain the receiver curves from measurement, 100 received pulses are measured with each experiment. A representative plot of the measured susceptibility when the standard setup parameters are applied is shown in Fig. 70. Due to the different positions and distribution of particles within the detector, the height of the detected signal varies. To obtain the average of the pulses to be compared with simulation, a threshold value equals to 50% of the strongest pulse is taken so that the pulses are separated and overlapped. Then, the mean is taken, and its standard deviation is calculated.

The receiver curves from simulation and measurement are synchronized by the use of an optimization strategy. The agreement between the curves is maximized in terms of a least-squares fit $\chi^2(\Delta t, c_\mathrm{m})$, where time-shift Δt and scaling factor c_m are used as free parameters

$$\chi^2(\Delta t, c_\mathrm{m}) = \frac{1}{N_\mathrm{m}} \sum_{i=1}^{N_\mathrm{m}} \left[s_\mathrm{meas}(t_i) - c_\mathrm{m} \cdot s_\mathrm{simul}(t_i - \Delta t) \right]^2 \qquad (140)$$

where N_m denotes the number of measurement values. Time shift Δt is varied in 100 steps in such a way that the maximum of the optimized curve s_simul is shifted from the threshold-crossing of the rising to the falling edge of the measurement curve.

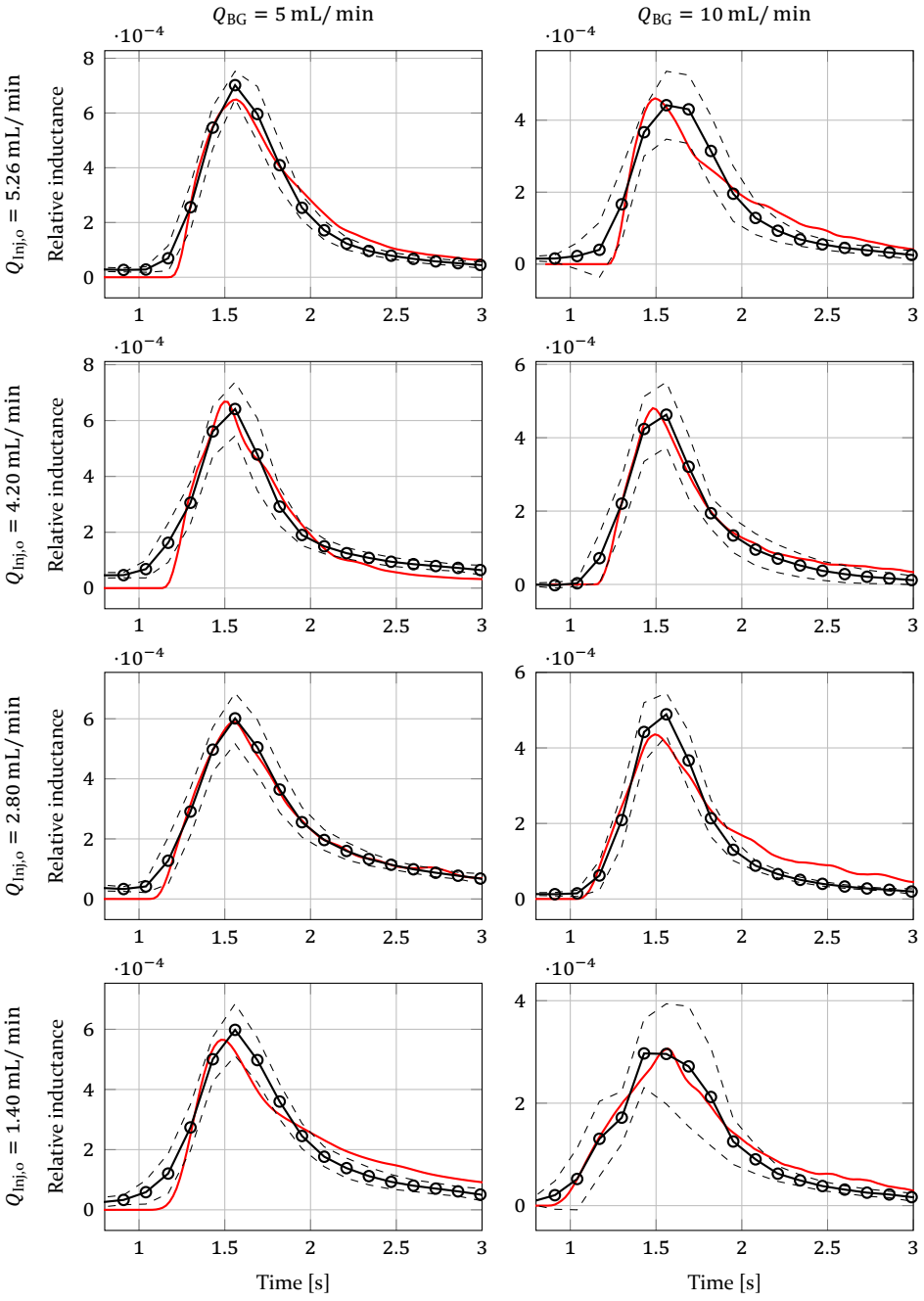

Figure 71: Relative inductance from measurement (solid black), its standard deviation (dashed black), and 3D-simulation (red) at different flow rates.

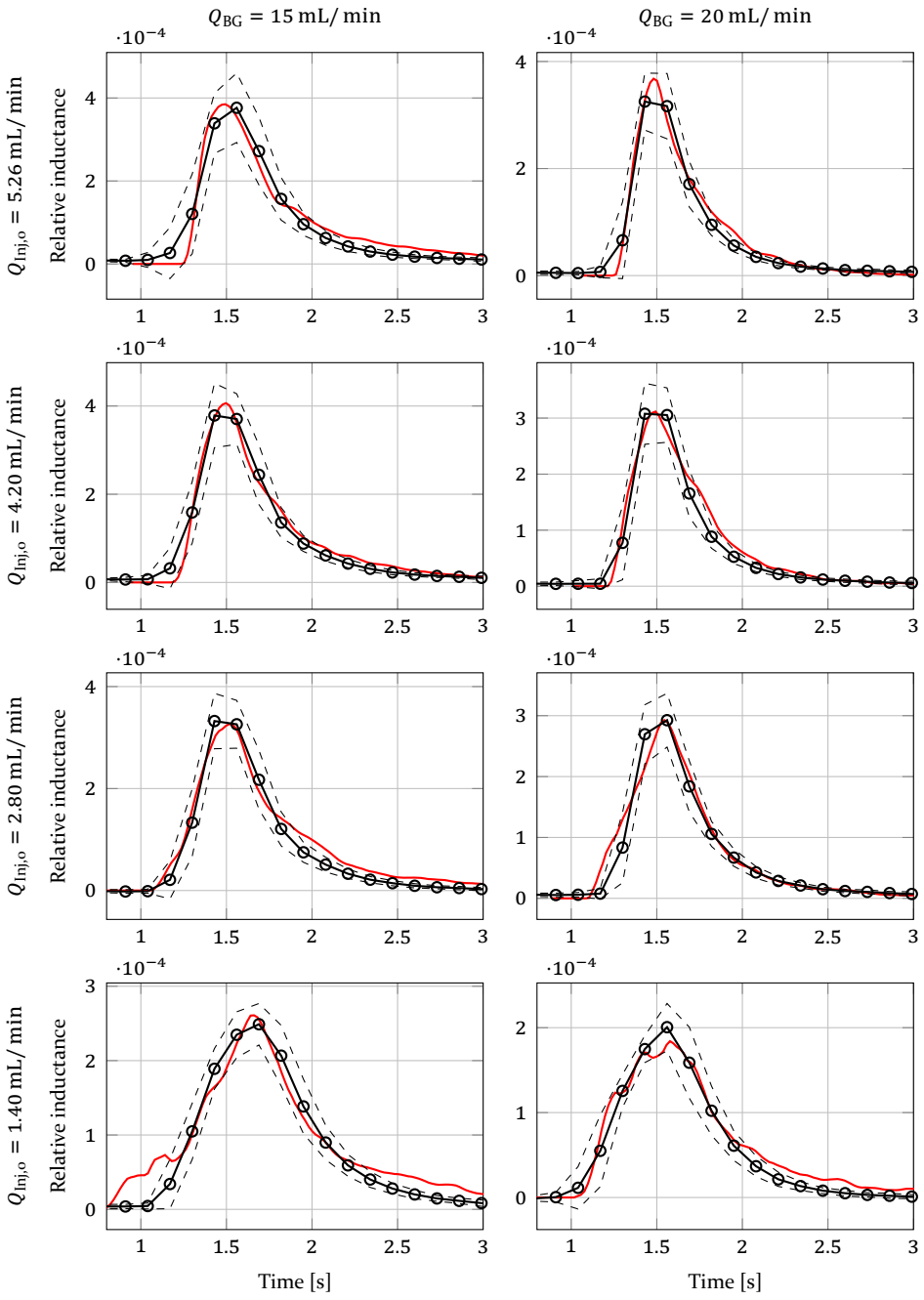

Figure 71: Relative inductance from measurement (solid black), its standard deviation (dashed black), and 3D-simulation (red) at different flow rates (cont.).

The measured susceptibility is compared with the curves of the simulated models in two ways: morphology and performance metrics.

Regarding the morphology, Fig. 71 depicts the system responses from measurement and simulation for varied flow rates. Background flow rate Q_{BG} and particle injection flow rate $Q_{\mathrm{Inj,0}}$ are varied along rows and columns, respectively. The results agree with the findings obtained in subsection 6.3.1.2. It can be seen that the amplitude of the receiver curve decreases with increasing Q_{BG} at low $Q_{\mathrm{Inj,0}}$. This means that, for the same number of particles, the speed of the propagating flow influences the amplitude of the detected signal. Also, the width of the system response is found to mainly depend on the flow in the propagation channel and is minimized with maximum Q_{BG} and $Q_{\mathrm{Inj,0}}$. Narrow pulse width promises less ISI and provides a high transmission rate. For very low $Q_{\mathrm{Inj,0}}$, however, weaker pulses are obtained with relatively large width nearly regardless of Q_{BG}. In the measurements, due to the multiple actions of particle injection, some particles may remain in the channel and contribute to upcoming received signals, i.e., channel with memory. Low flow rates increase this effect and prevent the particles from being washed out, adversely affecting both bit rate and bit error rate.

In Fig. 72, both PMFDHM and DPM of the simulated models are plotted against their counterparts of the measurements for each experiment with a linear regression representation (red line). There is a good correlation between simulation and measurement regarding the PMFDHM, giving R^2-value of 0.77. Also, because of the applied synchronization strategy, a perfect correlation between the measurement and simulation is shown regarding the DPM, R^2-value of 0.96.

The discrepancy between measurement and simulation can be due to the following assumptions: straight and memoryless channel, homogeneous magnetic field, and ideal detector; in addition to the pumps tolerances and injection functions; as well as the threshold taken to average over the measured pulses.

6.7.4 Particle Distribution Shortly After Y-connector

After the verification of the 3D-simulated model by experiments in the previous section, simulation is further employed in this subsection to obtain the particle density at the beginning of the propagation channel, directly after the Y-connector, which can be considered the distribution of particles being injected into the channel. The simulation allows a complex distribution due to the confluence of background and injection flows. The particle density is

obtained at time $t = 0.1$ s for a slice of thickness 3 mm taken from the propagation tube directly after the Y-connector. The cross-sectional area of the channel is subdivided into $X = 30$ radial and $Y = 30$ angular compartments according to the description given in section 4.2.1.

As shown in Fig. 73, the particle distribution is examined by simulation (Fig. 73a) and measurement (Fig. 73b) when the standard setup is applied, while the cross-sectional particle density is depicted in Fig. 73c. Rather than mixing, the background and injection flows stay separated from each other and move parallel to one another. The lower side of the cross-section is empty of particles, which are concentrated on the other side of the tube.

In order to investigate the particle distribution as a function of the tube radius and azimuth, respectively, the estimated radial $R(r)$ and angular $A(\varphi)$ components of the particle density are smoothed in MATLAB2019a and plotted in Fig. 74. The components are shown in Fig. 74a for a fixed injection flow rate of $Q_{\mathrm{Inj,o}} = 5.26\,\mathrm{mL/min}$ with varied background flow rates, and in Fig. 74b when the particles are injected with varied flow rates into a channel of a fixed background flow rate of $Q_{\mathrm{BG}} = 20\,\mathrm{mL/min}$.

For all flow configurations, due to the Y-connector, the particles are distributed only on one side of the tube in contact with its inner boundary, $0 \leq \varphi \leq \pi$ rad, where they are injected into the channel. The relatively large background flow, i.e., $Q_{\mathrm{BG}} > Q_{\mathrm{Inj,o}}$, pushes the particles away from the center of the tube, and hence it covers a larger part of the cross-section than the injected particles. When the injection flow rate is reduced, the pushing becomes more pronounced, and particle density significantly decreases, as depicted in Fig. 74b. Pushing the particles towards the inner boundary of the tube, where the velocity is considerably lower than at the tube center, leading to a long transmission time. This explains the long tail introduced to the curves shown in Fig. 71. Using the Y-connector is close to or imitates the scenario given in section 6.2.2.1, where the particles are injected from the boundary-ring.

To validate the model given in section 4.2.1, the 2D estimated particle density matrix $\nu(r, \varphi)$ defined by Eq. (101) is obtained for all the trials considered in Fig. 71 and compared with the actual density matrix $\mathrm{P}_0(r, \varphi)$ extracted directly from the FEM simulated model. The corresponding values are plotted in Fig. 75 with a linear regression representation (red line).

The results show a good correlation between both models with R^2-value of 0.83, which ensures the validation of the model.

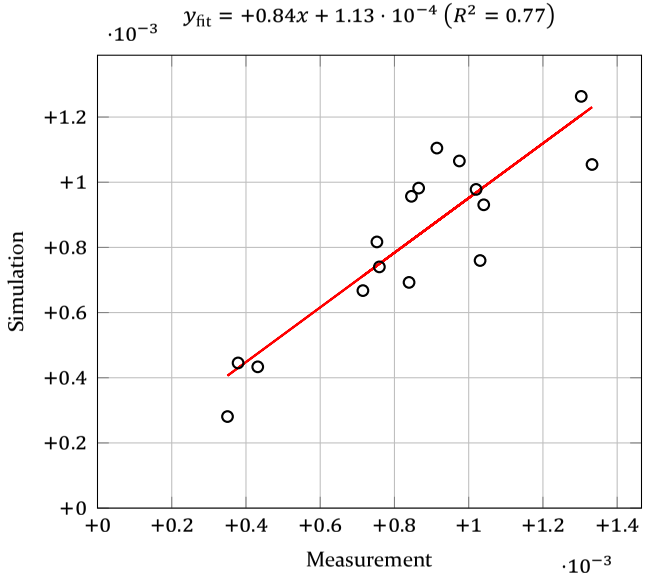

(a) PMFDHM [s^{-1}].

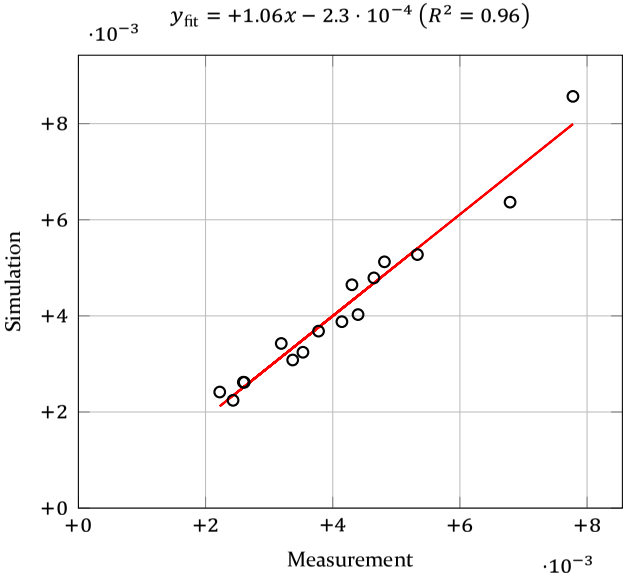

(b) DPM [µs].

Figure 72: Performance metrics comparison between measurement data and simulated curves.

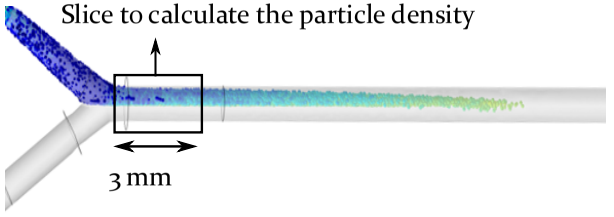

(a) Simulation

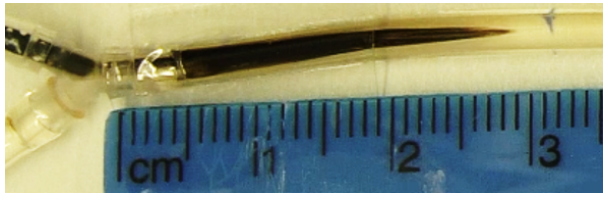

(b) Experiment

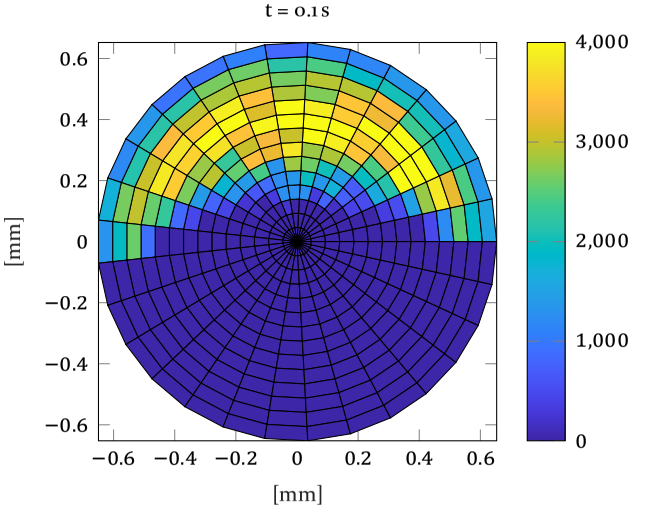

(c) Cross-sectional particle density

Figure 73: Particle distribution after the Y-connector derived from the simulation and measurement when the standard setup is applied.

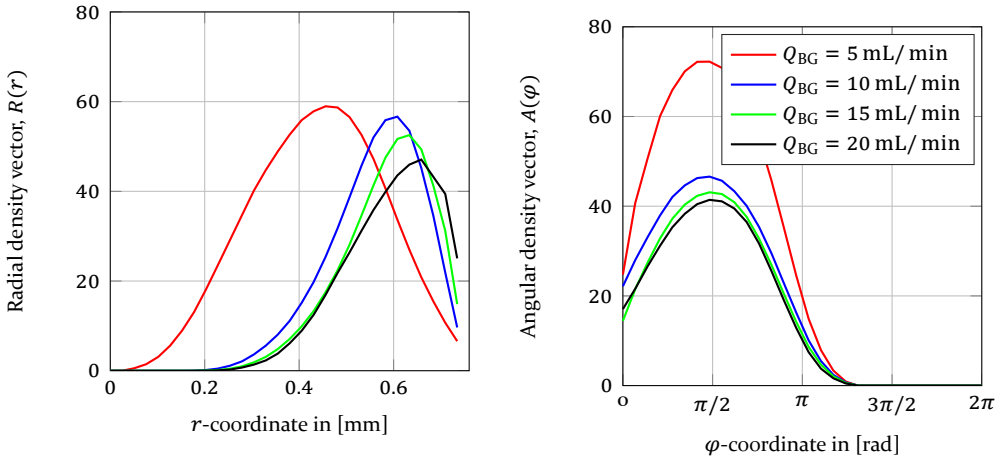

(a) Fixed injection flow rate of $Q_{\text{Inj,o}} = 5.26\,\text{mL/ min}$.

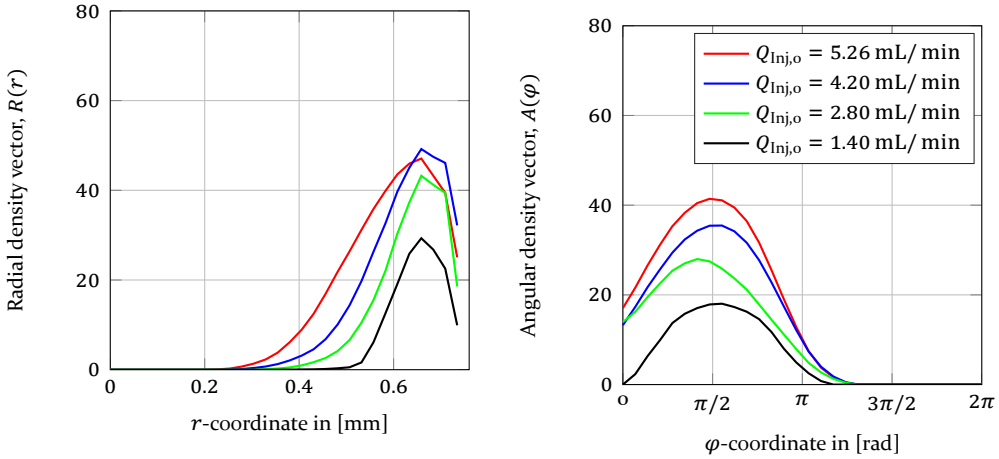

(b) Fixed background flow rate of $Q_{\text{BG}} = 20\,\text{mL/ min}$.

Figure 74: Radial and angular components of the cross-sectional particle density 3 mm after the Y-connector at time $t = 0.1\,\text{s}$ for varied background and injection flow rates.

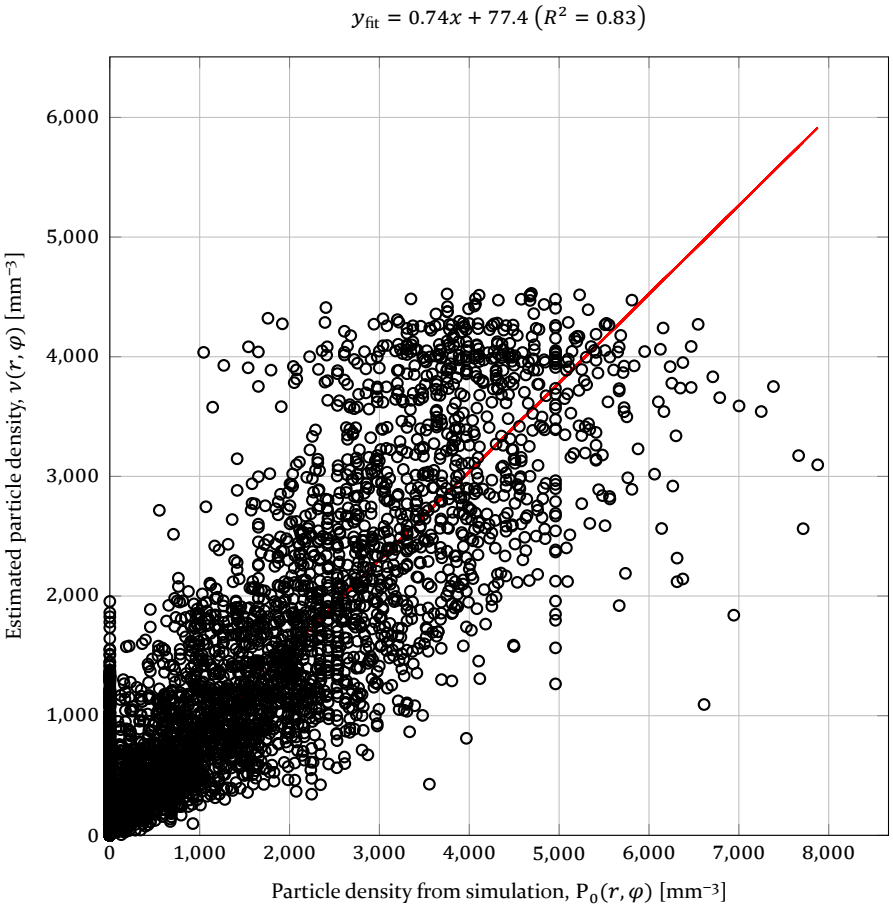

Figure 75: Linear regression relation between the estimated and exact particle density matrices for a slice of thickness 3 mm after the Y-connector at time $t = 0.1$ s for all the trials given in Fig. 71.

7 Guidelines for System Design

This chapter summarizes most of the important findings from previous chapters and provides a catalog of design guidelines that should be followed at the transmitter, channel and receiver to optimize the system response. The improvement or degradation stated below about the system response is decided according to the performance metrics given in section 6.1.2.

7.1 Transmitter

- Changing the initial distribution and position of the injected particles highly affects the system response. The injection directly at the tube center weakens the detected signal but reduces the time delay. Whereas the injection near its inner boundary elongates the system response and hence degrades the performance metrics. A compromise choice is to inject the particles at a region between the center of the tube and its inner boundary, see section 6.2.2.1.
- The injection volume, flow rate, and background velocity are three interconnected parameters that highly affect the system response. They must be chosen in line with the other system parameters such that the transmitter length becomes short relative to the lengths of both the channel and receiver, see section 6.3.1.
- Increasing the injected volume of the SPIONs suspension at relatively high background and injection flow rates improves the system response. However, injecting a large volume of particle suspension with a very low flow rate into a channel of a very high background flow rate significantly degrade the performance metrics, see section 6.3.1.
- For a very long injection duration, the signal takes a relatively long time to reach its maximum peak; hence, a wide pulse is detected that slows down the system and may degrade the performance. It is recommended that the injection ends before or, if not possible, shortly after the particles enter the detector, see section 6.3.1.
- Due to the Y-connector, the background and injection flow rates do not mix; instead, they move parallel to one another, and particles are confined to one side of the propagation tube. Increasing the background flow rate pushes the particles away from the tube center, particularly when the injection flow rate is reduced, see section 6.7.4.

- If the radial dependency is negligible, a single domain 3D-simulation-based model of the testbed that employs the Y-connector can be used together with the sensitivity curve of the susceptometer along its center axis to estimate the system response, see section 6.5. Otherwise, the 3D distribution of solenoid's field in its inner domain is needed, see section 4.3.2.2.

7.2 Channel

- In small tubes with relatively low flow rates, Laminar flow with a parabolic velocity profile is considered, and particles' diffusion can be neglected, see section 4.1.1.
- When the particles are released into large channels of retaively low flow rates, high signal amplitudes can be obtained if the strong magnetic field near the inner boundary of the solenoid compensates for the reduction in the particle density. However, the time delay and pulse width accordingly increase, degrading the overall system performance, see section 6.2.3.2.
- To speed up the system in case of wide tubes, high background flow rates can be a reasonable solution. However, turbulence should be taken into consideration, see section 6.3.1.3.
- As the transmission distance increases, considerable signal attenuation, dispersion, and delay are observed, see section 6.2.3.1.
- When the particles are injected into a channel of a very high background flow rate, they are distributed along large volume in the propagation tube which reduces their density and weakens the detected signal, see section 6.3.1.2.

7.3 Receiver

7.3.1 Cylindrical Coils

- Changing the particle distribution inside the inner domain of the coils significantly affects the detected signal. However, if the size of a propagation tube, placed axially along the center axis of the solenoid, is much smaller than its cross-sectional area such that the field is considered homogeneous, any change in the radial positions of particles will not significantly contribute to the detected signal, see section 5.1.3.5.

- The sensitivity near the inner boundary of all cylindrical coils is much higher than that about the center axis. Any small movement of particles near the coil's inner boundaries significantly affect its detected signal. Hence, adaptive threshold might be needed for decoding, especially for short solenoids, see section 5.1.2.
- The radial movement of a SPIONs-filled cylinder of fixed density inside the coil towards its inner boundary increases the detected signal in an exponential manner, which is directly proportional to the field distribution in the same direction, see section 5.1.2.
- The detected signal of the coil is directly proportional to the volume susceptibility (density) of the particle suspension in its detection region. This finding can help adjusting the amount of drugs delivered to the infected cells. For instance, when a large volume of particle suspension (covered with drugs) is injected into the bloodstream, strong signal should be detected, which is corresponding to an intensive dose of drugs and vice versa, see section 4.3.2.2.
- Because the magnetic field of the coil is not limited to its physical length, signals are detected before the particles enter its inner domain. This phenomena may cause interference if there are other magnetic materials nearby. However, the non-homogeneous effect (stray fields) at both ends of the coil is mitigated in long solenoids, see section 5.1.2.
- The stray fields at both ends of the coil is higher than those along its outer boundary, where the field is relatively weak and can be neglected, see section 5.1.2 and section 5.1.3.8.
- Due to the rotational symmetry, the change in inductance caused by a SPIONs-filled cylinder placed inside the coil is equivalent to that caused by a summation of ring-cylinders that form the cylinder. This means that changes in inductance due to partial volumes are additive in radial direction, which is not the case in the axial direction, see section 5.1.3.4 and section 5.1.3.3.
- To fully capture the transmitted data and improve the system response, the receiver is recommended to be of comparable length to the transmitter. Much longer or shorter receivers reduce the performance metrics. Also, it is recommended to have a solenoid of small cross-sectional area (fits perfectly to the tube) so that the particles propagate directly next to its inner boundary, where the magnetic field is maximum, see section 6.2.4.

- In a multi-layer solenoid, adding more layers to the solenoid (that increases its thickness) slightly enlarges its average cross-sectional area and hence reduces the detected signal, see section 6.2.4.3.
- The system response can be mainly obtained either directly from the detector (simulation or measurement) or estimated analytically using its sensitivity curve when the particle distribution in the detection region is known. However, the estimated system response is slightly narrower than that obtained directly from the detector, see section 6.6.
- For the same length, the magnetic field of the Maxwell coil decays outside the detection region faster than Helmholtz, see section 5.1.2.
- Despite of the large homogeneous regions that exist in Helmholtz and Maxwell coils about their center axes, the homogeneity is entirely lost near their inner boundaries and magnetic fields fluctuate due to the contribution from their own individual coils, see section 5.1.2.

7.3.2 Planar Coils

- Moving vertically above the surface of a planar coil shows prominent decay in the detected signal, i.e. double distance weakens the signal almost by half, see section 5.2.2.
- Both square and circular planar coils which are centered on the xy-plane have symmetric magnetic field distribution about the z-axis, see section 5.2.2.
- The fields of the planar coils are almost confined to a small region above their surfaces, see section 5.2.2.
- The system response due to a rectangular planar coil is weaker and wider than that obtained from a square coil whose side length equals the width of the rectangle, see section 5.2.2.
- Introducing an inner aperture to the planar coil weakens its detected signal, see section 5.2.3.3.
- Distributing planar coils around the propagation tube, rather than using a single-sided coil, can help strengthen the detected signal, see section 5.2.3.2.
- Circular planar coil shows superiority over the square and rectangular coils. However, its detected signal is still much weaker than that

obtained from a solenoid of the same detection length and wire-turns, see section 5.2.3.1.

- For On-chip MC applications using SPIONs, an array of planar coils with apertures can be used, which imitates a cylindrical coil and hence provides higher detected signal in comparison with a single planar coil. The array of coils can be embedded into a PCB such that each coil is integrated between two successive layers, while the propagation tube passes through the aperture, see section 5.2.3.3.

8 Conclusion and Outlook

8.1 Conclusion

Molecular communication (MC) uses molecules or synthesized particles to carry information from transmitter to receiver. Over the past years, MC system has been extensively theoretically studied in the literature. Also, several experimental platforms and simulators were lately proposed. Most of those studies were surveyed in this manuscript. However, this work is based on a platform that employs biocompatible Superparamagnetic Iron Oxide Nanoparticles (SPIONs) as information carriers that propagate through a fluidic channel and detected by a susceptometer, i.e., solenoid. The related magnetic and fluidic fundamentals are discussed. In addition, an analytical solution is given to estimate the system response due to the particle propagation inside the inner domain of the susceptometer. The solution involves the volume or line integral of the particle density weighted by the magnetic field strength inside the detection region of the solenoid. This solution efficiently estimates the detection regime of the susceptometer, which reduces the computationally expensive simulations and tedious experiments. According to the best of the author's knowledge, this derivation has not been given in any publications before. Other detectors, namely cylindrical and planar coils, are also analytically and numerically studied then compared with the solenoid. To gain an insight into their detection mechanism, various distribution, positions, and trajectories of particles within their detection regions are applied.

In general, the system response can be estimated either analytically as discussed above or directly from the detector using simulation and/or measurements. In an entirely numeric study, the SPIONs-based platform is approximated by a 2D-axisymmetric model to investigate how changing its injection, fluid flow, and geometrical parameters affect the system response. This model is also used to verify the analytical solution. Another 3D simulation-based model of the employed platform is built to export the time-dependent particle density inside the detector during propagation, to be substituted into the analytical solution to estimate the system response. The simulations are compared with the conducted experiments.

Some of the findings are concluded as follows. The receiver is preferred to be of comparable length to the transmitter with its inner boundary in direct contact with the propagation tube. Although the propagation through a wide channel strengthens the detected signal because the propagating particles are shifted towards the inner border of the coil, where the field is high, the

average propagating velocity is reduced, which widens the pulse and reduces the overall system performance. Also, the injection is recommended to end before, or at most shortly after, the particles enter the detection region. Before being injected into the channel, the particle distribution within the transmitter highly affects the detected signal. Other design guidelines are collected in Chapter 7.

8.2 Outlook

Molecular communication using SPIONs is still in its initial phase and deep research is needed.

As a future work, we suggest the following

- Other pumps, e.g., micropumps, with different injection functions should be employed and compared.
- Variation of fluids rather than water, such as oil or blood, is required to study how the viscosity affects the system response.
- Check for turbulence when adding obstacles to the channel, which imitate clots in the bloodstream, or when the tube is bent.
- Change the injection angle by building new pieces with different angles rather than the standard Y-connector.
- Because of the nanoscale of the employed particles, the effect of gravity is neglected in this manuscript. However, other particles with larger diameters and masses are needed to be studies to check their impact on the system response.
- Apply sufficiently long transmission distances and check how this affects the particle diffusion.
- To steer the particles to a particular direction (or location) for targeted drug delivery, electromagnets of high field gradient are needed to be optimized.
- For industry applications, larger tubes with high flow rates can be employed. However, turbulence should then be taken into consideration.
- The extension of this Single-Input Single-Output (SISO) system into MIMO to achieve high bit rate transmission.

- Planar coils are promising alternatives to the solenoids if the detector is placed on the body. Therefore, a deep study of their working mechanism and design is recommended. One of the suggested designs is the folding and bending planar coils that fit the shape of the surface on which they are placed.
- In all of these studies, very low frequency is assumed, and hence only Direct Current (DC) analysis is conducted. However, the models can be extended to include the AC analysis.
- Finally, building an experimental platform that involves both HBC and MC communication systems.

List of Published Work

1. D. Ahmed, J. Kirchner, and G. Fischer, "Signal Transmission with Intra-Body and Inter-Body Communications: Simulation-Based Models", *13th EAI International Conference on Body Area Networks*, Springer International Publishing, 2020

2. A. Thalmayer, S. Zeising, D. Ahmed, G. Fischer, and J. Kirchner, "*Particle Steering In Magnetic Drug Targeting: A Simple Comsol Model*", *COMSOL Conference*, Online, 2020.

3. S. Zeising, J. Kirchner, H. F. Khalili, D. Ahmed, M. Lübke , A. Thalmayer, and G. Fischer, "Towards Realisation of a Non-Invasive Blood Glucose Sensor Using Microstripline", *International Instrumentation and Measurement Technology Conference (I2MTC)*, Dubrovnik, 2020.

4. D. Ahmed, H. Unterweger, G. Fischer, R. Schober, and J. Kirchner, "Characterization of an Inductance-based Detector in Molecular Communication Testbed Based on Superparamagnetic Iron Oxide Nanoparticles", *IEEE SENSORS Conference*, Montréal, Canada, 2019.

5. D. Ahmed, G. Fischer, and J. Kirchner, "Simulation-based Models of the Galvanic Coupling Intra-body Communication", *2019 IEEE Sensors Applications Symposium*, Sophia Antipolis, France, 2019.

6. M. Bartunik, M. Lübke, H. Unterweger, C. Alexiou, S. Meyer, D. Ahmed, G. Fischer, W. Wicke, V. J. Kooshkghazi, R. Schober, and J. Kirchner, "Novel Receiver for Superparamagnetic Iron Oxide Nanoparticles in a Molecular Communication Setting", *6th ACM International Conference on Nanoscale Computing and Communication (NANOCOM)*, Dublin, 2019.

7. N. Schlechtweg, S. Meyer, H. Unterweger, M. Bartunik, D. Ahmed, W. Wicke, V. J. Kooshkghazi, C. Alexiou, G. Fischer, R. Weigel, R. Schober, and J. Kirchner, "Magnetic Steering of Superparamagnetic Nanoparticles in Duct Flow for Molecular Communication: A Feasibility Study", *14th EAI International Conference on Body Area Networks*, BodyNets, Florence, 2019.

8. H. Unterweger, J. Kirchner, W. Wicke, A. Ahmadzadeh, D. Ahmed, V. J. Kooshkghazi, C. Alexiou, G. Fischer, R. Weigel, and R. Schober, "Experimental Molecular Communication Testbed Based on Magnetic Nanoparticles in Duct Flow", *19th IEEE International Workshop on Signal*

Processing Advances in Wireless Communications, Kalamata, Greece, 2019.

9. D. Ahmed, J. Kirchner and G. Fischer, "Wave Propagation with Human Body Communications in BANs", *IEEE MTT-S International Conference (NEMO)*, Seville, Spain, 2017.
10. D. Ahmed, J. Kirchner and G. Fischer,"Wave Propagation with HBC in a Human Arm Model", *IEEE International Symposium on Medical Measurements and Applications (MeMeA)*, Rochester, 2017.

Bibliography

[1] M. Abbaszadeh, I. U. Atthanayake, P. J. Thomas, and W. Guo. "Molecular Signal Tracking and Detection Methods in Fluid Dynamic Channels." In: *IEEE Transactions on Molecular, Biological and Multi-Scale Communications* 6.2 (2020), pp. 151–159.

[2] M. Abbaszadeh, W. Li, L. Lin, I. White, P. Denissenko, P. J. Thomas, and W. Guo. "Mutual Information and Noise Distributions of Molecular Signals Using Laser Induced Fluorescence." In: *2019 IEEE Global Communications Conference (GLOBECOM)* (2019), pp. 1–6.

[3] D. Ahmed, G. Fischer, and J. Kirchner. "Simulation-based Models of the Galvanic Coupling Intra-body Communication." In: *2019 IEEE Sensors Applications Symposium (SAS)* (2019), pp. 1–6.

[4] D. Ahmed, H. Unterweger, G. Fischer, R. Schober, and J. Kirchner. "Characterization of an Inductance-based Detector in Molecular Communication Testbed Based on Superparamagnetic Iron Oxide Nanoparticles." In: *IEEE SENSORS* (2019), pp. 1–4.

[5] D. Ahmed, J. Kirchner, and G. Fischer. "Signal Transmission with Intra-Body and Inter-Body Communications: Simulation-Based Models." In: *13th EAI International Conference on Body Area Networks* (2020), pp. 171–184.

[6] B. Akdeniz, A. Pusane, and T. Tugcu. "Position-based Modulation in Molecular Communications." In: *Nano Communication Networks* 16 (2018).

[7] A. Akkaya and T. Tugcu. "DMCS: Distributed Molecular Communication Simulator." In: *Proceedings of the 8th International Conference on Body Area Networks*. BodyNets '13 (2013), pp. 468–471.

[8] I. F. Akyildiz, F. Fekri, R. Sivakumar, C. R. Forest, and B. K. Hammer. "Monaco: Fundamentals of Molecular Nano-communication Networks." In: *IEEE Wireless Communications* 19.5 (2012), pp. 12–18.

[9] I. F. Akyildiz, M. Pierobon, S. Balasubramaniam, and Y. Koucheryavy. "The internet of Bio-Nano things." In: *IEEE Communications Magazine* 53.3 (2015), pp. 32–40.

[10] I. Akyildiz, F. Brunetti, and C. Blázquez. "Nanonetworks: A New Communication Paradigm." In: *Computer Networks* 52 (2008), pp. 2260–2279.

[11] I. F. Akyildiz, J. M. Jornet, and M. Pierobon. "Nanonetworks: A New Frontier in Communications." In: *Commun. ACM* 54.11 (2011), pp. 84–89.

[12] B. Alberts. *Molecular Biology of the Cell*. 6. ed. Garland Science, 2015.

[13] B. Atakan, S. Galmes, and O. B. Akan. "Nanoscale Communication With Molecular Arrays in Nanonetworks." In: *IEEE Transactions on NanoBioscience* 11.2 (2012), pp. 149–160.

[14] I. Atthanayake, S. Esfahani, P. Denissenko, I. Guymer, P. J. Thomas, and W. Guo. "Experimental Molecular Communications in Obstacle Rich Fluids." In: *Proceedings of the 5th ACM International Conference on Nanoscale Computing and Communication*. NANOCOM '18 (2018), pp. 1–2.

[15] C. Austin, D. Caro, S. Sankar, W. Penniman, J. Perdomo, L. Hu, S. Patel, X. Gu, S. Watve, B. Hammer, and C. Forest. "Porous Monolith Microfluidics for Bacterial Cell-to-Cell Communication Assays." In: *Biomicrofluidics* 11 (2017), pp. 1–11.

[16] C. Austin, W. Stoy, P. Su, M. Harber, J. P. Bardill, B. Hammer, and C. Forest. "Modeling and Validation of Autoinducer-Mediated Bacterial Gene Expression in Microfluidic Environments." In: *Biomicrofluidics* 8 (2014), pp. 1–10.

[17] R. Bala and A. Marwaha. "Investigation of Graphene Based Miniaturized Terahertz Antenna For Novel Substrate Materials." In: *Engineering Science and Technology, an International Journal* 19.1 (2016), pp. 531–537.

[18] S. Balasubramaniam and P. Lio. "Multi-Hop Conjugation Based Bacteria Nanonetworks." In: *IEEE Transactions on NanoBioscience* 12.1 (2013), pp. 47–59.

[19] M. Bartunik, M. Fleischer, W. Haselmayr, and J. Kirchner. "Colour-Specific Microfluidic Droplet Detection for Molecular Communication." In: *Proceedings of the 7th ACM International Conference on Nanoscale Computing and Communication*. NanoCom '20 (2020), pp. 1–6.

[20] M. Bartunik, M. Lübke, H. Unterweger, C. Alexiou, S. Meyer, D. Ahmed, G. Fischer, W. Wicke, V. Jamali Kooshkghazi, R. Schober, and J. Kirchner. "Novel Receiver for Superparamagnetic Iron Oxide Nanoparticles in a Molecular Communication Setting." In: *Proceedings of the 6th ACM International Conference on Nanoscale Computing and Communication, NANOCOM 2019* (2019).

[21] M. Bartunik, H. Unterweger, C. Alexiou, R. Schober, M. Lübke, G. Fischer, and J. Kirchner. "Comparative Evaluation of a New Sensor for Superparamagnetic Iron Oxide Nanoparticles in a Molecular Communication Setting." In: *Bio-inspired Information and Communication Technologies* (2020), pp. 303–316.

[22] M. Biletic, F. H. Juwono, and L. Gopal. "Nanonetworks and Molecular Communications for Biomedical Applications." In: *IEEE Potentials* 39.3 (2020), pp. 25–30.

[23] Bloomer. *Practical Fluid Mechanics For Engineering Applications*. 1st ed. Mechanical engineering 124. Marcel Dekker, 2000.

[24] G. V. Brown and L. Flax. "Superposition of Semi-Infinite Solenoids for Calculating Magnetic Fields of Thick Solenoids." In: *Journal of Applied Physics* 35 (1964), pp. 1764–1767.

[25] S. F. Bush. *Nanoscale Communication Networks (Nanoscale Science and Engineering)*. 1st ed. Artech House, 2010.

[26] Callister. *Fundamentals of Materials Science and Engineering*. 5th ed. John Willey and Sons, 2001.

[27] Y. Cengel and J. M. Cimbala. *Fluid Mechanics: Fundamentals and Applications*. 1st ed. McGraw-Hill Science/Engineering/Math, 2006.

[28] O. A. Dambri and S. Cherkaoui. "Performance Enhancement of Diffusion-Based Molecular Communication." In: *IEEE Transactions on NanoBioscience* 19.1 (2020), pp. 48–58.

[29] Y. Deng, A. Noel, M. Elkashlan, A. Nallanathan, and K. C. Cheung. "Modeling and Simulation of Molecular Communication Systems With a Reversible Adsorption Receiver." In: *IEEE Transactions on Molecular, Biological and Multi-Scale Communications* 1.4 (2015), pp. 347–362.

[30] M. B. Dissanayake, Y. Deng, A. Nallanathan, M. Elkashlan, and U. Mitra. "Interference Mitigation in Large-Scale Multiuser Molecular Communication." In: *IEEE Transactions on Communications* 67.6 (2019), pp. 4088–4103.

[31] T. H. O. Donald F. Young Bruce R. Munson and W. W. Huebsch. *A Brief Introduction To Fluid Mechanics*. 5th. Wiley, 2010.

[32] F. Dressler and S. Fischer. "Connecting in-body Nano-communication With Body Area Networks: Challenges and Opportunities of The Internet of Nano Things." In: *Nano Communication Networks* 6 (2015), pp. 29–38.

[33] M. G. Durmaz, A. Dilmac, B. Camli, E. Gencturk, Z. C. Canbek Ozdil, A. E. Pusane, A. D. Yalcinkaya, K. Ulgen, and T. Tugcu. "Preliminary Studies on Flow Assisted Propagation of Fluorescent Microbeads in Microfluidic Channels for Molecular Communication Systems." In: *Bio-inspired Information and Communication Technologies* (2020), pp. 294–302.

[34] C. Elbuken, T. Glawdel, D. Chan, and C. L. Ren. "Detection of Microdroplet Size and Speed Using Capacitive Sensors." In: *Sensors and Actuators A: Physical* 171.2 (2011), pp. 55–62.

[35] A. Enomoto, M. J. Moore, T. Suda, and K. Oiwa. "Design of Self-organizing Microtubule Networks for Molecular Communication." In: *Nano Communication Networks* 2.1 (2011), pp. 16–24.

[36] M. Faraji, Y. Yamini, and M. Rezaee. "Magnetic Nanoparticles: Synthesis, Stabilization, Functionalization, Characterization, and Applications." In: *Journal of the Iranian Chemical Society* 7 (2010).

[37] N. Farsad, A. W. Eckford, S. Hiyama, and Y. Moritani. "On-Chip Molecular Communication: Analysis and Design." In: *IEEE Transactions on NanoBioscience* 11.3 (2012), pp. 304–314.

[38] N. Farsad, D. Pan, and A. Goldsmith. "A Novel Experimental Platform for In-Vessel Multi-Chemical Molecular Communications." In: *GLOBECOM 2017 - 2017 IEEE Global Communications Conference* (2017), pp. 1–6.

[39] N. Farsad, H. B. Yilmaz, A. Eckford, C. Chae, and W. Guo. "A Comprehensive Survey of Recent Advancements in Molecular Communication." In: *IEEE Communications Surveys Tutorials* 18.3 (2016), pp. 1887–1919.

[40] N. Farsad. "Molecular Communication: Interconnecting Tiny NanoBio Devices." In: *GetMobile: Mobile Computing and Communications* 22.2 (2018), pp. 5–10.

[41] N. Farsad, W. Guo, and A. W. Eckford. "Tabletop Molecular Communication: Text Messages through Chemical Signals." In: *PLOS ONE* 8.12 (2013), pp. 1–13.

[42] L. Felicetti, M. Femminella, and G. Reali. "A Simulation Tool for Nanoscale Biological Networks." In: *Nano Communication Networks* 3.1 (2012), pp. 2–18.

[43] L. Felicetti, M. Femminella, and G. Reali. "Simulation of Molecular Signaling in Blood Vessels: Software Design and Application to Atherogenesis." In: *Nano Communication Networks* 4.3 (2013), pp. 98–119.

[44] L. Felicetti, M. Femminella, G. Reali, and P. Liò. "Applications of Molecular Communications To Medicine: A Survey." In: *Nano Communication Networks* 7 (2016), pp. 27–45.

[45] G. Fink, M. Hamidović, A. Springer, R. Wille, and W. Haselmayr. "Design and Realization of Flexible Droplet-based Lab-on-a-Chip Devices." In: *Elektrotechnik und Informationstechnik* (2020), pp. 113–120.

[46] P. Flowers, K. Theopold, R. Langley, and R. W. R. *Chemistry*. Rice University, 2015.

[47] L. Galluccio, T. Melodia, S. Palazzo, and G. E. Santagati. "Challenges and Implications of Using Ultrasonic Communications in Intra-body Area Networks." In: *2012 9th Annual Conference on Wireless On-Demand Network Systems and Services (WONS)* (2012), pp. 182–189.

[48] S. Giannoukos, D. Mcguiness, A. Marshall, J. Smith, and S. Taylor. "A Chemical Alphabet for Macromolecular Communications." In: *Analytical Chemistry* 90 (2018), pp. 7739–7746.

[49] H. Gottlob. *The coil*. Berlin; Munich: Siemens-Aktienges, 1989.

[50] K. D. Granzow. *Homogeneity Of The Magnetic Field Of A Helmholtz Coil*. Sandia Corporation Monograph, 1960.

[51] L. Grebenstein, J. Kirchner, W. Wicke, A. Ahmadzadeh, V. Jamali, G. Fischer, R. Weigel, A. Burkovski, and R. Schober. "A Molecular Communication Testbed Based on Proton Pumping Bacteria: Methods and Data." In: *IEEE Transactions on Molecular, Biological and Multi-Scale Communications* 5.1 (2019), pp. 56–62.

[52] L. Grebenstein, J. Kirchner, R. Stavracakis Peixoto, W. Zimmermann, F. Irnstorfer, W. Wicke, A. Ahmadzadeh, V. Jamali Kooshkghazi, G. Fischer, R. Weigel, A. Burkovski, and R. Schober. "Biological Optical-to-Chemical Signal Conversion Interface: A Small-scale Modulator for Molecular Communications." In: *IEEE Transactions on Nanobioscience* (2018), pp. 31–42.

[53] M. Gregori, I. Llatser, A. Cabellos-Aparicio, and E. Alarcón. "Physical Channel Characterization For Medium-range Nanonetworks Using Flagellated Bacteria." In: *Computer Networks* 55.30 (2011), pp. 779–791.

[54] W. Guo, C. Mias, N. Farsad, and J. Wu. "Molecular Versus Electromagnetic Wave Propagation Loss in Macro-Scale Environments." In: *IEEE Transactions on Molecular, Biological and Multi-Scale Communications* 1.1 (2015), pp. 18–25.

[55] M. C. Gursoy, E. Basar, A. E. Pusane, and T. Tugcu. "Index Modulation for Molecular Communication via Diffusion Systems." In: *IEEE Transactions on Communications* 67.5 (2019), pp. 3337–3350.

[56] M. C. Gursoy, E. Basar, A. E. Pusane, and T. Tugcu. "Pulse Position-Based Spatial Modulation for Molecular Communications." In: *IEEE Communications Letters* 23.4 (2019), pp. 596–599.

[57] M. Hamidović, U. Marta, H. Bridle, D. Hamidovic, G. Fink, R. Wille, A. Springer, and W. Haselmayr. "Off-Chip-Controlled Droplet-on-Demand Method for Precise Sample Handling." In: *American Chemical Society Omega* (2020), pp. 9684–9689.

[58] M. Hamidović, U. Marta, G. Fink, R. Wille, A. Springer, and W. Haselmayr. "Information Encoding in Droplet-Based Microfluidic Systems: First Practical Study." In: *Proceedings of the Sixth Annual ACM International Conference on Nanoscale Computing and Communication*. NANOCOM '19 (2019), pp. 1–6.

[59] G. W. Hanson. "Fundamental transmitting properties of carbon nanotube antennas." In: *IEEE Transactions on Antennas and Propagation* 53.11 (2005), pp. 3426–3435.

[60] W. Haselmayr, A. Zanella, and G. Morabito. "Communications and Networking in Droplet-Based Microfluidic Systems." In: (2019), pp. 1–7.

[61] S. Hiyama, Y. Moritani, R. Gojo, S. Takeuchi, and K. Sutoh. "Biomolecular-Motor-Based Autonomous Delivery of Lipid Vesicles As Nano- or Microscale Reactors on a Chip." In: *Lab on a chip* 10 (2010), pp. 2741–2748.

[62] Y. Huang, M. Wen, L. Yang, C. Chae, X. Chen, and Y. Tang. "Space Shift Keying for Molecular Communication: Theory and Experiment." In: *2019 IEEE Global Communications Conference (GLOBECOM)* (2019), pp. 1–6.

[63] Y. Huang, M. Wen, L. Yang, C. Chae, and F. Ji. "Spatial Modulation for Molecular Communication." In: *IEEE Transactions on NanoBioscience* 18.3 (2019), pp. 381–395.

[64] P. K. Isgor, M. Marcali, M. Keser, and C. Elbuken. "Microfluidic Droplet Content Detection Using Integrated Capacitive Sensors." In: *Sensors and Actuators B: Chemical* 210 (2015), pp. 669–675.

[65] B. Jaafar, J. Luo, D. Firfilionis, A. Soltan, J. Neasham, and P. Degenaar. "Ultrasound Intra Body Multi Node Communication System for Bioelectronic Medicine." In: *Sensors (Basel, Switzerland)* 20 (2019), pp. 2–19.

[66] V. Jamali, A. Ahmadzadeh, W. Wicke, A. Noel, and R. Schober. "Channel Modeling for Diffusive Molecular Communication—A Tutorial Review." In: *Proceedings of the IEEE* 107.7 (2019), pp. 1256–1301.

[67] U. Jeong, X. Teng, Y. Wang, H. Yang, and Y. Xia. "Superparamagnetic Colloids: Controlled Synthesis and Niche Applications." In: *Advanced Materials* 19 (2007), pp. 33–60.

[68] Y. Jian, B. Krishnaswamy, C. M. Austin, A. Ozan Bicen, A. Einolghozati, J. E. Perdomo, S. C. Patel, F. Fekri, I. F. Akyildiz, C. R. Forest, and R. Sivakumar. "nanoNS3: A Network Simulator for Bacterial Nanonetworks Based on Molecular Communication." In: *Nano Communication Networks* 12 (2017), pp. 1–11.

[69] D. Jiles. *Introduction to Magnetism and Magnetic Materials, Second Edition*. Taylor & Francis, 1998.

[70] Y.-W. Jun, J.-w. Seo, and J. Cheon. "Nanoscaling Laws of Magnetic Nanoparticles and Their Applicabilities in Biomedical Sciences." In: *Accounts of chemical research* 41 2 (2008), pp. 179–89.

[71] M. H. Kabir, S. M. Riazul Islam, and K. S. Kwak. "D-MoSK Modulation in Molecular Communications." In: *IEEE Transactions on NanoBioscience* 14.6 (2015), pp. 680–683.

[72] E. Kennedy, P. Shakya, M. Ozmen, C. Rose, and J. Rosenstein. "Spatiotemporal Information Preservation in Turbulent Vapor Plumes." In: *Applied Physics Letters* 112 (2018), pp. 1–6.

[73] L. Khaloopour, S. V. Rouzegar, A. Azizi, A. Hosseinian, M. Farahnak-Ghazani, N. Bagheri, M. Mirmohseni, H. Arjmandi, R. Mosayebi, and M. Nasiri-Kenari. "An Experimental Platform for Macro-Scale Fluidic Medium Molecular Communication." In: *IEEE Transactions on Molecular, Biological and Multi-Scale Communications* 5.3 (2019), pp. 163–175.

[74] H. Knoepfel. "Magnetic Fields: A Comprehensive Theoretical Treatise for Practical Use." In: *American Journal of Physics* 69 (2001).

[75] A. Kolhatkar, A. Jamison, D. Litvinov, R. Willson, and T. Lee. "Tuning the Magnetic Properties of Nanoparticles." In: *International journal of molecular sciences* 14 (2013), pp. 15977–16009.

[76] B. Koo, C. Lee, H. B. Yilmaz, N. Farsad, A. Eckford, and C. Chae. "Molecular MIMO: From Theory to Prototype." In: *IEEE Journal on Selected Areas in Communications* 34.3 (2016), pp. 600–614.

[77] B. Krishnaswamy, C. M. Austin, J. P. Bardill, D. Russakow, G. L. Holst, B. K. Hammer, C. R. Forest, and R. Sivakumar. "Time-Elapse Communication: Bacterial Communication on a Microfluidic Chip." In: *IEEE Transactions on Communications* 61.12 (2013), pp. 5139–5151.

[78] M. Kumari. "Magnetic Properties of Iron-oxide Nanoparticles and Methods for their Characterization." PhD. thesis. Swiss Federal Institute of Technology in Zurich (ETH Zurich), 2015.

[79] M. S. Kuran, H. B. Yilmaz, T. Tugcu, and I. F. Akyildiz. "Modulation Techniques for Communication via Diffusion in Nanonetworks." In: *2011 IEEE International Conference on Communications (ICC)* (2011), pp. 1–5.

[80] M. Kuscu, A. Kiraz, and O. Akan. "Fluorescent Molecules as Transceiver Nanoantennas: The First Practical and High-Rate Information Transfer over a Nanoscale Communication Channel based on FRET." In: *Scientific reports* 5 (2015), pp. 1–6.

[81] V. Labinac, N. Erceg, and D. Kotnik-Karuza. "Magnetic Field of a Cylindrical Coil." In: *American Journal of Physics - AMER J PHYS* 74 (2006), pp. 621–627.

[82] C. Lee, B. Koo, and C. Chae. "Demo: In-Vessel Molecular MIMO Communications." In: *2020 IEEE Wireless Communications and Networking Conference Workshops (WCNCW)* (2020), pp. 1–2.

[83] C. Lee, B.-H. Koo, and C.-B. Chae. "Molecular MIMO Communications Platform with BTSK for In-Vessel Network Systems." In: *Bio-inspired Information and Communication Technologies* (2020). Ed. by Y. Chen, T. Nakano, L. Lin, M. U. Mahfuz, and W. Guo, pp. 289–293.

[84] C. Lee, B. Koo, N.-R. Kim, B. Yilmaz, N. Farsad, A. Eckford, and C.-B. Chae. "Molecular MIMO communication link." In: *2015 IEEE Conference on Computer Communications Workshops (INFOCOM WKSHPS)* (2015), pp. 13–14.

[85] C. Lee, B. Koo, N.-R. Kim, H. B. Yilmaz, N. Farsad, A. Eckford, and C.-B. Chae. "Demo: Molecular MIMO with Drift." In: *the 21st Annual International Conference* (2015), pp. 201–203.

[86] M. Li and Y. Kim. "Feasibility Analysis on the Use of Ultrasonic Communications for Body Sensor Networks." In: *Sensors (Basel, Switzerland)* 18 (2018), pp. 1–11.

[87] Y. Liu, C.-Y. Tsao, E. Kim, T. Tschirhart, J. L. Terrell, W. E. Bentley, and G. F. Payne. "Using a Redox Modality to Connect Synthetic Biology to Electronics: Hydrogel-Based Chemo-Electro Signal Transduction for Molecular Communication." In: *Advanced Healthcare Materials* 6.1 (2017), pp. 1–7.

[88] I. Llatser, D. Demiray, A. Cabellos-Aparicio, D. T. Altilar, and E. Alarcón. "N3Sim: Simulation Framework For Diffusion-based Molecular Communication Nanonetworks." In: *Simulation Modelling Practice and Theory* 42 (2014), pp. 210–222.

[89] K. Lopez, G. Vermeeren, A. Thielens, W. Joseph, and L. Martens. "Characterization of Path Loss and Absorption For a Wireless Radio Frequency Link Between An In-body Endoscopy Capsule and a Receiver Outside The Body." In: *EURASIP Journal on Wireless Communications and Networking* 21 (2014), pp. 1–10.

[90] P. Lu, Z. Wu, and B. Liu. "A Vertical Channel Model of Molecular Communication and Its Test-bed." In: *EAI Endorsed Transactions on Pervasive Health and Technology* 3 (2017), p. 152390.

[91] P. Lu, Y. You, B. Liu, and Z. Wu. "A Vertical Channel Model of Molecular Communication based on Alcohol Molecules." In: *EAI Endorsed Transactions on Creative Technologies* 3 (2016), pp. 157–162.

[92] Y. Lu, M. D. Higgins, and M. S. Leeson. "Comparison of Channel Coding Schemes for Molecular Communications Systems." In: *IEEE Transactions on Communications* 63.11 (2015), pp. 3991–4001.

[93] A. N. Matveev. *Electricity and Magnetism*. Mir Publishers Moscow, 1987.

[94] J. C. Maxwell. *A Treatise on Electricity and Magnetism*. 3rd. Clarendon Press Oxford, 1892.

[95] D. T. McGuiness, S. Giannoukos, A. Marshall, and S. Taylor. "Experimental Results on the Open-Air Transmission of Macro-Molecular Communication Using Membrane Inlet Mass Spectrometry." In: *IEEE Communications Letters* 22.12 (2018), pp. 2567–2570.

[96] D. T. McGuiness, S. Giannoukos, A. Marshall, and S. Taylor. "Parameter Analysis in Macro-Scale Molecular Communications Using Advection-Diffusion." In: *IEEE Access* 6 (2018), pp. 46706–46717.

[97] D. T. Mcguiness, S. Giannoukos, A. Marshall, and S. Taylor. "Modulation Analysis in Macro-Molecular Communications." In: *IEEE Access* 7 (2019), pp. 11049–11065.

[98] D. T. Mcguiness, S. Giannoukos, S. Taylor, and A. Marshall. "Experimental and Analytical Analysis of Macro-Scale Molecular Communications Within Closed Boundaries." In: *IEEE Transactions on Molecular, Biological and Multi-Scale Communications* 5.1 (2019), pp. 44–55.

[99] M. E. McHenry and D. E. Laughlin. *Magnetic Moment and Magnetization*. American Cancer Society, 2012, pp. 1–25.

[100] M. Misakian. "Equations for the Magnetic Field Produced by One or More Rectangular Loops of Wire in the Same Plane." In: *Journal of Research of the National Institute of Standards and Technology* 105 (2000).

[101] M. Mitra. "Medical Nanobot for Cell and Tissue Repair." In: *Journal of Analytical and Pharmaceutical Research* 2 (2017), pp. 1–6.

[102] A. Mohamed and E. Paleologos. *Chapter 15 - Magnetic Properties of Soils*. Butterworth-Heinemann, 2018, pp. 535–580.

[103] J. Mohapatra and J. P. Liu. "Chapter 1 - Rare-Earth-Free Permanent Magnets: The Past and Future." In: ed. by E. Brück. Vol. 27. Handbook of Magnetic Materials. Elsevier, 2018, pp. 1–57.

[104] J. Mohapatra, M. Xing, and J. P. Liu. "Inductive Thermal Effect of Ferrite Magnetic Nanoparticles." In: *Materials* 12.19 (2019).

[105] M. Moore, A. Enomoto, T. Nakano, R. Egashira, T. Suda, A. Kayasuga, H. Kojima, H. Sakakibara, and K. Oiwa. "A Design of a Molecular Communication System for Nanomachines Using Molecular Motors." In: *Fourth Annual IEEE International Conference on Pervasive Computing and Communications Workshops (PERCOMW'06)* (2006), pp. 554–559.

[106] S. Mørup, E. Brok, and C. Frandsen. "Spin Structures in Magnetic Nanoparticles." In: *Journal of Nanomaterials* 2013 (2013).

[107] R. Mosayebi, A. Gohari, M. Mirmohseni, and M. Nasiri-Kenari. "Type-Based Sign Modulation and Its Application for ISI Mitigation in Molecular Communication." In: *IEEE Transactions on Communications* 66.1 (2018), pp. 180–193.

[108] S. Movassaghi, M. Abolhasan, J. Lipman, D. Smith, and A. Jamalipour. "Wireless Body Area Networks: A Survey." In: *IEEE Communications Surveys Tutorials* 16.3 (2014), pp. 1658–1686.

[109] T. Nakano, M. J. Moore, F. Wei, A. V. Vasilakos, and J. Shuai. "Molecular Communication and Networking: Opportunities and Challenges." In: *IEEE Transactions on NanoBioscience* 11.2 (2012), pp. 135–148.

[110] T. Nakano, A. W. Eckford, and T. Haraguchi. "Application Areas of Molecular Communication." In: *Molecular Communication* (2013), pp. 152–168.

[111] T. Nakano, Y. Okaie, and T. Hara. "Applications of Molecular Communication Systems." In: *Encyclopedia of Wireless Networks*. Cham: Springer International Publishing, 2018, pp. 1–6.

[112] A. Noel, K. C. Cheung, and R. Schober. "Improving Receiver Performance of Diffusive Molecular Communication With Enzymes." In: *IEEE Transactions on NanoBioscience* 13.1 (2014), pp. 31–43.

[113] R. O'Handley. *Modern Magnetic Materials: Principles and Applications*. Wiley, 1999.

[114] E. Osmekhina, C. Jonkergouw, G. Schmidt, F. Jahangiri, V. Jokinen, S. Franssila, and M. Linder. "Controlled Communication Between Physically Separated Bacterial Populations in a Microfluidic Device." In: *Communications Biology* 1 (2018), pp. 1–7.

[115] M. Ozmen, E. Kennedy, J. Rose, P. Shakya, J. K. Rosenstein, and C. Rose. "High Speed Chemical Vapor Communication Using Photoionization Detectors." In: *2018 IEEE Global Communications Conference (GLOBECOM)* (2018), pp. 1–6.

[116] M. Ozmen, E. Kennedy, J. Rose, P. Shakya, J. K. Rosenstein, and C. Rose. "High Speed Chemical Vapor Communication Using Photoionization Detectors in Turbulent Flow." In: *IEEE Transactions on Molecular, Biological and Multi-Scale Communications* 4.3 (2018), pp. 160–170.

[117] P. N. Prasanth, K. P. Sumanth, V. K. Chakka, and G. Roy. "Experimental Implementation of Molecular Communication System using Sampling based Adaptive Threshold Variation Demodulation Algorithm." In: *2018 IEEE International Conference on Advanced Networks and Telecommunications Systems (ANTS)* (2018), pp. 1–5.

[118] R. F. Probstein. *Physicochemical Hydrodynamics: An Introduction*. 2nd ed. Wiley-Interscience, 1994.

[119] S. Qiu, T. Asyhari, and W. Guo. "Mobile molecular communications: Positional-distance codes." In: *2016 IEEE 17th International Workshop on Signal Processing Advances in Wireless Communications (SPAWC)* (2016), pp. 1–5.

[120] S. Qiu, W. Guo, M. Leeson, S. Wang, N. Farsad, and A. Eckford. "Nanoparticle Communications: From Chemical Signals in Nature To Wireless Sensor Networks." In: *Nanotechnology Perceptions* 10 (2014), pp. . 29–41.

[121] S. Qiu, W. Guo, S. Wang, N. Farsad, and A. Eckford. "A Molecular Communication Link for Monitoring in Confined Environments." In: *2014 IEEE International Conference on Communications Workshops, ICC 2014* (2014), pp. 718–723.

[122] B. E. Rapp. "Microfluidics: Modelling, Mechanics and Mathematics." In: Micro and Nano Technologies (2017). Ed. by B. E. Rapp, pp. 43–263.

[123] J. B. Reece and N. A. Campbell. *Campbell biology*. 9th ed. Pearson Learning Solutions, 2011.

[124] J.-P. Rospars, V. Křivan, and P. Lánský. "Perireceptor and Receptor Events in Olfaction. Comparison of Concentration and Flux Detectors: a Modeling Study." In: *Chemical Senses* 25.3 (2000), pp. 293–311.

[125] N. Schlechtweg, S. Meyer, H. Unterweger, M. Bartunik, D. Ahmed, W. Wicke, V. Jamali, C. Alexiou, G. Fischer, R. Weigel, R. Schober, and J. Kirchner. "Magnetic Steering of Superparamagnetic Nanoparticles in Duct Flow for Molecular Communication: A Feasibility Study." In: *Body Area Networks: Smart IoT and Big Data for Intelligent Health Management* (2019), pp. 161–174.

[126] M. Seehra. *Magnetic Spinels: Synthesis, Properties and Applications*. IntechOpen, 2017.

[127] R. A. Serway and J. W. Jewett. *Physics for Scientists and Engineers with Modern Physics*. 8th. Pacific Grove, CA, USA: Brooks/Cole Publishing Co., 2011.

[128] M. Seyedi, B. Kibret, D. Lai, and M. Faulkner. "A Survey on Intrabody Communications for Body Area Network Applications." In: *IEEE transactions on bio-medical engineering* 60 (2013), pp. 2067–2079.

[129] P. Shakya, E. Kennedy, C. Rose, and J. K. Rosenstein. "Correlated Transmission and Detection of Concentration-Modulated Chemical Vapor Plumes." In: *IEEE Sensors Journal* 18.16 (2018), pp. 6504–6509.

[130] P. Shih, C. Lee, P. Yeh, and K. Chen. "Channel Codes for Reliability Enhancement in Molecular Communication." In: *IEEE Journal on Selected Areas in Communications* 31.12 (2013), pp. 857–867.

[131] W. R. Smythe. *Static and Dynamic Electricity*. International Series in Pure and Applied Physics. McGraw Hill, 1950.

[132] J. Suzuki, H. Budiman, T. Carr, J. DeBlois, and D. Wang. "NeuroSim: A Neuronal Signaling Simulator for Nanoscale Intrabody Sensor Networks." In: (2013), pp. 1–12.

[133] Tadashi Nakano, Tatsuya Suda, Takako Koujin, Tokuko Haraguchi, and Yasushi Hiraoka. "Molecular Communication Through Gap Junction Channels: System Design, Experiments and Modeling." In: *2007 2nd Bio-Inspired Models of Network, Information and Computing Systems* (2007), pp. 139–146.

[134] Y. Tang, M. Wen, X. Chen, Y. Huang, and L. Yang. "Molecular Type Permutation Shift Keying for Molecular Communication." In: *IEEE Transactions on Molecular, Biological and Multi-Scale Communications* (2020), pp. 160–164.

[135] A. S. Teja and P.-Y. Koh. "Synthesis, Properties, and Applications of Magnetic Iron Oxide Nanoparticles." In: *Progress in Crystal Growth and Characterization of Materials* 55.1 (2009), pp. 22–45.

[136] A. Thalmayer, S. Zeising, D. Ahmed, G. Fischer, and J. Kirchner. "Particle Steering In Magnetic Drug Targeting: A Simple Comsol Model." In: *COMSOL Conference 2020* (2020).

[137] H. Unterweger. "Multimodal Superparamagnetic Iron Oxide Nanoparticles As a Safe Contrast Agent For Magnetic Resonance Imaging and magnetic drug delivery." PhD dissertation. Friedrich Alexander University Erlangen-Nuremberg, 2017.

[138] H. Unterweger, J. Kirchner, W. Wicke, A. Ahmadzadeh, D. Ahmed, V. Jamali, C. Alexiou, G. Fischer, and R. Schober. "Experimental Molecular Communication Testbed Based on Magnetic Nanoparticles in Duct Flow." In: *2018 IEEE 19th International Workshop on Signal Processing Advances in Wireless Communications (SPAWC)* (2018), pp. 1–5.

[139] J. Wang, D. Hu, C. Shetty, and H. Hassanieh. "Understanding and Embracing the Complexities of the Molecular Communication Channel in Liquids." In: *Proceedings of the 26th Annual International Conference on Mobile Computing and Networking*. MobiCom '20 (2020).

[140] J. Wang, B. Yin, and M. Peng. "Diffusion based molecular communication: principle, key technologies, and challenges." In: *China Communications* 14.2 (2017), pp. 1–18.

[141] G. Wei, P. Bogdan, and R. Marculescu. "Efficient Modeling and Simulation of Bacteria-Based Nanonetworks with BNSim." In: *IEEE Journal on Selected Areas in Communications* 31.12 (2013), pp. 868–878.

[142] F. M. White. *Fluid Mechanics*. 7th ed. McGraw Hill, 2010.

[143] L. Xing. "Iron Nanoparticles By Inert Gas Condensation: Structure and Magnetic Characterization." English. PhD thesis. University of Groningen, 2018.

[144] K. Yang et al. "A Comprehensive Survey on Hybrid Communication for Internet of Nano-Things in Context of Body-Centric Communications." In: (2019), pp. 1–26.

[145] H. B. Yilmaz, Y. Cho, W. Guo, and C. Chae. "Interference Reduction via Enzyme Deployment For Molecular Communication." In: *Electronics Letters* 52.13 (2016), pp. 1094–1096.

[146] H. B. Yilmaz, A. C. Heren, T. Tugcu, and C. Chae. "Three-Dimensional Channel Characteristics for Molecular Communications With an Absorbing Receiver." In: *IEEE Communications Letters* 18.6 (2014), pp. 929–932.

[147] H. B. Yilmaz and C.-B. Chae. "Simulation Study of Molecular Communication Systems With An Absorbing Receiver: Modulation and ISI Mitigation Techniques." In: *Simulation Modelling Practice and Theory* 49 (2014), pp. 136–150.

[148] A. J. G. Yunus A. Çengel. *Heat and Mass Transfer: Fundamentals and Applications*. 5th ed. McGraw-Hill Education, 2015.

[149] H. Zhai, Q. Liu, A. V. Vasilakos, and K. Yang. "Anti-ISI Demodulation Scheme and Its Experiment-Based Evaluation for Diffusion-Based Molecular Communication." In: *IEEE Transactions on NanoBioscience* 17.2 (2018), pp. 126–133.

[150] J. Zhao, X. Chen, B. Liang, and Q. Chen. "A Review on Human Body Communication: Signal Propagation Model, Communication Performance, and Experimental Issues." In: *Wireless Communications and Mobile Computing* (2017), pp. 1–15.

In this dissertation, based on the Molecular Communication (MC) system, a macroscale aqueous-based testbed is used to imitate the propagation of biocompatible drug-loaded Superparamagnetic Iron Oxide Nanoparticles (SPIONs) through a human vessel for drug delivery applications. In the testbed, particle suspension is pumped at different flow rates into a channel filled with water and detected by a susceptometer. All fundamentals required to understand the testbed's physics are discussed. In a preliminary study, the testbed is simplified to a 2D rotationally symmetric model described mathematically, and its flow regime is analytically derived. A full numerical study of the simplified model is carried out. To avoid the computational complexity of the 3D Multiphysics simulations, the magnetic and fluidic simulations are decoupled and simulated separately, from which the system response is efficiently estimated. Other detectors, including Helmholtz, Maxwell, and planar coils, are also considered. The detected signal of the coils is found to be directly proportional to the volume susceptibility and thus to the density of the particles in their detection regions. Changing the particle distribution inside the transmitter before being injected into the channel leads to various distributions inside the detector, significantly affecting the system response.

ISBN 978-3-96147-517-9

FAU UNIVERSITY PRESS 2022